Title
The Effects of Cytoskeletal Perturbation on Neuronal Structure, Biomechanics, and Function

Permalink
https://escholarship.org/uc/item/1b20m3sk

Author
Bober, Brian Geoffrey

Publication Date
2015

Peer reviewed|Thesis/dissertation

UNIVERSITY OF CALIFORNIA, SAN DIEGO

The Effects of Cytoskeletal Perturbation on Neuronal Structure, Biomechanics, and Function

A dissertation submitted in partial satisfaction of the
requirements for the degree Doctor of Philosophy

in

Bioengineering

by

Brian Geoffrey Bober

Committee in Charge:

Professor Sameer Shah, Chair
Professor Adam Engler, Co-Chair
Professor Alex Groisman
Professor Andrew McCulloch
Professor Samuel Ward

2015

The Dissertation of Brian Geoffrey Bober is approved, and it is acceptable in quality and form for publication on microfilm and electronically:

Co-Chair

Chair

University of California, San Diego

2015

TABLE OF CONTENTS

LIST OF FIGURES AND TABLES

ACKNOWLEDGMENTS

The work presented in this dissertation could not have been completed without the support of numerous colleagues and mentors. First and foremost, I thank my advisor, Dr. Sameer Shah, for accepting me into his lab and providing guidance throughout my time as a graduate student. I credit much of my development as a scientist to Dr. Shah and his excellent mentorship, advice, and scientific expertise. I would also especially like to thank Dr. Alex Groisman and Dr. Edgar Gutierrez for creating the cell stretching device used throughout my studies, allowing me to use their lab space, and their technical expertise. I also acknowledge and thank Dr. Richard Lieber, Dr. Sam Ward, Dr. Simon Schenk, and Dr. Koichi Masuda, for their help and suggestions during my time at UCSD. Finally, I acknowledge my other dissertation committee members not yet mentioned, Dr. Adam Engler and Dr. Andrew McCulloch.

Many other students and technical staff members have also provided me with much help over the last several years. From the Neuromuscular Bioengineering Lab, I would like to thank Dr. James Love, for his experimental and analytical suggestions. I would also like to acknowledge Dr. Gunja Dave, Dr. Tom Chuang, Justin Papreck, Dr. Ken Vaz, Dr. Ian Foran, Steven Horton, Vincent Hussey, and Elizabeth Orozco, for their help running experiments and scientific suggestions. Finally, I would like to acknowledge all of the technical staff and students at the UCSD Muscle Physiology Lab, in particular Dr. Raji

Pichika and Shannon Bremner, who provided scientific support, suggestions, and training during my time at UCSD.

I would like to acknowledge my family and friends for their support over the years. In particular, I would like to thank my parents for their love and steadfast belief in me throughout my entire life, and for providing me with all the tools and emotional support I needed to be successful. I would also like to thank my siblings for their advice and guidance. Finally, I would like to thank Kelsey Wiechert for her unwavering support and love over the last couple of years, and for seeing me through the challenges of graduate school.

The content of chapter 2 was published as a manuscript in the journal Experimental Neurology, and is titled “Combinatorial influences of paclitaxel and strain on axonal transport.” I would like to acknowledge my co-authors: Edgar Gutierrez, Steven Plaxe, Alex Groisman, and Sameer Shah.

The content of chapter 3 was accepted for publication as a manuscript in the Journal of Biomechanics, and is titled “Paclitaxel alters sensory nerve biomechanical properties.” I would like to acknowledge my co-author Sameer Shah.

The content of chapter 4 is original and unpublished. It will be prepared for submission to a peer-reviewed journal at a future date, and will include the co-authors Sameer Shah and Elizabeth Orozco.

The content of chapter 5 was published as a manuscript in the journal Cytoskeleton, and is titled “Actin-myosin network influences morphological

response of neuronal cells to altered osmolarity.” I would like to acknowledge my co-authors James Love, Steven Horton, Mariya Sitnova, Sinan Shahamatdar, Ajay Kannan, and Sameer Shah.

VITA

2006 – 2010	Carnegie Mellon University Bachelor of Science, Chemical Engineering With Additional Major in Biomedical Engineering
2010 – 2015	University of California, San Diego Doctor of Philosophy, Bioengineering

PUBLICATIONS

Bober BG, Shah SB. Paclitaxel alters senosry nerve biomechanical properties. Journal of Biomechanics 2015. (in press)

Bober BG, Gutierrez E, Plaxe S, Groisman A, Shah SB. Combinatorial influences of paclitaxel and strain on axonal transport. Experimental neurology 2015;271:358-67.

Chetta J, Love JM, Bober BG, Shah SB. Bidirectional actin transport is influenced by microtubule and actin stability. Cellular and molecular life sciences : CMLS 2015.

Bober BG, Love JM, Horton SM, et al. Actin-myosin network influences morphological response of neuronal cells to altered osmolarity. Cytoskeleton 2015.

Shah SB, Chetta J, Bober BG. Axonal Transport and Neuromechanics, Textbook Chapter in "Molecular and Cellular Biomechanics". Pan Stanford Publishing, 2015.

Barry DM, Stevenson W, Bober BG, et al. Expansion of neurofilament medium C terminus increases axonal diameter independent of increases in conduction velocity or myelin thickness. The Journal of neuroscience : the official journal of the Society for Neuroscience 2012;32:6209-19.

ABSTRACT OF THE DISSERTATION

The Effects of Cytoskeletal Perturbation on Neuronal Structure, Biomechanics, and Function

by

Brian Geoffrey Bober

Doctor of Philosophy in Bioengineering

University of California, San Diego, 2015

Professor Sameer Shah, Chair

Professor Adam Engler, Co-Chair

Paclitaxel is a common chemotherapeutic that often causes peripheral sensory neuropathy. Paclitaxel binds to and stabilizes microtubules, preventing their depolymerizaiton. Through unknown mechanisms, paclitaxel treatment

causes bundling and altered organization axonal microtubules. In neurons, microtubules serve several roles, including facilitating axonal transport, and supporting axonal structure. In addition, peripheral nerves exist in a dynamic biomechanical environment and undergo significant strain during joint motion. Given the structural and functional roles of microtubules, this dissertation explores the effects of paclitaxel on nerve biomechanics and the ability of neurons to properly accommodate tensile loading.

Chapter 2 explores experiments testing the hypothesis that axonal stretch magnifies disruptions in axonal transport in paclitaxel treated neurons. Results indicated that stretch alone minimally altered axonal transport, paclitaxel treatment alone significantly decreased transport velocity and frequency, and the combination of both paclitaxel and stretch together led to the largest disruptions in the transport of multiple different cargoes.

Chapter 3 discusses whether microtubule bundling observed in paclitaxel treated axons leads to changes in the tissue level mechanical properties of whole nerves. In this experiment, the mechanical properties of nerves bathed in paclitaxel were compared to control nerves. Results showed that paclitaxel significantly stiffened nerves.

Chapter 4 investigates the role of tau in inducing microtubule bundling following paclitaxel treatment. In this study, nervous tissue from tau knockout mice exhibited significantly less microtubule bundling than tissue from wild type mice, indicating that tau may play a role aberrant microtubule bundle formation

following paclitaxel treatment. Collectively, results from chapters 2-4 show that paclitaxel treatment leads to microtubule bundling, partially due to tau, which leads to tissue level mechanical changes and an inability of neurons to successfully accommodate mechanical loading.

Chapter 5 is unrelated to the effects of paclitaxel on neurons, but is related to the theme of determining the effects of cytoskeletal perturbations on neuronal function. This chapter discusses the effects of actin and myosin on osmotic regulation of SH-SY5Y neuroblastoma cells. Results indicated that actin and myosin disruption differentially altered the normal cellular response to osmotic loading, and neuronal cells were unable to restore normal morphology 30 minutes after osmotic insult.

CHAPTER 1: INTRODUCTION

1.1 Peripheral Nervous System Anatomy

The peripheral nervous system consists of the nerves and ganglia that exist outside of the brain and spinal cord. The nerves of the peripheral nervous system extend to the distal extremities and provide a critical link allowing for electrical signal transmission between the central nervous system and the rest of the body (*fig 1.1*). The peripheral nervous system can be further sub-classified into the somatic nervous system, responsible for voluntary muscle control, the sensory nervous system, responsible for relaying sensory information towards the brain, and the autonomic nervous system, responsible for regulation of bodily functions controlled by internal organs.

Sensory neurons originate at the dorsal root ganglia, which are clusters of neuronal cell bodies located along the vertebral column next to the spine with projections entering the spinal cord dorsally. In contrast, alpha motor neurons originate from within the spinal cord in the ventral horn, and their axons extend ventrally from the spinal cord forming the ventral roots. The dorsal roots and ventral roots join together to form mixed spinal roots, which then further branch and extend to the periphery as peripheral nerves.

The neurons, which are the primary functional units of peripheral nerves, are the longest cells in the human body due to the fact that their axons extend continuously from the cell bodies located in or near the spinal cord to innervation sites located in the distal extremities of the body that can be over a meter away. In addition, peripheral neuron axonal diameters are extremely small in relation to their lengths, with the smallest sensory axons measuring less than a micron in diameter and the largest motor and sensory axons measuring up to 20 microns[1]. The dimensions of peripheral neurons make them uniquely susceptible to injury – any disruption to an axon along its track can prevent signaling between its innervation sites in the peripheral and central nervous systems. Consequently, the biomechanical environment of peripheral nerves is of critical importance to preventing injury to the long, thin, axons housed in their interiors.

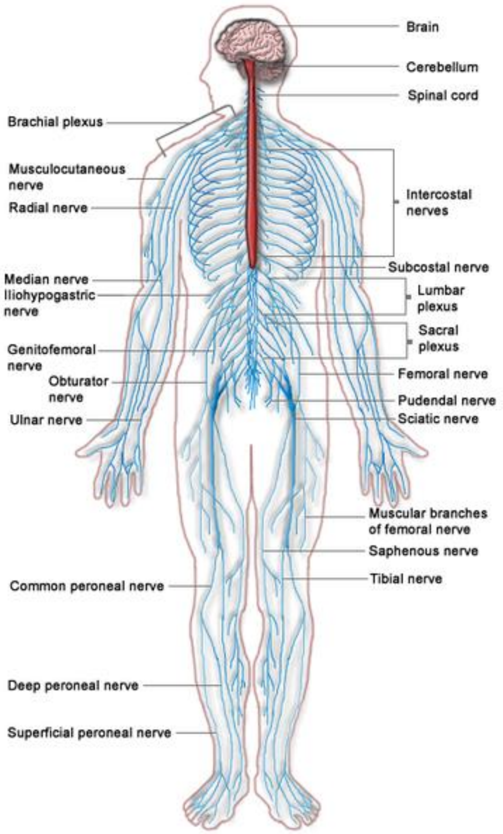

Figure 1.1 – Central vs. peripheral nervous system
Illustration indicating the components of the central nervous system (brain and spinal cord, in red) and the peripheral nervous system (nerves extended from spinal cord, in blue)[2]

1.2 Mechanical Loading in the Peripheral Nervous System

Peripheral nerves naturally exist under tension as evidenced by their recoil when severed[3]. Because peripheral nerves must span articular joints in order to reach the distal extremities of the body, they necessarily undergo considerable biomechanical loading during joint motion[4]. Movement induces tensile stress in the nerve which is accommodated by a combination of excursion along the nerve bed and strain of the nerve[4,5]. As elongation occurs, nerves undergo a reduction in cross-sectional area, which is partially resisted by fluid and connective tissue in the nerves and leads to increased pressure[5]. Tensile strain in nerves strain can be considerably high, particularly around joint regions where strains of up to 20%[6] or higher have been observed.

Despite their ability to accommodate loads, there are limitations to the magnitude of strain a nerve can maintain before damage occurs. For example, experiments reveal that even relatively small strains of 11-15.7% cause marked reductions in blood flow in rat sciatic nerves[7,8]. Strains of only 6% in rabbit tibial nerves lead to decreases in the compound action potential of the analyzed nerves, and strains of 12% completely block nerve conduction and lead to permanent damage[9]. In humans, nerve entrapment syndromes such as carpal and cubital tunnel syndromes are hypothesized to result from abnormal nerve compression[10,11] and possibly altered strain profiles[12] due to soft tissue abnormalities, and these syndromes are treated with surgeries aimed to release the nerve from any abnormal connections[13].

1.3 Peripheral Nerve Structure and Biomechanics

As a consequence of these structural and biological considerations, the nerves and the axons in within them are structurally organized to be protected from damage under non-pathological or acutely injurious conditions. Axons in a nerve exist in an undulating state at rest[14]. Due to optical effects of superimposed undulating axons and their surrounding connective tissue, peripheral nerves show characteristic periodic bands known as the Bands of Fontana[15,16]. During joint motion, these bands become less distinct and are spaced further apart until they eventually disappear[17], and so, undulating axons are believed to unravel with nerve strain. This redundancy in length is considered to be an adaptation to prevent excessive mechanical loading of the axons themselves during movement induced nerve strain (*fig 1.2*).

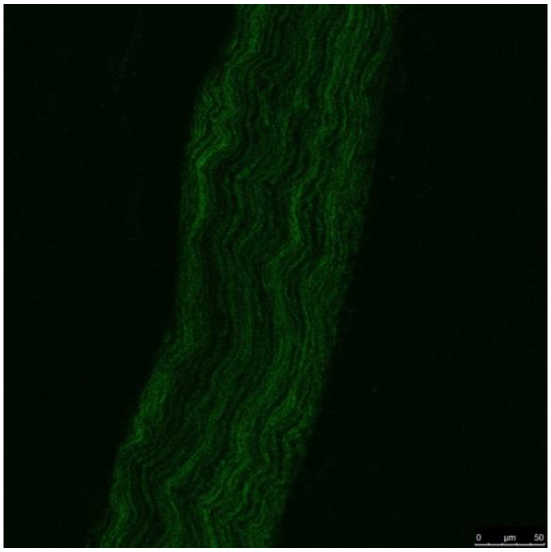

Figure 1.2 – Axonal Undulations
Fluorescent axons in a mouse sural nerve follow an undulating course.

Aside from the axons themselves, nerves consist of multiple layers of cells and connective tissue (*fig 1.3*). Axons are surrounded Schwann cells with or without myelin, and these cells are locally surrounded by basal lamina, collagen, and other proteins making up the endoneurium. Axons are bundled into fascicles surrounded by a sheath of perineurium composed of up to 15 layers of perineurial cells, basal lamina, collagen fibrils, and elastic fibers[4]. Fascicles are bound by the epineurium, containing fibroblasts, mast cells, fat cells, and bundles of collagen fibrils and elastic fibers which serve load bearing purposes[4].

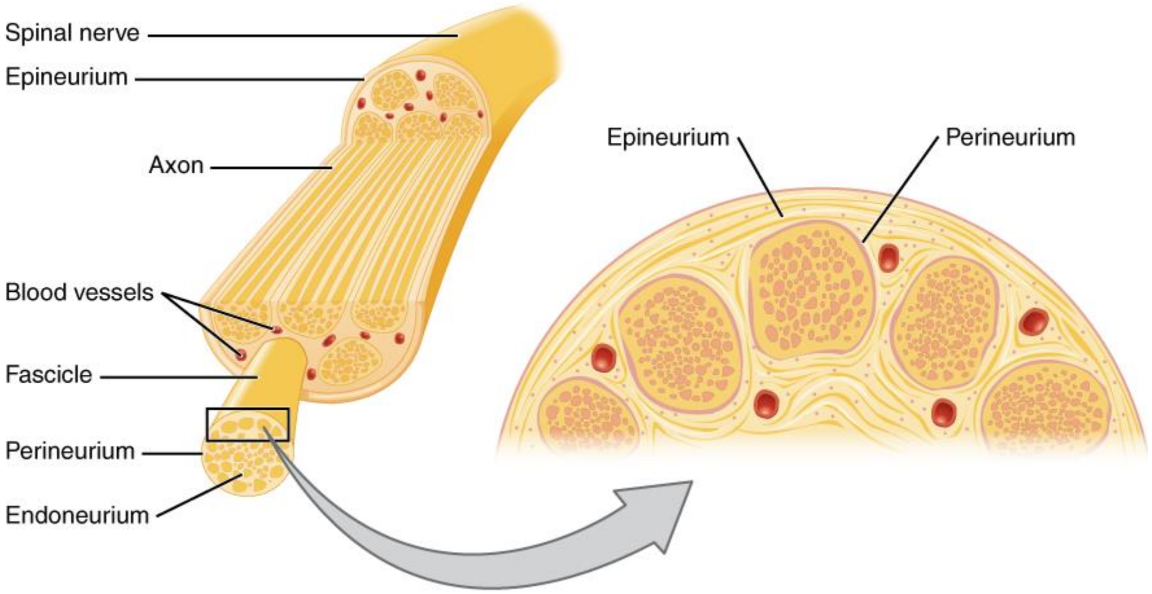

Figure 1.3 – Architecture of peripheral nerve
Axons and surrounding Schwann cells are embedded in endoneurium. Clusters of axons form fascicles, which are bound by perineurium. Groups of fascicles compose the whole nerve which is bound by epineurium.[18]

Importantly, inner structural damage can occur before visible tearing of the epineurium[4,19]. In fact, the perineurium is believed to be the primary load bearing component of the nerve due to biomechanical experimentation revealing sharp decreases in the load bearing capacity of nerves concomitant with histological evidence of perineurial rupture during excessive strain[19]. However, it is important to note that this may be an oversimplification, as it is possible that other types of less visible damage to other nerve components could also contribute to such observations.

Like most soft tissues, peripheral nerves are viscoelastic, and show stress-relaxation when held at constant strain[20]. Measurements of nerve stress during elongation have shown that nerves undergo strain stiffening[21]. At low strains, nerves are extremely compliant and minimal increases in stress lead to large increases in strain. Stress-strain curves of peripheral nerves refer to this compliant region as the toe region. As the nerve is progressively stressed to *in situ* strains and beyond, nerve stress begins to increase linearly with strain; this region is referred to as the linear region. Eventually, at extremely large, non-physiological strains, nerves will plastically deform and experience clear structural damage and decreases in load bearing capacity[4].

1.4 Neuronal Structure and the Cytoskeleton

In addition to structural support by connective tissue layers, neurons themselves contain an internal cytoskeletal network critical for maintaining axonal structure and providing mechanical stability over long distances. Compared to other cell types, neurons possess a unique polarized structure with a cell body and a long extending axon. Multipolar neurons, the most common type of neuron in the body, also contain dendrites, branched projections near the cell body which receive input from other neurons. Each of these distinct compartments –

the axon, dendrites, and cell body, has its own unique structural organization. Interestingly, sensory neurons, the dorsal root ganglia, contain no dendrites. Instead, axons of the dorsal root ganglia neurons contain two branches, with one running to the periphery and the other to the spinal cord (*fig 1.4*). This type of neuronal structure is referred to as pseudounipolar.

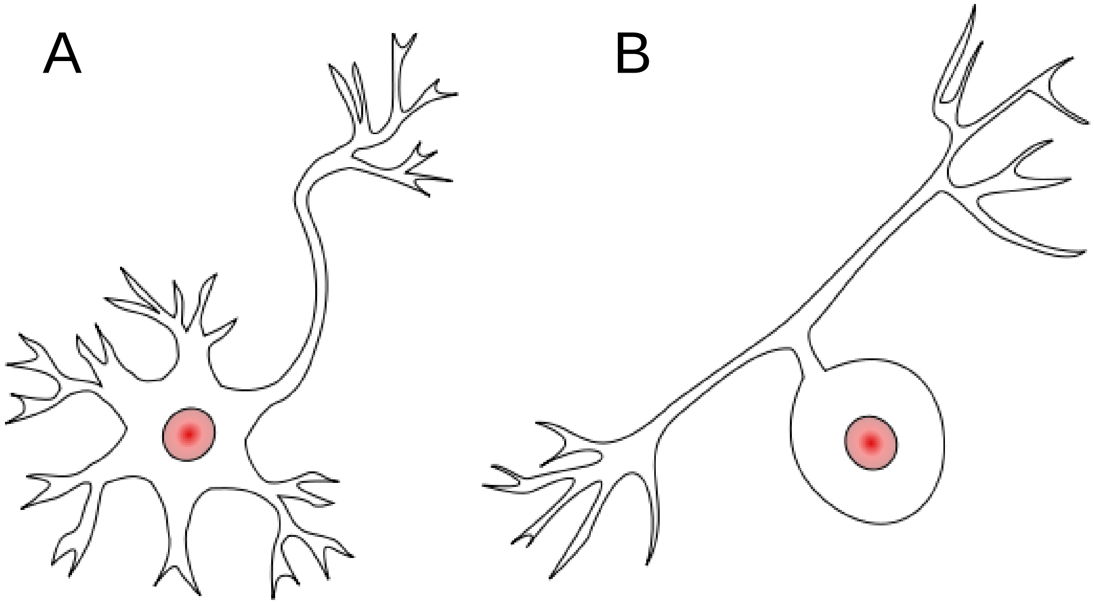

Figure 1.4 – Neuron morphology
Schematic of a multipolar neuron (A) and a pseudounipolar neuron (B). Dorsal root ganglia sensory neurons are pseudounipolar and contain no dendrites.[22]

The cytoskeleton of a neuron contains 3 major building blocks – microtubules, neurofilaments, and actin microfilaments, though other filament types are also present. Disruption of any of these components with drug treatment leads to dramatic decreases in the indentation stiffness of neurons, as verified by atomic force microscopy[23], highlighting the contributions of these proteins to neuronal compressive cell mechanics. In addition to these components, a vast array of supporting proteins affects the stability, length, organization, and crosslinking of these structures. Neurofilaments are heteropolymers roughly 10 nm in diameter that can be hundreds of microns in length. They are particularly abundant in axons, though present in all neuronal compartments. There are three major neurofilament subunits typically referred to as heavy, medium and light chains, based on their molecular weights, but other subunits also exist and include peripherin, α -internexin, and nestin[24]. Neurofilaments contain side arms projecting radially and have been noted to play roles in radial growth of axons, and therefore, in conduction velocity[25].

Actin microfilaments are composed of 42 kDa actin monomers arranged in two protofilaments in a double helix formation. They are approximately 7 nm in diameter, and in neurons most are less than 1 μm in length[25]. Actin is found throughout neurons but is enriched in regions located near the cell membrane, near presynaptic terminals, in dentritic spines, and in growth cones of elongating neurites[25]. Actin has a diverse array of proteins which interact with it, including myosin motor proteins, cross-linking proteins, bundling proteins, and anchoring proteins. Actin and the proteins that interact with it are responsible for a diverse range of functions, including maintaining cell structure and shape, segregating axonal and dendritic compartments, enabling cell adhesion and interaction with the extracellular environment, and enabling growth cone motility.

Neuronal microtubules are heterodimers of α- and β-tubulin subunits (~50 kDa)[25]. The α- and β- subunits align end to end to form protofilaments, and protofilaments align laterally generating a pseudo-helical structure with, most commonly, 13 tubulin dimers from different protofilaments comprising one turn of the helix[26]. The resulting structure is a hollow tube formation with an inner diameter of 12 nm and an outer diameter for 24 nm. In neurons, microtubules can vary in length from several microns to over 100 µm[25]. The structure of microtubules imparts it with a natural polarity due to the head to tail arrangement of α- and β-tubulin subunits in each protofilament and the uniform orientation of each protofilament in a given microtubuled. The so-called (+) end of the microtubule will have β- subunits exposed and the (-) end will have α- subunits exposed[26]. This arrangement is critical to microtubule function, as elongation occurs much more rapidly at its (+) end[27].

Each tubulin dimer has two GTP binding sites – one binding site to α-tubulin which is stable and plays a structural role, and one to β-tubulin which is more dynamic and can be hydrolyzed to GDP. Whereas GTP-bound tubulin favors polymerization, GDP-bound tubulin favors disassembly. If the tip of the (+) end of the microtubule is bound to GDP, rapid disassembly of the microtubule can occur[28]. A large number of post-translational modifications and interactions with microtubule associated proteins can also affect the stability of microtubules. This is particularly true for neurons, which contain many different isotypes of tubulins and specific microtubule associated proteins that are present only within specific neuronal compartments. For example, the microtubule associated protein tau is present only in axons, whereas MAP2 is present only in dendrites and cell bodies[25]. This suggests that microtubule characteristics are controlled to perform specified tasks in neurons. Microtubule organization in neurons varies considerably depending on the compartment analyzed. In axons, microtubules exist in parallel arrays (*fig 1.*5) oriented with their (+) ends facing the distal tip of the axon. In dendrites, microtubules are shorter than in axons, and exhibit mixed polarity[27].

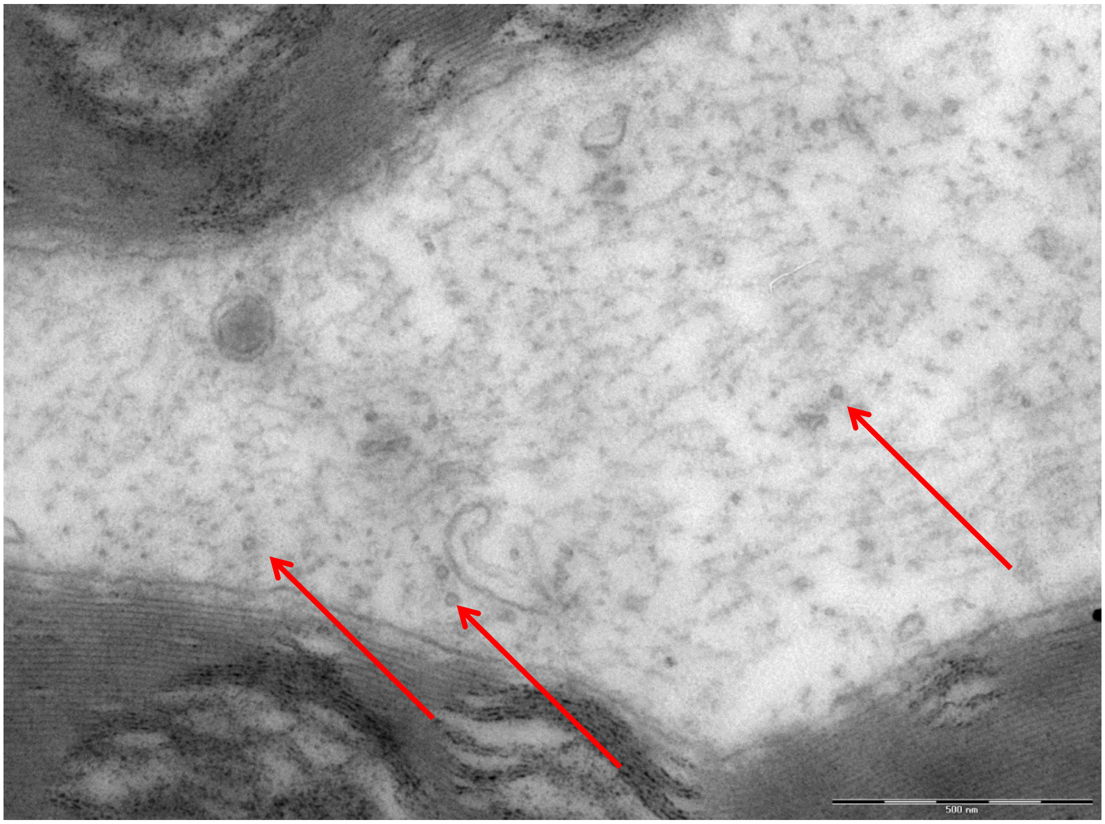

Figure 1.5 – Axonal microtubules
Electron micrograph showing cross section of an axon with microtubules (arrows) showing uniform orientation aligned in the direction of the axon.

Microtubules have several critical roles in neurons. Microtubules help maintain axonal structure and are required for axonal outgrowth[29]. During growth cone mediated elongation, microtubules enter the periphery of the growth cone and provide structural support during continued elongation. Microtubules can cross-link to each other as well as other cytoskeletal proteins[30-32], and microtubules themselves are extremely stiff, with a Young's modulus estimated to be roughly 1.5 GPa[32]. Conventionally, microtubules in cells bear compressive loads generated by the actin-myosin cytoskeleton; however, in axons, microtubules also bear loads under tension as well due to the connectivity of the cytoskeleton. Indeed, experimental analysis of traumatic stretch injury in neurons shows fracturing of microtubules in axons[33,34], and mathematical simulations hypothesize that microtubule density and microtubule cross-linking play significant roles in the tensile mechanics of axons[29,30].

1.5 Axonal Transport

In addition to their mechanical roles, microtubules also provide a critical framework upon which axonal transport occurs. While axons can extend to lengths on the order of 1 meter in humans, proteins, macromolecules, and organelles are all mainly manufactured in the cell body, with less than one percent of total protein production taking place in the axon itself[35]. To overcome the insufficiency of newly synthesized local materials in axons, neurons contain an elaborate axonal transportation system, in which kinesin and dynein motors carry proteins and organelles to and from the distal reaches of the axon upon microtubule based tracks. This process of axonal transport is complex – an enormous variety of cargoes are transported at different bulk rates[36] and the specific motion dynamics of these cargoes are either not fully known or are subject to change depending on other factors such as axon length[37], neuronal age[38], and connectivity patterns to the extracellular matrix environment[39].

Early experimentation in the field of axonal transport involved the monitoring of radio-labeled amino acids applied to the cell bodies of neurons. These amino acids were incorporated into proteins, and the peaks of radiolabeled material were then later discovered to have moved large distances, indicative of axonal transport[40]. Broadly, axonal transport can be classified as either fast or slow axonal transport, with slow axonal transport being further categorized into slow components a and b (SCa and SCb). Cargoes transported by fast axonal transport move at up to 400 mm/day and include vesicular cargoes and organelles[40,41]. SCa cargoes move at roughly .1-1 mm/day and include cytoskeletal proteins such as neurofilaments and microtubules. SCb cargoes move slightly faster at 2-10mm/day, and include actin and cytoskeletal associated proteins[40,41]. More recent analysis of typical SCa cargoes including microtubules and neurofilaments has revealed that these cargoes move at similar instantaneous velocities as fast transported cargoes, but their movement frequently pauses for long durations[42-44]. Thus, these bulk transport rates are now believed to be an average of short bursts of movement coupled with periods of no motion, with faster cargoes pausing less frequently – the so called “Stop-and-Go” hypothesis[45].

While the dynamics of axonal transport are intricate and actively studied, there is a breadth of conclusive evidence suggesting that disruptions in axonal transport are deleterious to neuronal health[46]. Axonal transport deficits are extensively observed in many neuropathies of both the central and peripheral nervous system including Alzheimer’s disease, amyotrophic lateral sclerosis, Parkinson’s disease, subtypes of Charcot-Marie Tooth disease, diabetic neuropathy, and chemotherapy induced peripheral neuropathy[46-48]. The focus of my dissertation will be on the effects of a common chemotherapeutic agent known as paclitaxel on axonal transport, due to fundamental interactions of paclitaxel with the neuronal cytoskeleton.

1.6 Paclitaxel

Paclitaxel, also known by its brand name Taxol, belongs to a class of drugs known as taxanes and is used to treat a variety of metastatic cancers including breast, ovarian, and non-small cell lung cancer. While effective in treating cancer, paclitaxel is delivered systemically, and can accumulate in other cell types, including neurons of the peripheral nervous system[49]. Consequently, as many as 60% of the patients receiving the drug[48] develop varying degrees of peripheral neuropathy. Intriguingly, paclitaxel induced neuropathy primarily affects the sensory nervous system, with little apparent motor involvement observed in most, though not all, patients. Symptoms typically begin in the distal extremities and progress proximally, and can include loss of sensory function, paresthesia, and neuropathic pain. The most common patient symptoms are diminished sensations to pain, temperature, and vibration, proprioceptive deficiencies, and loss of deep tendon reflexes[49,50]. Such a pattern of symptoms indicates that both small and large diameter sensory axons are susceptible to paclitaxel induced changes. In addition, sensory neuropathy symptoms are dose dependent and can be so severe that peripheral neuropathy is generally cited as the dose limiting side effect of paclitaxel treatment[49]. Although cessation of treatment often leads to resolution of symptoms, some symptoms can persist for months or years[51].

Mechanistically, paclitaxel binds to β-tubulin at the inner microtubule lumen, resulting in microtubule stabilization[52]. This suppresses microtubule dynamics and prevents them from depolymerizing. By suppressing microtubule dynamics, paclitaxel can prevent cell division, thus explaining its anti-cancer properties. It has been proposed that this stabilization occurs because paclitaxel induces a short helix formation in the M-loop of β-tubulin that strengthens lateral protofilament interactions[53]. Paclitaxel stabilized microtubules show a number of abnormal properties. While typically GTP is required for microtubule polymerization, paclitaxel can promote microtubule polymerization even in its absence[54]. In addition, the most common microtubule cylindrical structure contains 13 laterally joined protofilaments, and paclitaxel treatment results in a population shift in favor of a 12 protofilament structure[55]. Paclitaxel stabilization also results in altered mechanical properties of microtubules, typically increasing their compliance[56].

1.7 Paclitaxel, Mechanisms of Disease, and Axonal Transport

Given the critical importance of microtubules to neuronal structure and function, it is not surprising that microtubule perturbation via paclitaxel treatment leads to peripheral neuropathy. However, the exact mechanisms by which paclitaxel induces these neurotoxic effects are not clearly understood. Many observations of paclitaxel induced abnormalities have been noted, and several sites of pathogenesis have been proposed. Paclitaxel heavily inhibits neurite initiation and extension velocity in cultured sensory neurons[57,58] in a dose dependent fashion and disrupts growth cone turning dynamics[59]. Dividing cells exposed to paclitaxel often die by apoptosis. However, dorsal root ganglia exposed to micromolar concentrations of paclitaxel *in vitro* show high levels of cell death (40-50%) after just 48 hours, but this death is not by apoptosis[58]. One *in vitro* study tracking the plus end of microtubules in cultured Aplysia neurons showed that post paclitaxel exposure, the uniformity of microtubule polarity in the axon was disrupted[60].

Other studies indicate that cells treated with paclitaxel develop abnormal microtubule bundles[61] (*fig 1.6*), and biochemical analysis indicates that these bundles of microtubules show increased connectivity[31]. More specifically, abnormal microtubule arrays develop in paclitaxel treated DRG cultures[62]. Paradoxically, in the central nervous system, extremely low nanomolar dosages of paclitaxel have been reported to actually enhance regeneration[63], and other studies have suggested potential therapeutic uses of paclitaxel in treating neurodegenerative diseases such as Alzheimer’s in which microtubule destabilization may be a contributing factor to disease progression[64,65]. Such observations emphasize the dose dependence of paclitaxel related effects.

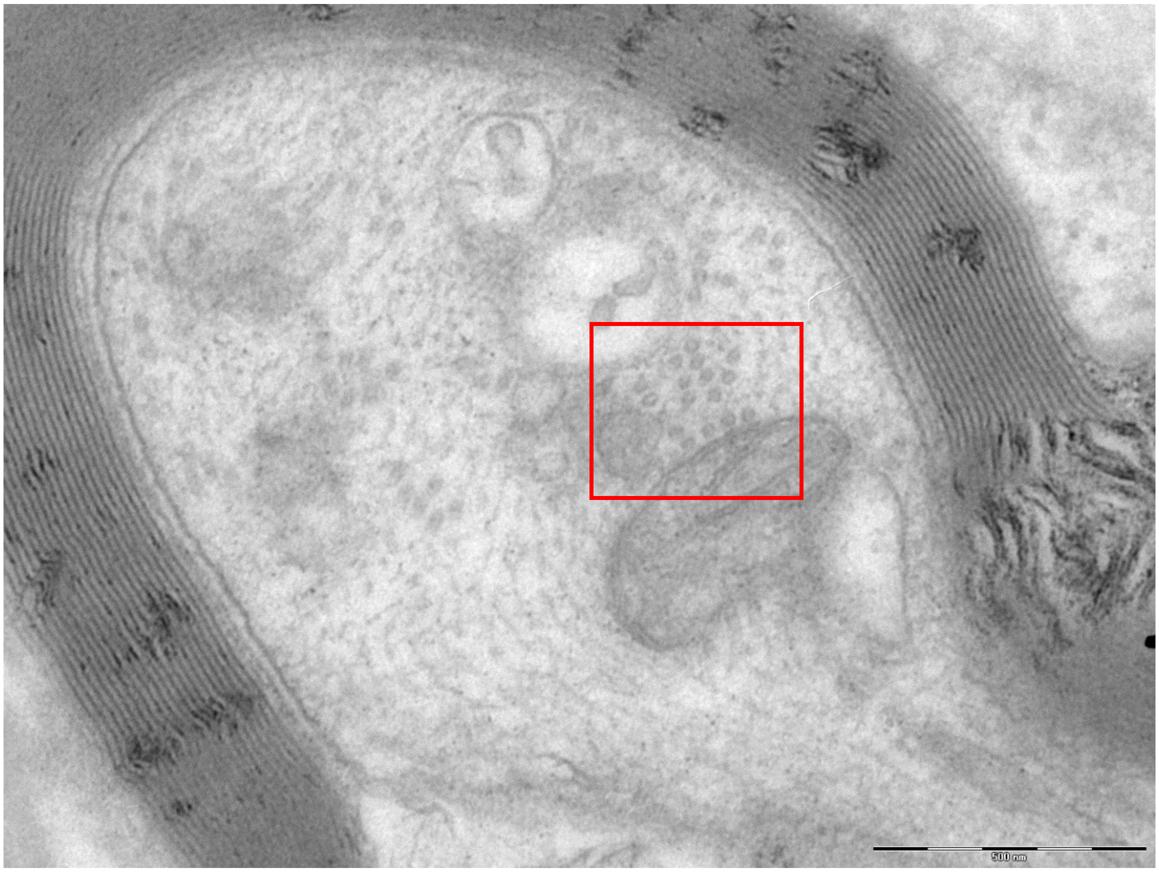

Figure 1.6 – Paclitaxel induced microtubule bundles
Electron micrograph of an axon exposed to paclitaxel. Microtubules form abnormal clusters (red box)

Evidence of paclitaxel induced microtubule bundling extends to *in vivo* work which shows that paclitaxel injected sciatic nerves in rats develop an increase in microtubule aggregation in axons and surrounding Schwann cells leading to localized bulging of the axon at the injection site[66], myelin damage[67], and abnormal arrays of microtubules especially present near organelles[68]. While massive axonal degeneration does not typically occur at moderate dosages, it has been shown in a rat model that paclitaxel causes partial degeneration of A- and C- fibers in the epidermis associated with an increase in the spontaneous firing of action potentials [69]. Such findings are corroborated in human case studies where high, repetitive dosages of paclitaxel result in signs of sural nerve degeneration[70]. High dosages of paclitaxel in animal models are additionally associated with degeneration of major nerve branches[71].

While direct microtubule related effects are likely to contribute to the pathogenesis of paclitaxel induced neuropathy, off-target effects have been noted as well[52]. For example, high concentrations of paclitaxel induce mitochondrial depolarization and calcium release[72], and swollen mitochondria are noted in paclitaxel treated peripheral nerves[73]. Paclitaxel treatment induces macrophage activation in the sciatic nerve as well as microglial and astrocyte cells in the spinal cord[74]. Finally, TRPV1, an ion channel related to pain signaling neurons, is upregulated following paclitaxel treatment[75]. It is important to note that while many observations of paclitaxel induced defects have been noted, no definitive mechanism of damage or order of progression at the cell level has been determined.

The most commonly theorized mechanism of paclitaxel based neurotoxicity is the disruption of axonal transport routinely reported following paclitaxel treatment. Several studies have reported various degrees of disruption of the transport of a variety of cargoes. For example, the retrograde fast axonal transport of injected wheat germ agglutinin was impaired post paclitaxel treatment in a rat sciatic nerve[76]. Paclitaxel additionally was observed to disrupt anterograde, though not retrograde, fast transport in extruded squid axoplasm[77]. Bulk anterograde fast transport of injected horse radish peroxidase into cultured dorsal root ganglia was shown to be disrupted after paclitaxel treatment[78].

Vesicle and mitochondrial transport frequency appears reduced following paclitaxel treatment in aplysia neurons[60]. Mitochondrial transport velocity also appears reduced at the cell level[79] in cortical neurons.

The mechanisms by which paclitaxel disrupts transport remain unclear. Logically, it is possible that microtubule disorganization and bundling could alter transport dynamics. Other possibilities have been noted, such as accumulation of damaged tubulin subunits due to the prevention of microtubule depolymerization[52]. In addition, microtubule associated proteins such as tau have been shown to be able to sterically inhibit motor protein interaction with microtubules at high concentrations[80], and the presence of paclitaxel is well noted to interact with tau binding to microtubules[81]. Finally, paclitaxel induces changes to post-translational modifications of microtubules[82], and motor protein interactions with microtubules are reported to be affected by such modifications[52,83] Overall, while it has not definitely been shown that axonal transport disruptions are the cause of paclitaxel induced neuropathy and not a consequence of other issues in an already degenerating axon, given the observed microtubule abnormalities, the clinical observations of distal to proximal neuropathic progression, and the association of axonal transport deficiencies with other neurodegenerative diseases, axonal transport disruption is a promising mechanism of paclitaxel induced disease pathogenesis.

1.8 Mechanisms of Paclitaxel Induced Microtubule Bundling

While abnormal microtubule bundling has been hypothesized to be related to paclitaxel induced toxicity, the mechanisms by which paclitaxel induces bundling remain unclear. Paclitaxel's binding site is located at the inner lumen of the microtubule[81], and thus, paclitaxel by itself should not induce microtubule cross-linking. Indeed, biochemical analysis[31,84] and electron microscopy[31,84,85] reveal that though paclitaxel greatly enhances microtubule bundling and cross-linking in systems including mixtures of other cellular proteins, isolated microtubules treated with paclitaxel do not show these characteristics. Thus, experimental evidence indicates that paclitaxel stabilized microtubules must interact with other cellular factors to induce cross-linking.

Many proteins within cells interact with microtubules. Broadly, these are categorized as microtubule associated proteins, and they represent likely candidates for influencing paclitaxel induced microtubule bundling *in vivo*. Perhaps the most studied microtubule associated protein is tau, which has been determined to play roles in the pathogenesis of neurodegenerative diseases of the central nervous system. Tau is a major axonal microtubule associated protein, is well known to confer microtubule stability[86,87], and has also been demonstrated to cross-link microtubules both in the presence and absence of paclitaxel[85,88].

Several studies have further implicated potential interactions between paclitaxel and tau. Paclitaxel and tau both occupy similar sites on the microtubule lumen, though tau can also occupy an additional site on the microtubule exterior[81]. Additionally, evidence suggests that tau can induce cooperative binding of paclitaxel to microtubules[89]. Research has demonstrated that paclitaxel induces displacement of tau due to their similar binding sites[81,90], but still other evidence suggests that tau still binds to the exterior of microtubules following paclitaxel treatment[91]. Given that tau is a major microtubule associated protein in axons whose dysfunction is linked to numerous neurodegenerative diseases and that tau can crosslink nearby microtubules in the presence of paclitaxel, tau is a strong candidate for a protein responsible for inducing microtubule bundling following paclitaxel treatment *in vivo.*

1.9 The Interaction Between Neuronal Mechanics and Axonal Transport

Because the neuronal cytoskeleton plays roles in both mechanics and transport, it is likely that the mechanical environment of the neuron plays roles in regulating transport. The mechanical environment has been shown to affect a variety of neuronal parameters including axonal growth rate[92,93], axonal sprouting and guidance[92], and conduction patterns and velocities[94]. In particular, neurons seem notably responsive to tensile loading, and below a certain threshold, increasing strain on an axon via external loading causes a significant increase in axonal growth rate[93]. At rest, nerves exist under tension in the body, and this tension naturally fluctuates growth and during movement, which induces significant strain in nerves[4].

The effects of mechanical loading on neurons are necessarily tied to the cytoskeletal network, which maintains cellular structure and transduces forces through the cell. Microtubule density and cytoskeletal cross-linking has been posited to play important roles in defining the tensile properties of neurons[32,95,96]. In neurons, these same microtubules that are responsible for supporting axonal structure are also responsible for serving as tracks for axonal transport. Given that peripheral nerves undergo considerable loading during movement, it is therefore not surprising that axonal transport machinery is apparently adapted to function during periods of loading. For example, neurons can be stretched at rates well beyond physiological growth rates and appear to respond with increased growth rates in the absence of axonal narrowing[93], implying that transport is not disrupted. Observations of mitochondrial transport in stretched axons have shown that only very large strains cause disruptions in velocity or transport frequency[97]. More robust measures of transport seem to indicate that stretch actually enhances transport by increasing the likelihood of active transport, particularly in the retrograde direction[98]. When strain thresholds are exceeded, microtubules fracture, and axons show bulging indicative of axonal transport failure and subsequently degenerate[33,34].

1.10 Thesis Scope

Given that microtubules are necessary for axonal transport, for maintaining axonal structure, and for bearing mechanical loads, this dissertation discusses research testing whether cytoskeletal perturbation, particularly with paclitaxel treatment, alters the ability of neurons and nerves to accommodate loading.

Chapter 2, published in Experimental Neurology, presents a study that analyzed potential influences of paclitaxel and strain on axonal transport in cultured dorsal root ganglia sensory neurons. Because paclitaxel alters the cytoskeletal structure of an axon by increasing the quantity and aggregation of polymerized microtubules, this study tested the hypothesis that paclitaxel treatment fundamentally alters the ability of a neuron to withstand mechanical loading in a manner that permits normal axonal transport. Such a result would be likely if increased levels of microtubule aggregation result in increased cytoskeletal crosslinking, preventing proper cytoskeletal motion during stretch. This could damage microtubule tracks or cause physical blocking of larger cargoes when an axon narrows during stretch, and result in an inability to maintain functional levels of axonal transport during periods of loading. Results indicate that stretch alone showed minimal effects on axonal transport, paclitaxel treatment resulted in significant transport perturbation, and the combination of both paclitaxel and stretch together led to the largest disruptions in the transport of multiple different cargoes.

Chapter 3, published in the Journal of Biomechanics, presents a study testing the hypothesis that increased microtubule bundling due to paclitaxel treatment will result in alterations to the mechanical properties of whole sensory nerves. Altered nerve properties could potentially decrease nerve performance during joint induced strain, for example, by reducing axonal flexibility and preventing the proper unraveling of axons during nerve stretch, or by altering the natural strain profile of the nerve. When combined with existing deficits in axonal transport, it is plausible that the nerve could accrue enough damage to be permanently impaired. Results indicate that sural nerves treated with paclitaxel show increased microtubule bundling within axons and increased stiffness at various points along the stress-strain curve, including both the linear and non-linear regions.

Chapter 4 presents a study analyzing potential mechanisms of paclitaxel induced microtubule bundling. Prior work suggests that microtubule bundling in the presence of paclitaxel does not occur in isolated microtubules; instead paclitaxel and microtubules together interact with other factor(s) in neurons to induce microtubule bundling[31]. This study tests the hypothesis that the microtubule associated protein tau plays a significant role in paclitaxel induced microtubule bundling. Prior literature indicates that tau has the potential to cross-link microtubules, and that paclitaxel interacts with tau and microtubules together at the molecular level. Results reveal that the absence of tau lessens the severity of paclitaxel induced microtubule bundling in nerves and homogenized brain, indicating a role for tau in contributing to paclitaxel induced microtubule bundling *in vivo.*

Chapter 5 presents a side project published in *Cytoskeleton* unrelated to the effects of paclitaxel on sensory neurons, but related to the broader theme of discovering the effects of cytoskeletal perturbation on the ability of neurons to respond to mechanical loads, in this case, osmotic. This study analyzes the effects of the actin-myosin network on the osmotic regulation of cultured SH-SY5Y neuroblastoma cells. Cells were exposed to hyper- and hypo-osmotic perturbation in the presense of actin or myosin disrupting drugs, and the cytoskeletal, morphological, and cell motility response was assessed at time points up to 30 minutes from the start of perturbation. Results indicated that these cells were unable to restore normal morphology after 30 minutes, and actin and myosin disruption differentially altered the normal cellular response to osmotic loading.

Chapter 6 summarizes conclusions of the dissertation and their significance, and proposes future studies to build upon this body of work.

CHAPTER 2: THE COMBINATORIAL INFLUENCES OF PACLITAXEL AND STRAIN ON AXONAL TRANSPORT

2.1 Summary

Paclitaxel is an effective chemotherapeutic that, despite its common use, often causes peripheral sensory neuropathy. In neurons, paclitaxel binds to and stabilizes microtubules, and through unknown mechanisms, bundles microtubules and disrupts their organization. Because microtubules serve as tracks on which a variety of axonal cargoes are transported, a leading hypothesis for the etiology of paclitaxel-induced neuropathy is that these changes to microtubule organization impair axonal transport. In addition to supporting transport, microtubules also serve a structural role, accommodating axonal extension occurring during axonal growth or joint movement. In light of this dual role for microtubules, we tested the hypothesis that axonal stretch amplified the effects of paclitaxel on axonal transport. Embryonic rat dorsal root ganglia were cultured on stretchable silicone substrates, and parameters describing the axonal transport of three distinct cargoes – mitochondria, synaptophysin, and actin – were measured with and without paclitaxel treatment and axonal strain. Paclitaxel treatment, particularly in combination with stretch, led to severe perturbations in a number of transport parameters, including the number, velocity, and travel distance of cargoes in the axon. Our results suggest that mechanical loading of neurons can exacerbate transport deficits associated with paclitaxel treatment, raising the interesting possibility that paclitaxel influences neuronal function in a multi-factorial manner.

Chapter 2.2 Introduction

Paclitaxel is a taxane used to treat a variety of metastatic cancers, including breast, ovarian, and lung cancer. While effective as an anti-cancer agent, paclitaxel causes peripheral sensory neuropathy in as many as 60% of treated patients[48]. Symptoms are dose dependent and can include loss of sensory function, paresthesia, neuropathic pain, and myalgia. Peripheral neuropathy is generally cited as the dose limiting side effect of paclitaxel treatment[49].

Mechanistically, paclitaxel binds to and stabilizes microtubules. One function of microtubules is to serve as tracks on which kinesin and dynein motor proteins shuttle cargoes along the length of the axon. Because paclitaxel affects the microtubule tracks and induces neuropathic symptoms in a stocking-and-glove distribution, progressing distally to proximally[48], several studies have investigated impairment of axonal transport as a potential cause of neurotoxicity. Accordingly, it is well documented that paclitaxel slows down bulk axonal transport of a wide variety of cargoes, ranging from cytoskeletal proteins to vesicles and organelles[60,77,78,99], presumably due to abnormal microtubule aggregation and organization[31,62].

In addition to their pivotal roles in axonal transport, microtubules also provide structural support in the axonal shaft. In the peripheral nervous system, during phases of organismal growth and due to the movement of spanned joints, nerves undergo significant translation[4] and incur considerable tensile strain (stretch)[6]. The cytoskeleton, including the microtubules, bears loads[23] and is necessarily reorganized during axonal stretch[95,100]. Healthy neurons thus accommodate stretch without being damaged[93]. In fact, an in vitro study suggests that tension is necessary for the survival of neurons[101]. Paclitaxel alters the neuronal response to high strain-rate (traumatic) loading[33] and increases the compressive modulus of neurons[102] and thus may directly impact the ability of a neuron to tolerate deformation. A recent study indicates that deformation-induced mechanical damage can result from cytoskeletal perturbation; intriguingly, mutation of spectrin in a *Caenorhabditis elegans* model resulted in increased damage to axons lengthened during crawling[103].

Recent studies have suggested that tensile strain can modify patterns of axonal transport. While theoretical and experimental evidence suggests that high strain rates fracture microtubules, thus resulting in transport failure[32], lower, physiological levels of stretch are not necessarily detrimental for axonal transport. Specifically, mitochondrial velocity and transport frequency in stretch-grown axons appears unaffected for strains <24%[97]. In addition, *Aplysia* neurons display an increased likelihood of active transport of vesicles following stretch, with a retrograde bias[98]. Beyond these studies, though, despite mechanical and transport roles for neuronal microtubules, very little is known about the interaction between mechanical loading and axonal transport. Here we cultured cells on stretchable substrates integrated in novel microfabricated devices and used high-resolution confocal microscopy to examine the combined effect of stretching and paclitaxel treatment on axonal transport. Specifically, we tested whether paclitaxel impaired the axonal transport of three important axonal cargoes with different functions and transport dynamics – mitochondria, actin, and synatophysin-associated vesicles – and whether axonal stretching amplified this effect. Our results revealed that axonal stretching and paclitaxel synergistically perturbed cargo transport, raising the interesting possibility that paclitaxel influences neuronal function in a multi-factorial manner.

2.3 Methods

Cell culture

Dorsal root ganglia (DRG) were dissected from E15 embryonic rats as previously described[104]. DRGs were digested in trypsin for 30 minutes, collected by centrifugation at 100x gravity, and pre-plated for 75 minutes to minimize the presence of non-neuronal cells. Cells were then recollected and cultured on a stretchable polydimethylsiloxane (PDMS) substrate at the bottom of a 1 x 8 mm micro-cuvette integrated in a custom-built microfabricated device, which was also made out of PDMS (*fig 2.1b*). The PDMS substrate could be continuously extended by up to 17% (as assessed by displacements of beads bound to its surface) along the direction of its shorter (1 mm) dimension. (*fig 2.1a*)Technical details of the device are published elsewhere[105].) Cells were grown in Minimum Essential Media supplemented with 10% FBS, 1% PSN, 50 ng/mL nerve growth factor, and 2% B27 at 37°C for 24-48 hours before imaging.

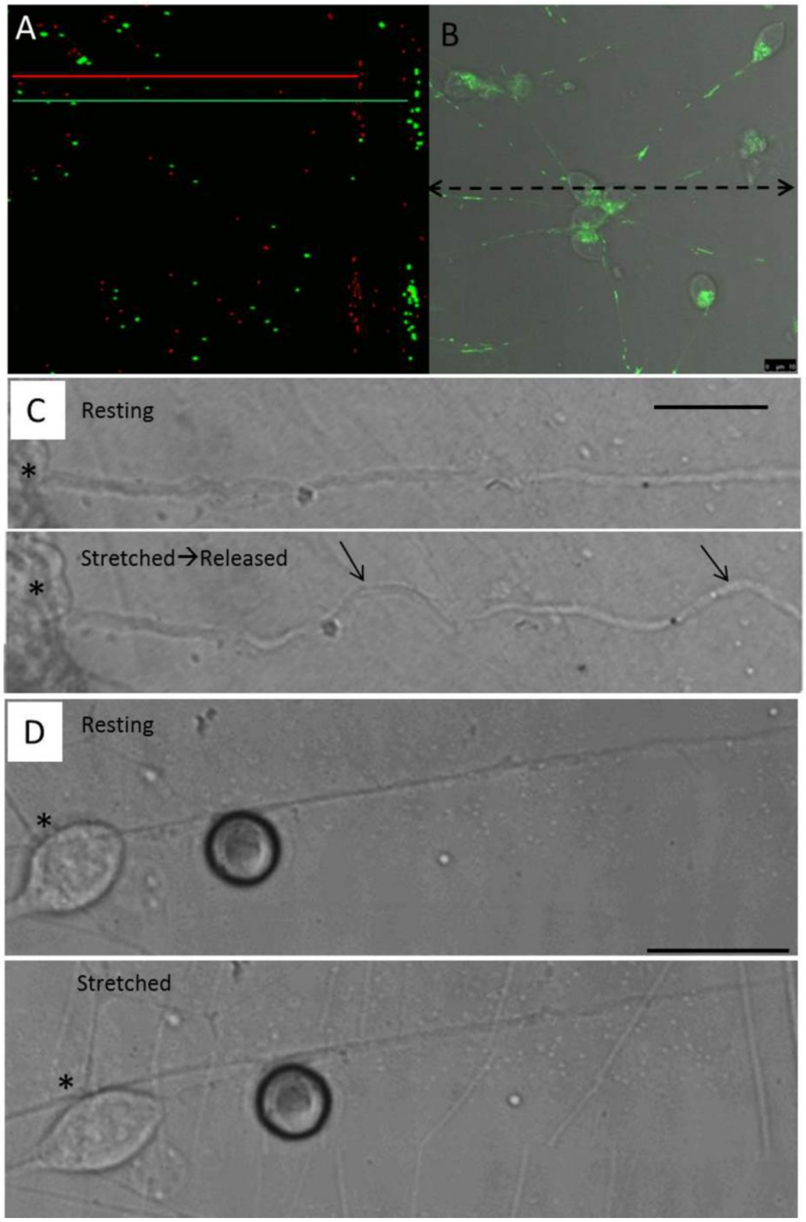

Figure 2.1 – Dorsal root ganglia cells cultured on flexible substrates
a) Beads attached to surface of stretch device before (red) and after (green) stretch. After stretch, pairs of beads attached to the surface appear further apart from one another, allowing for thecalculation of strain. b) Dorsal root ganglia neurons cultured on the stretchable substrate and treated with MitoTracker to show fluorescent mitochondria. Axons are oriented randomly, so only those along the axis of stretch (dashed arrow) + 20 degrees are sampled and analyzed for the effect of stretching on axonal transport. c) Bundle of axons originating from cell bodies located at the left side of the image (*) at rest (top) and immediately after release from stretch (bottom). The axons show undulations (highlighted by arrows) after releasing stretch, indicating that axons remain adherent to the substrate during stretch. Scale bar = 25 μm. D) Unstretched (top) and stretched (bottom) neuron, note the elongation of the cell body (*) post-stretch. Scale bar = 25 μm

Reagents

Paclitaxel (TCI, P1632) was dissolved in DMSO and stored at -20°C as 10 mM culture media for two hours prior to their imaging as well as during the course of the stocks. Cells treated with paclitaxel were incubated at 100 nM paclitaxel in imaging. MitoTracker® Green FM dye (Invitrogen, Carslbad, CA), a fluorescent probe which localizes to mitochondria, was utilized according to manufacturer specifications to visualize mitochondrial transport in DRGs. CellLight® Reagents BacMam 2.0 (Life Technologies), a baculovirus delivery system conferring expression of synaptophysin-RFP and actin-GFP that has been confirmed to infect neurons[106] (and was previously used to study actin flow[107]), was used to visualize synaptophysin and actin transport along DRG axons.

Imaging and analysis

After 24-48 hours of growth, PDMS devices were placed on a Leica SP5 confocal microscope within an environmental chamber (Tokai Hit) which maintained a temperature of 37 º C with constant airflow of 5% CO_2. The stretchable substrates were gradually extended at a relatively low strain rate of ~0.5%/sec (to prevent possible damage from fast extension) up to a maximal strain of 16.8 ± .4% (*fig 2.1c,d*). Cells selected for imaging on stretched substrates had axons aligned ± 20% with the axis of stretch and were imaged during the first 15 minutes post stretch.

DRGs were imaged using a 63x glycerol-water mixture immersion lens (NA = 1.3), and fluorescent images of the cargoes were taken along with either

DIC or brightfield images of the axon. Movies of axonal transport were then assembled with frames taken every 5 seconds for 5 minutes for mitochondria and actin-GFP transport, and every 5 seconds for 90 seconds for synaptophysin-RFP transport. Kymographs were generated from movies using a custom MATLAB script to allow for visualization of mobile and stationary tracks and computation of velocity, movement time, and distance travelled (procedure adopted with modifications from [108]). All transport related parameters were calculated over the entire duration of each movie. Transport of actin in the growth cone was excluded from analysis. In the case of mitochondrial transport, only relatively fast moving cargoes were considered, with those traveling at velocities less than .05 µm/sec ignored due to previously documented low velocity mitochondrial and cytoskeletal drift associated with growth cone induced tension[109].

Transport Parameters

Parameters used to describe mitochondria and synaptophysin-RFP movement included cargo velocity, defined as the average velocity of the cargo while it was in motion, track time, defined as the time a cargo moved without pausing or changing directions, and distance travelled, defined as the distance a cargo moved before it paused or changed directions. Because of frequent pauses and direction changes observed in the kymographs of actin-GFP, to describe actin-GFP movement, we tracked the net displacement of actin-GFP densities during their imaging period. The data was then used to calculate the average velocity of actin during periods of movement. We also analyzed the total time that actin-GFP density was stationary or mobile during the imaging period. Additionally, based on the direction of motion, all resolvable cargoes were scored as anterograde, retrograde, or, in the case of mitochondria, stationary, in order to calculate percentages or numbers of mobile cargoes.

Statistics

Mean values were compared using two-way ANOVA, testing for main effects of paclitaxel treatment and stretch. Because sample sizes varied between groups, likely due to the treatments leading to lower numbers of observations per analysis period, and no significant interaction between main effects was detected in the parameters analyzed, type 2 sum of squares was used in all ANOVA calculations. Post-hoc testing between all groups was performed using the Tukey-Kramer method, which accounts for multiple comparisons. P-values less than 0.05 were considered statistically significant.

2.4 Results

Mitochondrial Transport

To test the combinatorial influences of stretch and paclitaxel treatment on mitochondria transport, we measured a number of parameters; for convenience and clarity, we provided a comprehensive set of mean values of the parameters with significant ANOVA main effects noted (Table 2.1). Key results are presented below. Kymographs from each experimental group are shown (*fig 2.*2a).

Table 2.1 – Mitochondiral transport parameters
Mitochondrial transport parameters presented as means ± standard deviations. Significant main effects of Paclitaxel (P) and Stretch (S) (p<.05) from ANOVA testing are indicated by * next to the category. Each experimental group contains 7-15 axons with 15-50 mobile tracks observed.

Mitochondria Parameters (Mean ±St. Dev)

	- Paclitaxel		**+ Paclitaxel**	
Parameter	**- Stretch**	**+ Stretch**	**- Stretch**	**+ Stretch**
Velocity (anterograde, µm/sec) P:*	0.301 ± 0.127	0.324 ± 0.205	0.222 ± 0.115	0.154 ± 0.057
Velocity (retrograde, µm/sec) P:*	-0.373 ± 0.188	-0.375 + 0.220	-0.235 ± 0.186	-0.165 ± 0.086
Total distance (anterograde, µm) P,S:*	13.800 ± 8.546	9.189 ± 6.057	8.134 ± 4.237	5.116 ± 2.995
Total distance (retrograde, µm) P:*	-17.068 ± 16.307	-10.711 ± 8.921	-8.587 ± 7.808	-8.609 ± 7.527
Percent stationary tracks P,S: *	60.306 ± 21.472	72.794 ± 13.178	79.975 ± 13.671	86.309 ± 11.337
Percent anterograde tracks P:*	17.238 ± 16.683	14.552 ± 7.862	7.550 ± 8.183	3.980 ± 4.743
Percent retrograde tracks P,S:*	23.074 ± 16.614	12.654 ± 10.369	12.474 ± 11.277	9.711 ± 10.768
Track time (anterograde, sec) S:*	51.538 ± 33.698	36.167 ± 29.175	55.385 ± 38.539	33.750 ± 17.061
Track time (retrograde, sec)	48.571 ± 36.753	32.115 + 19.502	39.643 ± 16.108	56.250 + 32.272

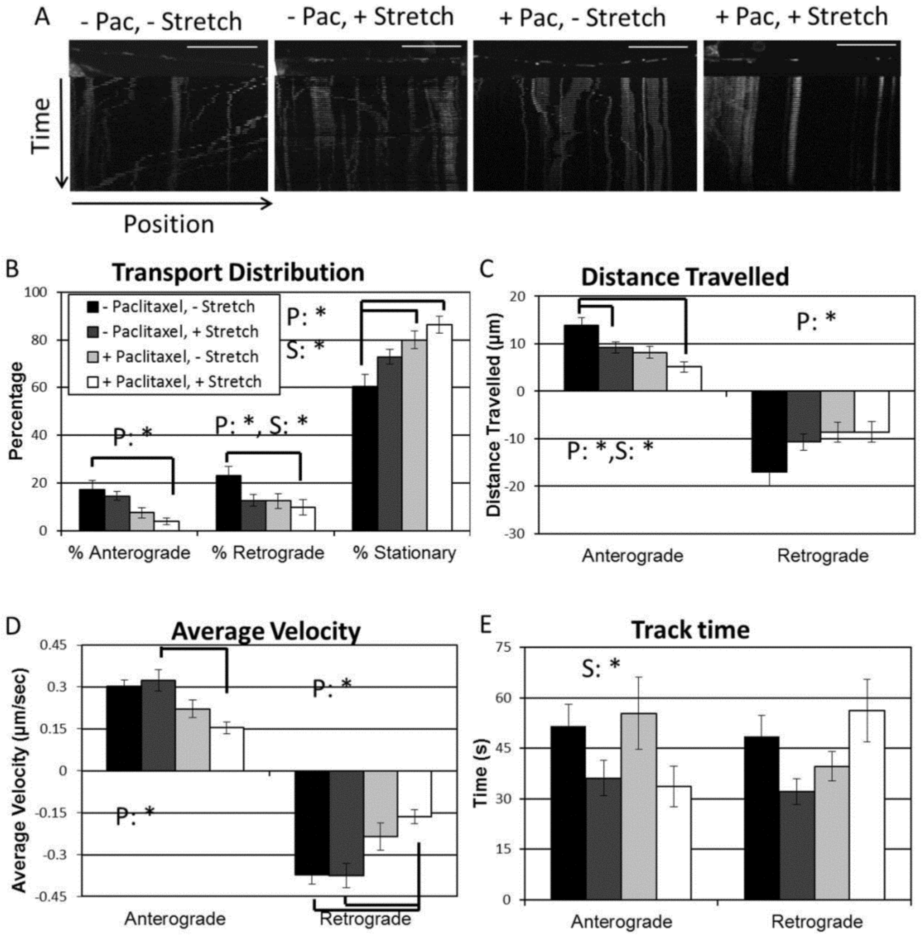

Figure 2.2 – Mitochondrial transport observed with and without paclitaxel treatment and stretch a) Kymographs of mitochondrial transport observed over 5 minutes in axons, from left to right, with no treatment, stretch treatment alone, paclitaxel treatment alone, and paclitaxel treatment in combination with stretch. b) Graphs summarizing the directionality of mitochondrial transport over 5 minute viewing windows under each experimental condition. Paclitaxel treatment causes a significant increase in the proportion of stationary mitochondria; neurons treated with paclitaxel and stretch show the most consistant increase in stationary mitochondria, driven by significant reductions in bidirectional movement. c) Graphs of distances travelled by mitochondria under each experimental condition during 5 minutes of imaging. Stretch and paclitaxel treatment negatively disrupt mitochondria travel distance, with the combination of the two leading to the most consistent decreases in anterograde transport. d) Graphs of velocities of mitochondria under each experimental condition observed during 5 minutes of imaging. Stretch alone has no apparent effect on velocity, while paclitaxel treatment, particularly in combination with stretch, causes large decreases in the velocity of mobile mitochondria. e) Graphs of average duration of a bout of mitochondria movement under each experimental condition observed during 5 minutes of imaging. ANOVA reveals a significant main effect of stretch on anterograde track time, but no post-hoc significance between groups was detected. All error bars represent standard error of the mean. Bars on the graph indicate groups which show a significant (p < .05) difference from each other, as determined by Tukey's HSD. * indicates significant (p < .05) main effects of paclitaxel (P) and stretch (S) from two way ANOVA. Each experimental group contains 7-15 axons with 15-50 mobile tracks observed.

As a first step towards determining the effects of stretch and paclitaxel treatment, we quantified the number and proportion of mitochondria moving anterogradely, retrogradely, or remaining stationary during the imaging period (5 minutes). Under control conditions, axons showed an average of about 60 ± 21% stationary mitochondria, while the remaining mitochondria population equally experienced anterograde or retrograde movement, albeit with large variability from axon to axon (*fig 2.2b)*. Two-way ANOVA showed significant effects of paclitaxel treatment ($p<.005$) and stretch ($p<.05$) on the proportion of moving mitochondria. Post-hoc analysis revealed that paclitaxel alone significantly increased the proportion of stationary mitochondria compared to control ($p<.01$) by suppressing movement bidirectionally ($p<0.10$ for each direction). Stretch alone also trended towards increased proportions of stationary mitochondria, although to a lesser degree than paclitaxel ($p<.10$). The combination of both stretch and paclitaxel treatment led to the most consistent and largest increase in stationary mitochondria ($p<.0005$), driven by significant reductions in both anterograde ($p<.05$) and retrograde ($p<.05$) transport frequencies.

We next examined the directional transport capabilities of mitochondria that did move (i.e., were non-stationary) (*fig 2.2 c-e*). Parameters used to describe cargo movement included cargo velocity, track time, and distance travelled, as defined in the Methods section. Two-way ANOVA revealed a significant effect of paclitaxel treatment on bidirectional velocity ($p<.005$) and distance travelled ($p<.05$), and a significant effect of stretch on anterograde track time ($p<.05$) and distance traveled. Post-hoc analysis largely confirmed ANOVA trends, but additionally further elucidated possible combinatorial effects of paclitaxel and stretch treatment. Paclitaxel treatment alone induced strongly trending, though non-significant, decreases in mean anterograde distance travelled (p=.08), retrograde distance travelled (p = .13) and retrograde velocity (p=.10). Anterograde velocity appeared lower, however, differences were not significant due to high variability in this parameter across axons (p=.33). Stretch alone showed no significant effect on velocity, though it did reduce the anterograde distance travelled (p<.05) by decreasing track time (indicated by ANOVA, though no post-hoc significance was detected due to large data variability).The combination of paclitaxel and stretch led to the largest and most significant reductions in velocity (p<.05 for anterograde compared to stretch alone and retrograde compared to control and stretch treated neurons) and anterograde distance travelled (p<.01), highlighting the inability of paclitaxel treated axons to accommodate stretch.

Synaptophysin-RFP Transport

To test the effects of paclitaxel and axonal stretch on a cargo that undergoes fast transport, a similar analysis was performed on DRGs expressing synaptophysin-RFP. A comprehensive set of mean values of the parameters with significant ANOVA main effects noted (Table 2.2). Kymographs from each experimental group are shown (*fig 2.3a*).

Table 2.2 – Synaptophysin transport parameters
Synaptophysin transport parameters presented as means ± standard deviations. Significant main effects of Paclitaxel (P) and Stretch (S) (p<.05) from ANOVA testing are indicated by * next to the category. Each experimental group contains 16-20 axons with 40-80 mobile densities observed.

	Synaptophysin-RFP Parameters (Mean ±St. Dev)			
	- Paclitaxel		**+ Paclitaxel**	
Parameter	**- Stretch**	**+ Stretch**	**- Stretch**	**+ Stretch**
Velocity (anterograde, µm/sec) P,S:*	0.498 ± 0.303	0.430 ± 0.230	0.307 ± 0.202	0.145 ± 0.069
Velocity (retrograde, µm/sec) P:*	-0.441 ± 0.297	-.483 ± .334	-0.260 ± 0.095	-0.210 ± 0.128
Total distance (anterograde, µm) P,S:*	10.348 ± 11.028	5.878 ± 4.733	6.490 ± 6.326	2.862 ± 2.398
Total distance (retrograde, µm) P:*	-8.388 ± 8.859	-9.881 ± 15.152	-2.951 ± 2.000	-3.034 ± 3.287
Number anterograde tracks P:*	1.667 ± 1.017	1.421 ± 0.961	1.316 ± 0.946	0.824 ± 0.636
Number retrograde tracks P:*	1.667 ± 1.528	1.632 ± 1.739	0.579 ± 0.902	0.765 ± 0.664
Track time (anterograde, sec) S:*	18.638 ± 11.840	13.759 ± 8.622	22.255 ± 14.997	18.185 ± 9.228
Track time (retrograde, sec) P:*	18.674 ± 12.770	17.843 + 11.926	11.621 ± 6.746	14.978 + 8.275

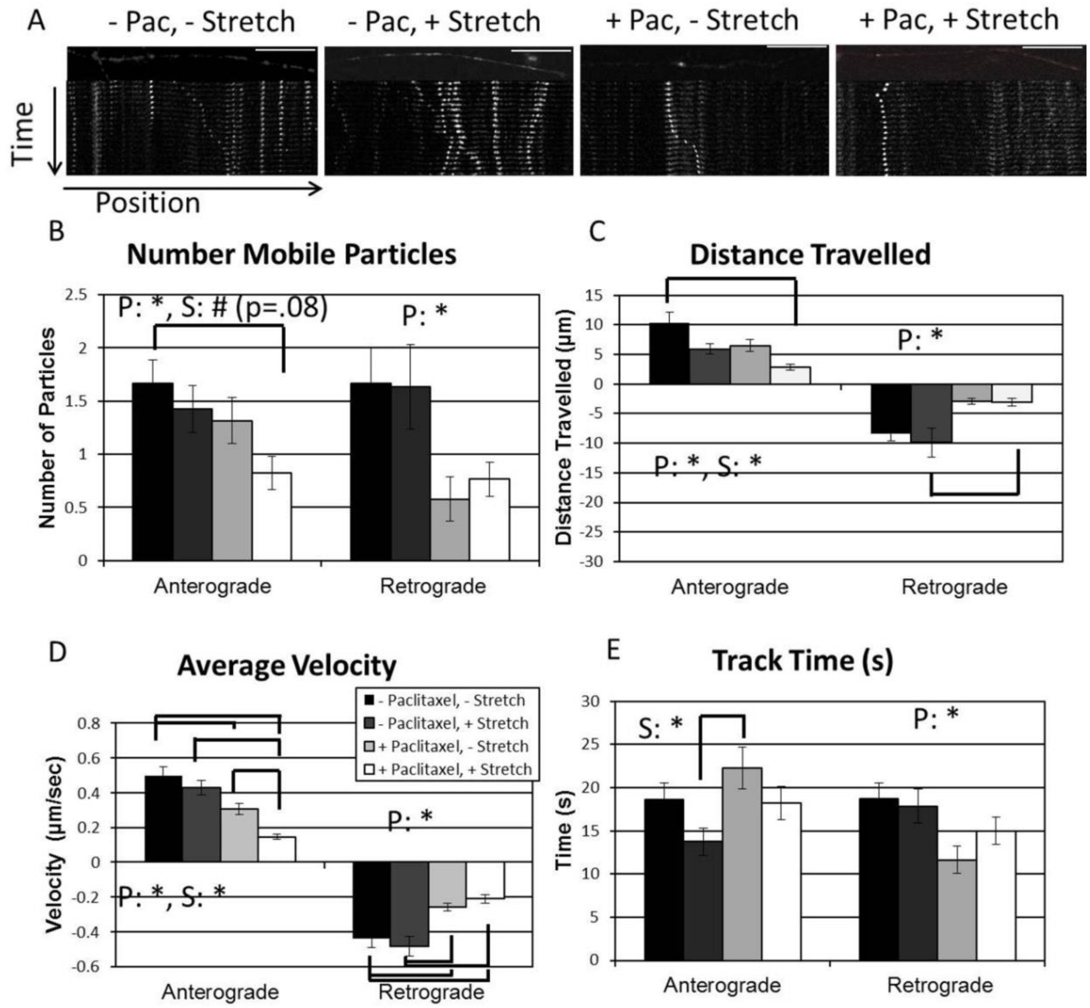

Figure 2.3 – Synaptophysin-RFP transport observed with and without paclitaxel treatment and stretch

a) Kymographs of synaptophysin-RFP transport over 90 seconds in axons, from left to right, with no treatment, stretch treatment alone, paclitaxel treatment alone, and paclitaxel treatment in combination with stretch. b) Graphs of the transport of synaptophysin-RFP over 90 second viewing windows. Neurons treated with paclitaxel in combination with stretch show the least number of detectable mobile particles in the anterograde direction. c) Graphs of distances travelled by synaptophysin-RFP during 90 seconds of imaging. The combination of paclitaxel and stretch leads to the most significant reductions in distance travelled. d) Graphs of velocities of synaptophysin-RFP observed during 90 seconds of imaging. Paclitaxel causes a significant reduction in transport velocity, which is magnified by axonal stretch. In the anterograde direction, paclitaxel alone and paclitaxel + stretch groups show significantly different velocities. e) Graphs of average duration of a bout of synaptophysin-RFP movement observed during 90 seconds of imaging. ANOVA reveals a main effect of stretch in the anterograde direction and paclitaxel in the retrograde direction, but little post-hoc significance was found. Bars on the graph indicate groups which show a significant (p < .05) difference from each other, as determined by Tukey's HSD. * indicates significant (p < .05) main effects of paclitaxel (P) and stretch (S) from two way ANOVA and # indicates a main effect of just outside of statistical significance (p = .08). Each experimental group contains 16-20 axons with 40-80 mobile tracks observed.

Similar transport distributions compared to mitochondria were observed in the transport of synaptophysin-RFP (*fig 2.3b*). Because synaptophysin-RFP particles appeared dimmer and smaller than labelled mitochondria, the total number of discrete particles in an axon could not be reliably resolved. We therefore analyzed the transport of synaptophysin-RFP in terms of raw numbers of mobile particles captured during the imaging period rather than proportions moving in each direction (*fig 2.3b*). Two-way ANOVA showed a significant effect of paclitaxel, but not stretch, on the number of mobile synaptophysin-RFP particles ($p<.05$). Post-hoc testing further revealed a significant reduction in the number of mobile anterograde particles only following the combination of paclitaxel and stretch ($p<.05$), indicating that, as for mitochondria, combining these two treatments leads to the most severe transport perturbation. Both paclitaxel alone and paclitaxel treatment in combination with stretch led to similar, though not quite significant, reductions in retrograde transport frequency ($p<.10$).

We next examined the directional transport capabilities of synaptophysin-RFP particles that were mobile (*fig 2.3 c-e*). Two-way ANOVA revealed a significant effect of paclitaxel treatment on bidirectional velocity ($p<.001$) and distance travelled ($p<.01$) and a significant effect of stretch on anterograde track time ($p<.05$), velocity ($p<.01$), and distance travelled ($p<.01$). Post-hoc analysis showed that paclitaxel treatment alone led to a significant decrease in the bidirectional velocity ($p<.05$) and trended towards a reduction in anterograde distance travelled ($p<.10$) of synaptophysin-RFP. Stretch alone showed no significant effect on velocity, though it did trend towards reduction in the anterograde distance travelled (p<.07). Again, the combination of paclitaxel and stretch led to the most significant reductions in velocity (p<.0001 anterograde, p<.005 retrograde) and anterograde distance travelled (p<.005). In addition, a significant decrease in anterograde velocity was observed in neurons treated with paclitaxel and stretch as compared to neurons treated with only paclitaxel (p<.05), further indicating a combinatorial effect of the two treatments.

Taken together, these data reveal that paclitaxel reduces the velocity and frequency at which both mitochondria and synaptophysin-RFP move, while stretch tends to marginally reduce only the duration of a bout of movement. In combination, however, the two treatments led to an extremely large velocity reduction, causing the largest reduction in distance travelled by mobile particles. Additionally, the least number of mobile particles are observed in neurons treated with both paclitaxel and stretch, further implying that the two treatments synergistically perturb axonal transport.

Actin Transport

We next examined the transport of actin, because we posited that the transport of changes in cytoskeletal stability. Mean values as well as p-values of different parameters from ANOVA are summarized in Table 2.3.

Table 2.3 – Actin transport parameters
Actin transport parameters presented as means ± standard deviations. Significant main effects of Paclitaxel (P) and Stretch (S) (p<.05) from ANOVA testing are indicated by * next to the category. Each experimental group contains 11-17 axons with 15-54 mobile tracks observed.

Actin-GFP Parameters (Mean ± St. Dev)

	- Paclitaxel		**+ Paclitaxel**	
Parameter	**- Stretch**	**+ Stretch**	**- Stretch**	**+ Stretch**
Velocity (anterograde, µm/sec) P:*	0.069 ± 0.050	0.093 ± 0.051	0.032 ± 0.023	0.027 ± 0.013
Velocity (retrograde, µm/sec) P:*	-0.075 ± 0.055	-0.071 ± 0.059	-0.030 ± 0.019	-0.052 ± 0.038
Net Displacement (anterograde, µm)	2.583 ± 2.284	4.098 ± 3.293	1.954 ± 1.801	3.403 ± 3.141
Net Displacement (retrograde, µm)	-3.180 ± 3.287	-2.828 ± -2.925	-1.978 ± 2.080	-2.407 ± 2.561
Total number mobile tracks P:*	3.00 + 2.318	3.727 ± 1.794	1.375 ± 1.204	1.182 ± 0.982
Total number anterograde tracks P:*	1.529 ± 1.125	1.364 ± 0.809	0.563 ± 0.892	0.182 ± 0.405
Total number retrograde tracks P:*	1.588 ± 1.372	2.364 ± 1.690	0.813 ± 0.750	0.909 ± 0.831
Track time (anterograde, sec)	32.586 ± 29.629	28.222 ± 35.212	34.582 ± 36.035	28.625 ± 47.917
Track time (retrograde, sec)	35.376 ± 34.139	43.856 ± 42.065	53.391 ± 54.346	41.541 + 29.577

We focused our analysis on the movement of mobile actin-GFP densities appearing brighter than the ubiquitous actin background (*fig 2.4a),* which have been identified to be predominantly filamentous[110]. Actin transport dynamics were more complex than those of mitochondrial transport, as several densities appeared and disappeared during the imaging window, presumably due to polymerization and depolymerization, respectively. There were also numerous stationary patches of actin, which had varying intensity. Thus, as for synaptophysin-RFP, we measured and compared raw numbers of moving actin densities (5 minute imaging period).

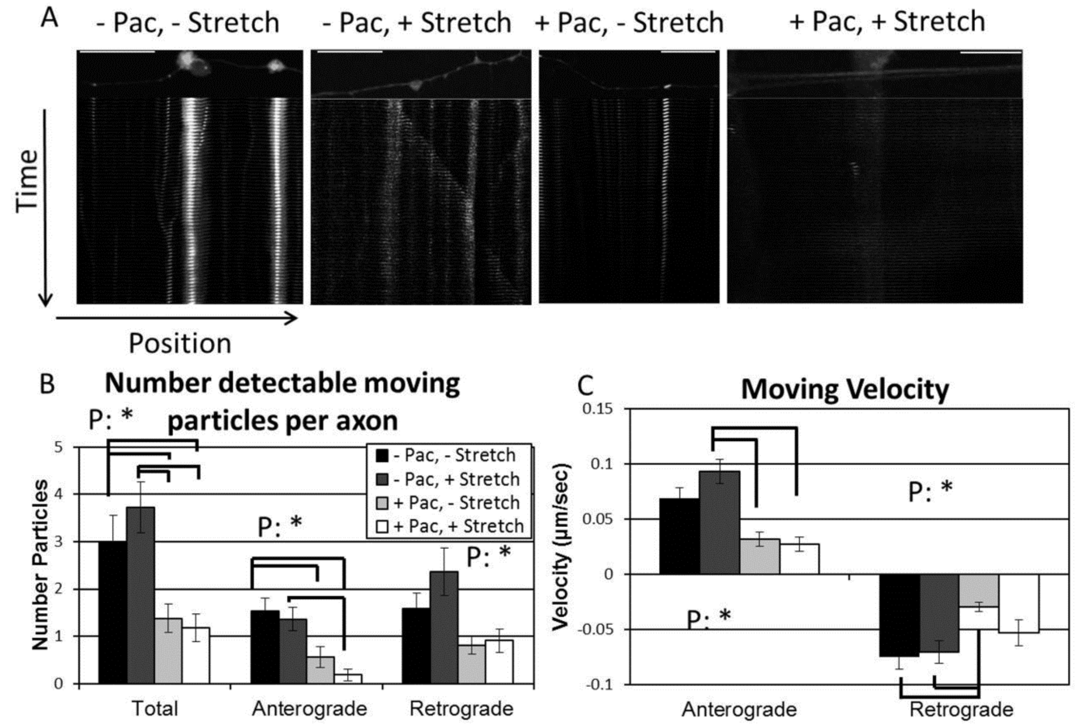

Figure 2.4 – Actin-GFP transport observed with and without paclitaxel treatment and stretch a) Kymograph of actin-GFP transport over 5 minutes in axons, from left to right, with no treatment, stretch treatment alone, paclitaxel treatment alone, and paclitaxel treatment in combination with stretch. (b) Transport distribution of actin densities over 5 minute viewing windows. Paclitaxel treatment causes a reduction in the number of mobile actin densities. Stretch alone has little effect on this parameter. In combination with stretch, very few axons (2 out of 11) showed anterograde movement of actin densities. c) Moving velocity of actin densities observed during 5 minutes of imaging. Paclitaxel treatment causes a reduction in the velocity of mobile actin densities. Stretch alone has little or potentially small positive effects on this parameter. All error bars represent standard error of the mean. Bars on the graph indicate groups which show a significant ($p < .05$) difference from each other, as determined by Tukey's HSD. * indicates significant ($p < .05$) main effects of paclitaxel (P) and stretch (S) from two way ANOVA. Each experimental group contains 11-17 axons with 15-54 mobile tracks observed.

We first analyzed changes in the number and directionality of movement of actin densities in response to paclitaxel treatment and/or stretch (*fig 2.4b*). Paclitaxel treatment caused a significant decrease in the number of anterograde, but not retrograde, densities ($p<.05$). While stretch alone did not change the number of densities moving in either direction, the combination of paclitaxel and stretch caused a massive reduction in the number of anterograde densities (p<.005), with densities in only 2 out of 11 axons showing any anterograde movement. ANOVA showed a significant effect of paclitaxel on the number of mobile densities bidirectionally (p<.005).

As we did for mitochondria and synaptophysin-RFP, we next analyzed changes in the movement characteristics of individual mobile densities. We tracked actin density velocities, net displacements, and directional track times, as defined in the Methods section. Net displacements across all groups were highly variable (Table 2.3). While net displacement trended downward in response to paclitaxel treatment, no significant changes were detected by ANOVA or post-hoc testing. There were no significant differences in anterograde or retrograde track time among any groups.

We also compared directional actin density velocities (*fig 2.4c*). The movement of actin densities was nearly an order of magnitude slower than mitochondrial or synaptophysin-RFP transport. ANOVA revealed a significant effect of paclitaxel treatment on actin velocity in both directions (p<.005). Post-hoc analysis showed paclitaxel treatment alone caused a significant decrease in the retrograde (p<.05) velocity of moving actin densities and a strong trend towards a decrease in the anterograde velocity (p=.08). Stretch alone did not yield significantly different velocity than in control data; in fact, anterograde actin density velocity was significantly higher in stretched neurons than in neurons treated with paclitaxel or paclitaxel in combination with stretch (bidirectionally, p<.05). The combination of stretch and paclitaxel treatment did not cause any significant difference in the velocity of moving actin densities compared to control, though there were few anterogradely moving densities detected at all, potentially rendering this comparison unreliable.

2.5 Discussion

Based on the unique dual role of microtubules, which both contribute to axonal structure and facilitating transport, this study examined the combinatorial effects of paclitaxel and axonal stretch on axonal transport dynamics of cargoes with distinct transport and functional profiles: mitochondria, synaptophysin, and actin (Tables 2.1, 2.2 and 2.3). Paclitaxel reduced transport of all cargoes by most measures, except for duration of a bout of movement (*figs 2.2-4*). Stretch decreased the duration of movement (*figs 2.2,3 e*) and distance travelled (*figs 2-2,3 c*) by mitochondria and synaptophysin, but not their velocity (*figs 2.2,3 d*). However, stretch had minimal effects on the movement of actin densities (*fig 2.4*), confirming the capacity for the cytoskeleton to accommodate deformation. Compellingly, the combination of paclitaxel and stretch severely impaired the movement of all cargoes, showing the largest impairment of bidirectional mitochondrial and synaptophysin transport and of anterograde transport of actin.

Effects of paclitaxel and mechanical loading on mitochondrial and synaptophysin transport

Mitochondrial transport has been previously studied in both untreated neurons[109,111] and paclitaxel treated neurons[60,68,76,79]. Indirect evidence from electron micrograph cross sections of nerves bathed in paclitaxel indicates buildup of organelles[76], including mitochondria[68], suggesting transport impairment. A recent study in rat cortical neurons more directly showed depression of velocities and run lengths after paclitaxel treatment[79], but did not examine changes in the proportion of moving mitochondria. Finally, a single study examined the effect of axonal strain on mitochondrial transport frequency and velocity[97], but revealed impaired transport frequency only at extremely large strains. The data presented in our study agree with much of the previous literature in that paclitaxel treatment reduces mitochondrial velocity and distance travelled, while stretch does not affect mitochondrial velocity or the proportion of transported mitochondria. Also, our control measurements of mitochondrial velocity and distances travelled are similar in magnitude to previously reported literature values, supporting the validity of our quantification methods[79].

Our measured velocities of synaptophysin transport in untreated axons ranged from 0.13 µm/sec to 1.63 µm/sec, which were on the same order of magnitude, but slightly lower on average than the published data[112]. These differences may be due to the fact that prior studies examined synaptophysin transport in networked central neurons rather than DRG axons[112,113]. In addition, our use of a lower frame rate than in prior studies and inclusion of lower velocity movements in reported averages may have contributed to the lower reported mean velocity.

In our study, stretch alone minimally altered transport; however, in combination with paclitaxel, contributed to substantial transport impairment. Thus, paclitaxel, which changes the structure and organization of the axonal cytoskeleton, fundamentally alters the ability of a neuron to respond to mechanical loading. Mechanisms by which this occurred are not clear, however, previous research on traumatic axonal stretch injury provides possible clues. Traumatic stretch has been implicated in microtubule breakage and alterations in axonal morphology, and the structural damage is increased in its extent and persists longer in paclitaxel treated neurons[33,34]. In particular, traumatic stretch injury to cultured neurons at high strain (~30%) and high strain rates caused microtubule breakage, modified the ability of axons to restore tension after unloading, and caused regional bulging suggestive of transport impairment. Thus, microtubule breakage, albeit at a lower level due to the more physiological levels of strain and lower strain rates, may partially explain our observations of decreases in distance traveled and movement duration, in the absence of any changes in velocity.

Effects of paclitaxel and mechanical loading on actin transport

Radiolabeling experiments have indicated that bulk transport of actin may be impaired by paclitaxel treatment[99], but, to our knowledge, the specific processes contributing to this impairment have not yet been analyzed. Moreover, mechanisms of the axonal transport of actin remain largely undescribed, with most studies either focusing on subsets of movement[114,115] or indirect measurements of general cytoskeletal mobility[93,97,116] that have not yet revealed the complex mechanisms of actin transport as a whole. We note that it is well documented that axonal stretch positively regulates axonal growth rate without a reduction in axonal diameter[93,97,117] and accelerated growth of axonal volume should lead to increased demand for structural proteins. Nevertheless, the potential role of stretch in the production and/or transport of cytoskeletal proteins in neurons remains unclear.

In this work, we have begun to address these gaps of knowledge by examining the movement of bright actin densities along the axon in response to axonal stretch and/or paclitaxel treatment. Interestingly, paclitaxel showed a number of deleterious effects on actin transport, suggesting a role for microtubules in the transport or inhibition of transport of actin. Compared to the non-cytoskeletal cargoes analyzed, stretch alone had little effects on actin transport. The exact reason for these differences is unknown, but could be related to the comparatively smaller distances and slower velocities at which actin appeared to move, or differences in the response of load-bearing cargoes (e.g., cytoskeletal elements such as actin) versus non-load bearing cargoes (e.g., organelles) to stretch. However, when paclitaxel treatment and stretch were combined, there was a significant reduction in anterograde actin density movement, again suggesting that paclitaxel treatment leads to deterioration in the ability of neurons to properly adapt to stretch.

2.6 Conclusions and future directions

Several conclusions may be drawn from our findings that stretch and paclitaxel treatment have a synergistic effect on impairing axonal transport. Because paclitaxel treatment led to less frequent bouts of movement of all cargoes analyzed, the drug likely decreased the number of microtubule tracks in an axon capable of supporting transport. Paclitaxel additionally decreased the velocity at which each cargo travelled, indicating altered interactions between motor proteins and microtubules. Alternately, previously observed microtubule misalignment[6] or bundling could lead to slower net movement along the principal axonal vector due to interference with transported cargoes. Axonal stretch typically led to shorter track times, which, in light of previous research, may be indicative of breakage or separation of microtubule tracks, thus leading to shorter bursts of movement for fast moving cargoes. In contrast, actin density transport showed little changes in response to stretch, suggesting that actin transport is regulated differently than the transport of faster moving, non-cytoskeletal cargoes. The combination of both stretch and paclitaxel treatment often led to the largest transport deficits across all cargoes – less functional tracks, shorter tracks, and lower transport velocities are all detrimental to axonal transport.

Our work fills some gaps in the literature by detailing a wide array of effects of paclitaxel treatment and stretching on transport of various cargoes. Most importantly, however, our results indicate that paclitaxel treatment, which changes the structure and organization of the axonal cytoskeleton, fundamentally alters the ability of a neuron to respond to axonal loading. While caution must be used in extrapolating *in vitro* studies to *in vivo* environment, our results raise the currently untested possibility that axonal stretch, such as that induced by joint motion[4,12,118], could exacerbate transport defects associated with paclitaxel-induced neuropathy. Testing this hypothesis provides a compelling direction for future study.

2.7 Acknowledgements

I acknowledge the publisher, Experimental Neurology, for publishing the manuscript presented in this chapter, titled “Combinatorial influences of paclitaxel and strain on axonal transport”. I also acknowledge all of the co-authors (Edgar Gutierrez, Steven Plaxe, Alex Groisman, and Sameer Shah) for their contributions. We gratefully acknowledge funding support from the National Science Foundation (CBET-0932590 and CMMI-1130997, S.B.S.), National Institute of Health (GM098412, E.G. and A.G), the National Skeletal Muscle Research Center at UCSD (S.B.S.), and the UCSD Academic Senate (S.B.S.). We appreciate valuable discussions with Dr. Velia Fowler, Dr. Richard Lieber, the Neuromuscular Bioengineering Laboratory and the Muscle Physiology Laboratory.

CHAPTER 3: PACLITAXEL ALTERS SENSORY NERVE BIOMECHANICAL PROPERTIES

3.1 Summary

Paclitaxel is an effective chemotherapeutic that, despite its common use, frequently causes debilitating peripheral sensory neuropathy. Paclitaxel binds to and stabilizes microtubules, and through unknown mechanisms, causes abnormal microtubule aggregation. Given that microtubules contribute to the mechanical properties of cells, we tested the hypothesis that paclitaxel treatment would alter the stiffness of sensory nerves. Rat sural nerves were excised and soaked in Ringer's solution with or without paclitaxel. Nerves were secured between a force transducer and actuator, and linearly strained. Stress-strain curves were generated, from which tangent moduli and linear elastic moduli were calculated. Paclitaxel treated nerves exhibited significantly higher moduli in both linear and transition regions of the curve. A composite-tissue model was then generated to estimate the stiffness increase in the cellular fraction of the nerve following paclitaxel treatment. This model was supported experimentally by data on mechanical properties of sural nerves stripped of their epineurium, and area fractions of the cellular and connective tissue components of the rat sural nerve, calculated from immunohistochemical images. Model results revealed that the cellular components of the nerve must stiffen 12x to 115x, depending on the initial axonal modulus assumed, in order to achieve the observed tissue level mechanical changes. Consistent with such an increase, electron microscopy showed increased microtubule aggregation and cytoskeletal packing, suggestive

of a more cross-linked cytoskeleton. Overall, our data suggests that paclitaxel treatment induces increased microtubule bundling in axons, which leads to alterations in tissue-level mechanical properties.

3.2 Introduction

Paclitaxel is an effective and common chemotherapeutic that prevents cell division by stabilizing microtubules, thus preventing their depolymerization[119]. Due to its systemic delivery, paclitaxel also accumulates in peripheral nerves, causing a debilitating sensory neuropathy[48]. Because neurons are post-mitotic, mechanisms underlying paclitaxel-induced neuropathy must differ from those affecting dividing cells. Animal models of disease and patients display dying back of axons, reduced epidermal nerve fiber density[120], demyelination[121], altered ion channel activity[75], and disruptions in axonal transport. The latter pathway is commonly hypothesized to underlie neuropathic progression; abnormal clustering of microtubules[31,62,122] is thought to impair delivery of vital proteins and organelles by microtubule-based motor complexes to distal axonal reaches.

Beyond their role in transport, microtubules also play important structural and biomechanical functions in axons[23,95,96], which may also be perturbed by paclitaxel. For example, a recent study demonstrated, using atomic force microscopy, that paclitaxel increases the compressive modulus of cell bodies in cultured dorsal root ganglia[102]. Paclitaxel also alters the response of central neurons to damage during high strain-rate loading[34]. Theoretical studies suggest that microtubules may influence tensile axonal biomechanics[95,96].

Whether and how structural and mechanical changes caused by paclitaxel influence biomechanics and physiological function at the whole nerve level has not been tested. Tensile loading is particularly relevant in peripheral nerves, which span articulating joints and can incur substantial regional strains[4,6,123]. However, deformation beyond normal levels impairs action potential conduction[9]. To protect neurons, strain is partially accommodated by axonal undulations, which straighten upon nerve deformation[14,19]. In axons themselves, maintenance of structural integrity during axonal straightening and subsequent lengthening is likely to be modulated by the cytoskeleton, including microtubules. Increasing microtubule amount, length, stiffness, and bundling through paclitaxel treatment could alter the mechanical response and stability of this delicate biomechanical system, leading to impaired function. This study uses a pure sensory nerve model to test the hypothesis that paclitaxel causes changes in the tensile properties of peripheral nerves. Our data suggest that paclitaxel influences the structure and biomechanics of sensory nerves, supporting a new hypothesis that altered neuronal biomechanics could contribute to paclitaxel-induced sensory dysfunction.

3.3 Methods

Mechanical testing

12 to 20 week old Sprague-Dawley rats were sacrificed and sural nerves were exposed and freed of the surrounding connective tissue bilaterally. A 5mm sural nerve segment just distal to the trifurcation point of the sciatic nerve was tied off with 6-0 nylon sutures *in situ (fig 3.1a)*. Both nerve segments were

excised and randomly assigned to be soaked in Ringer's solution (Aqueous solution of NaCl: 120mM, KCl: 4mM, $MgSO_4$: 0.8mM, $NaHCO_3$: 16mM, glucose: 20mM, and $CaCl_2$: 2.2mM, brought to pH 7.4) with or without the addition of 20µM paclitaxel for 2 hours. Each nerve segment was attached to an Aurora 402A force transducer and linear actuator and stretched in a chamber containing the appropriate Ringer's solution.

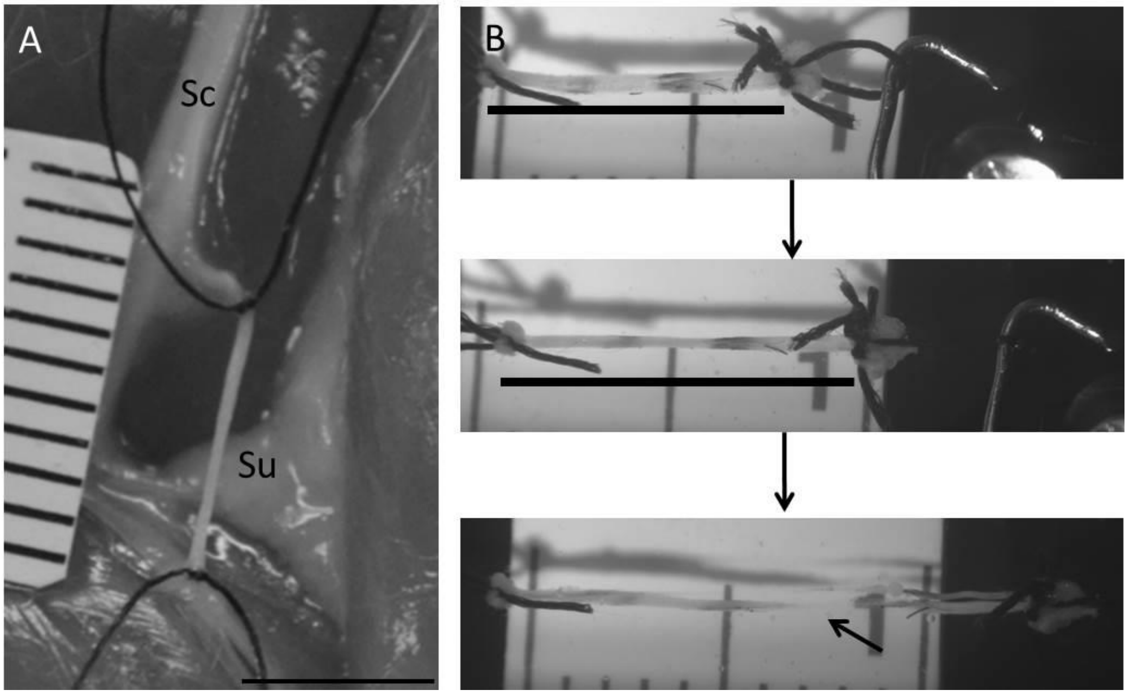

Figure 3.1 – Mechanical testing of sural nerves
A) Sural nerves were exposed in rat cadavers. A ~5 mm segment of each nerve immediately distal to the trifurcation point of the sciatic nerve was sutured *in situ* with 6-0 nylon sutures. Sc and Su indicate the sciatic and sural nerves, respectively. Scale bar = 5mm. B) Each nerve was tied to a force transducer and a linear actuator, and progressively strained over time until visible nerve rupture (arrow). Ink dots along the nerve were used to monitor regional deformation.

The length at which the nerve first incurred detectable passive load was recorded as *L_0*. Nerves were stretched in increments of 0.2-0.5mm at a rate of ~0.05mm/sec and held for 5min before recording the force output, to allow stress relaxation as previously described[124,125]. Because sutures securing the nerve to the force transducer and actuator were initially slack, nerve length was measured from suture to suture from images captured at each incremental deformation (*fig 1b*). All measurements were made blinded as to paclitaxel treatment. We alternately normalized lengths to the length at which nerve stress was equal to 2g-force/mm^2 ($L_{\sigma=2}$). Cross-sectional area was calculated from nerve diameters measured from images captured at L_0, assuming the nerve as a cylinder. Engineering stress-strain (σ-ε) curves were then generated, normalizing to L_0 or $L_{\sigma=2}$. Segmental strains were also measured using ink dots along the nerve, to determine the eventual region of failure.

To test the mechanical properties of nerves without their epineurium, sural nerves were excised as above. The tip of the inner sheath, which extruded beyond the epineurial boundary[126], was held with forceps and the epineurium was manually peeled away. Mechanical testing was performed as above.

The elastic modulus of each curve was calculated as the slope of the linear region of each stress-strain curve at high strains. To compare tangent moduli at specific lower strains preceding the linear region, each stress-strain curve, with strain normalized to $L_{\sigma=2}$, was plotted from ε=0 to the start of the linear region, and fit with an exponential function $\sigma = A*\exp(B*\varepsilon)$ as for other biological tissues[127,128]. A=2, such that σ=2g-force/mm^2, by definition, at ε=0. All curves had R^2 values > .95. Tangent moduli of non-linear regions of each curve were then calculated by the derivative of the exponential curve fit with respect to strain. The strain at which the tangent modulus of the exponential equation equaled the slope in the linear region was denoted as ε_L. The region of the stress-strain curve with $\varepsilon<\varepsilon_L$ are referred to as the transition region.

Because our higher-resolution mechanical testing apparatus was not designed to measure forces larger than 50 grams-force, we performed additional testing on a separate apparatus to measure the ultimate stress of 5 pairs of sural nerves. Contralateral pairs of ~5 mm segments of sural nerves were bathed in Ringer’s solution with or without paclitaxel as above, mounted between a force transducer (Omega, DFG55-5) and a linear actuator, and strained in increments of 0.5 mm every 30 seconds. Maximum force at failure was recorded, and ultimate stress was calculated by dividing the force by the resting cross sectional area of the nerve.

Modeling

The linear portion of the nerve was modeled as a composite tissue comprised of epineurium, inner sheath (perineurium and endoneurium) connective tissue,and a cellular fraction, which were stretched in parallel. The total modulus was expressed as:

$$E_w = A_e E_e + A_{in} E_{in} + A_c E_c \quad (1)$$

where A_i and E_i denote area fractions and modulus, respectively, and subscripts of *w*, *e*, *in*, and *c* refer to those properties of the whole nerve, epineurium, inner sheath connective tissue, and cells, respectively.

Area fractions of the epineurium and inner sheath were measured from immunohistochemical analysis, and the modulus of the epineurium was then calculated from:

$$E_w = A_e E_e + A_{ic} E_{ic} \quad (2)$$

where A_i and E_i denote area fractions and modulus, respectively, and subscripts of w, e, and ic refer to those properties of the whole nerve, epineurium, and inner sheath combined with cells, respectively.

Transmission electron microscopy

C57/Bl6 mice were anesthetized and sural nerves were exposed bilaterally. Smaller mouse nerves enabled us to obtain a more accurate and comprehensive representation of the entire axonal population compared to rat nerves. Nerves were surrounded by a hydrophobic barrier and immersed in Ringer's solution containing 20µM paclitaxel for 2hr. Nerves were then fixed and imaged via electron microscopy. A custom MATLAB script was used to determine the nearest neighbor distance between microtubules and the microtubule density in images of 13 myelinated fibers from paclitaxel-treated and control nerves. Significance between parameters was tested using a Student's t-test (α<0.05).

Immunohistochemistry and Gomori's Trichrome.

10 µM frozen rat sural nerve cross sections were labeled using an anti-laminin primary antibody (1:1000, Sigma Aldrich, L9393) for 1hr at room temperature and Alexa Fluor 488 secondary antibody (1:400, Life Technologies) for 1hr at room temperature. Images were captured on a Leica SP5 confocal microscope with appropriate filters. Gomori trichrome staining was performed as previously described[129].

Image processing

Images of sural nerve cross sections from 3 nerves labeled for laminin were used to calculate the cellular and connective tissue area fractions of the sural nerve. A randomly selected sub-region from an image of each nerve was cropped and manually segmented by tracing the inner area of the laminin rings in ImageJ (*fig 4b-d*). The cumulative areas of the manually segmented regions were divided by the total area of the cropped region, then normalized to dimensions of the whole nerve as measured by trichrome staining (*fig 4a*).

3.4 Results

Because paclitaxel primarily causes sensory neuropathy, we examined the sural nerve, a purely sensory nerve branch of the sciatic nerve. As for many tissues, stress-strain curves showed a toe region in which nerves incurred substantial strains under minimal tension, followed by a transition region in which the nerve stiffened, and finally, a linear region with a constant slope. Strain was normalized to two lengths, L_0, the length at which the nerve first began to incur detectable passive load, and $L_{\sigma=2}$, the length at which the nerve stress was equal to 2g-force/mm^2. This stress was the minimum stress at which nerves visibly began to lengthen and achieved a consistent signal to noise ratio. Representative plots for control and paclitaxel-treated samples are shown (*fig 3.2a and b*), with the latter also illustrating piece-wise curve fits for paired nerves. Raw stress-strain curves for all nerves are also provided (*supplementary fig 3.1).*

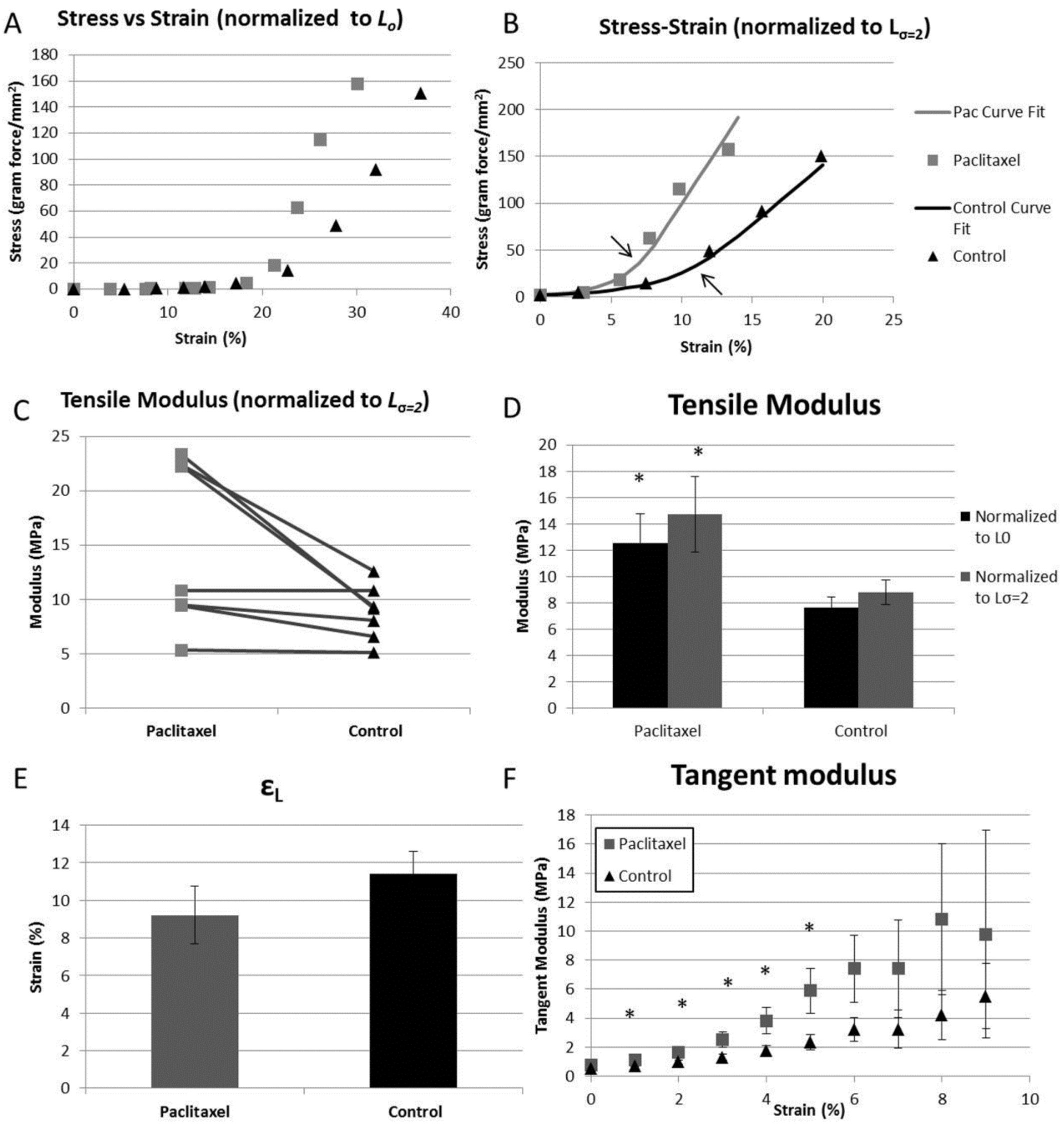

Figure 3.2 – Paclitaxel treatment alters whole nerve mechanical properties
Stress-Strain curves of contralateral nerve pairs soaked in Ringer's solution with and without paclitaxel were generated normalized to L_0 (A) and $L_{\sigma=2}$ (B). Each curve was fit with an exponential function from strain 0 to ε_L, the point at which the slope of the function was equal to the slope in the linear region (arrow). The slope of in the linear region was determined. C) In all cases, the tensile modulus of the paclitaxel treated nerve was greater than or equal to that of the contralateral control nerve. D) The mean tensile modulus of paclitaxel treated sural nerves is significantly (*, P<.05) greater than that of the contralateral control nerves. E) ε_L did not significantly differ between paclitaxel treated and control nerves. F) Tangent modulus calculations in the transition region reveal that paclitaxel significantly increases nerve stiffness (*, P<.05) even at low strains. Error bars indicate standard error of the mean.

We first probed paclitaxel-induced changes to the mechanical properties of the peripheral nerves in the linear regions of stress-strain curves (*fig 3.2a,b*). ε_L, the point defining the start of the linear region (*fig 3.2b*), trended ($p = .115$) towards a lower value in paclitaxel-treated nerves compared to contralateral control nerves (*fig 3.2e*). Paclitaxel-treated nerves were significantly stiffer in their linear region, based on elastic moduli calculated from stress-strain curves normalized both to L_0 and $L_{\sigma=2}$ ($p<0.05$, *fig 3.2c,d*). We also examined the maximum stress in 5 separate pairs of nerves stretched to failure. Most paclitaxel treated nerves showed a higher ultimate stress, however no significant difference was observed, potentially due to one paclitaxel treated nerve failing at a much lower stress than all other nerves (*supplementary fig 3.2).*

To examine biomechanical properties in a more physiologically relevant range of strains [4], we then examined the transition region of the stress-strain curve, which preceded the linear region. Tangent moduli were calculated from the exponential curve used to fit the stress-strain curve between $\varepsilon=0$ to ε_L, and were significantly higher (stiffer) in paclitaxel treated nerves than contralateral control nerves for low strains (ε=1-5%).

To better understand how increased stiffness in individual cells could influence biomechanics of the whole nerve, we developed a theoretical composite-tissue model based on the relative moduli and cross-sectional area fractions of connective tissue and cellular components. As expected, as visible by trichrome labeling, sural nerves displayed, from outside in, clear epineurial, perineurial and endoneurial compartments (*fig 3.3a*). To predict whether and by how much the modulus of the cellular fraction increased after paclitaxel treatment, we required area fractions and moduli of the connective tissue and cell components in untreated nerves. Trichrome labeling revealed the epineurialcross-sectional area to be 24.7 ± 2.7 % (n=3) (*fig 3.3a*). To determine area fractions of the cell and connective tissue compartments of the inner sheath, we labeled sural nerve sections with antibodies targeting laminin, which sharply demarcated cellular boundaries (*fig 3.3b-d*). The cellular area fraction of the nerve was 43.8 ± 0.9 % (n = 3) and the inner sheath connective tissue fraction was 31.1 ± 0.5 % (n=3).

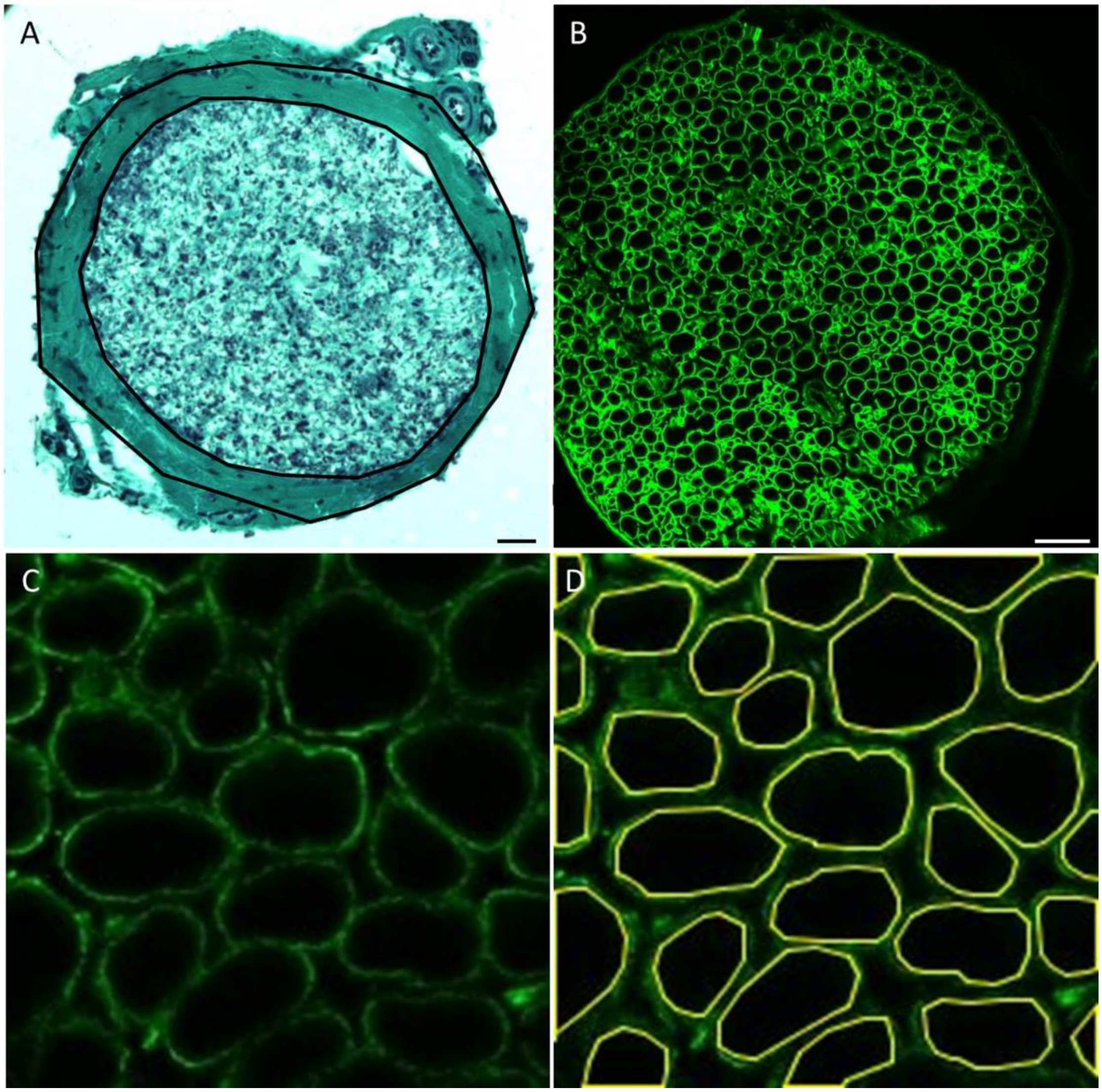

Figure 3.3 – Sural Nerve Histology
A) Gomorri Trichrome stain of a rat sural nerve cross-section, used to calculate epineurial area. Traces indicate sample boundaries from which area fractions were calculated for the inner sheath and epineurial compartments. B) Cross-section of a rat sural nerve stained for laminin. C) In order to estimate the area fraction of the cellular components of the inner sheath, smaller regions of laminin staining were digitally cropped and the inner regions of the laminin rings were manually sectioned in ImageJ (D). Area of the inner rings of laminin relative to the entire cropped region was then computed. Scale bars indicate 25 µm.

We next determined the modulus of the epineurial and inner sheath regions by mechanically testing sural nerves stripped of their epineurium (*fig 3.4a).* Following peeling, the inner sheath still appeared structurally intact (*fig*

3.4b), with expected laminin localization and a visible perineurial boundary. Sural nerves lacking their epineurium were ~5x more compliant than intact nerves (elastic moduli: 1.6 ± .9 MPa vs. 7.8 ± 2.2 MPa, $p<0.001$).

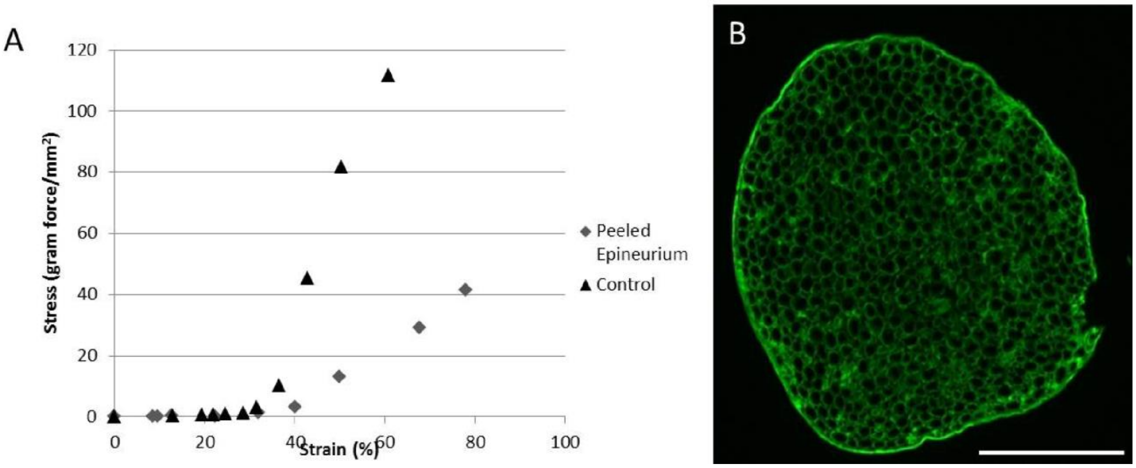

Figure 3.4 – Peeled Epineurium Testing
A) Mechanical properties of sural nerve stripped of epineurium with strain normalized to L_0. B) Cross-section of sural nerve stripped of epineurium labeled with a laminin antibody. Note that the nerve appears structurally intact. Scale bar indicates 100 µm.

Finally, an estimated modulus of the cellular fraction was needed. To our knowledge, mechanical properties of axons excised from peripheral nerves have not been measured. However, several studies have estimated axonal stiffness *in vitro* or through simulations[96,130,131]. We therefore solved our model using axonal moduli ranging from 100 kPa to 1 MPa, based on the range of reported values in these studies Assuming these moduli, the moduli of the epineurium and inner sheath connective tissue fractions were calculated (*equations 1 and 2*). For paclitaxel-treated nerves, the connective tissue moduli was assumed to stayed constant (i.e., no microtubules in this compartment) while the cell fraction modulus was varied. Upon incorporating the modulus of intact nerves following paclitaxel treatment, the modulus of the cellular fraction after paclitaxel treatment was calculated (*fig 3.5a).* Additionally, we calculated a stiffening factor (ration of paclitaxel-treated to untreated cell fraction modulus), as a function of initial cellular fraction stiffness. Results show that the cellular fraction must stiffen 115x to 12x, depending on the initial axonal modulus used (*fig 6b*).

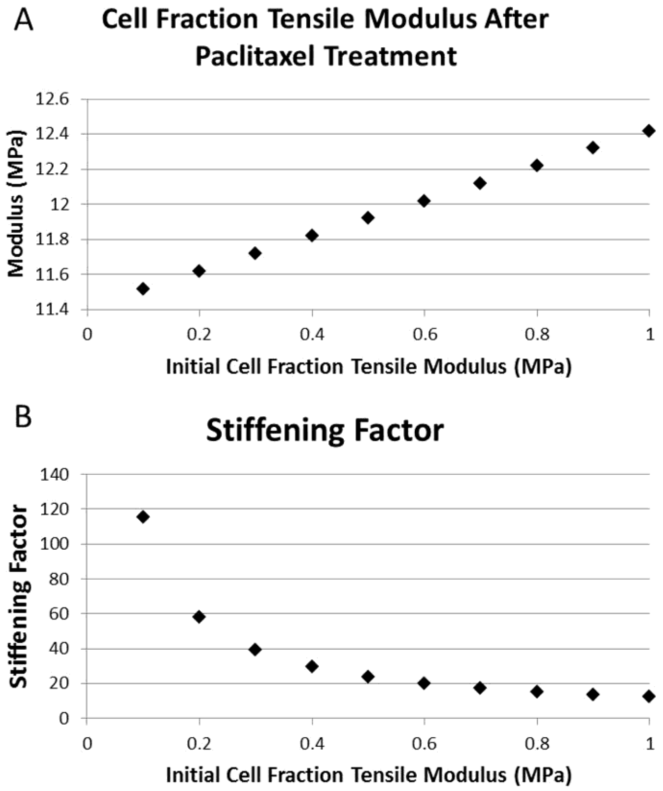

Figure 3.5 – Model of paclitaxel induced stiffening of cells
A) Our composite-tissue model was solved to determine the stiffness of the cell fraction after paclitaxel treatment assuming a range of initial cell fraction moduli. B) After paclitaxel treatment, the cell fraction stiffens significantly.

In an effort to determine a structural basis for biomechanical changes, we next sought to determine the extent by which cytoskeletal structures changed in response to paclitaxel. We therefore treated performed transmission electron microscopy on untreated and paclitaxel-treated rodent sural nerves *in vivo*. Microtubules, other cytoskeletal filaments, and their crosslinks have been suggested to impact cell mechanical properties[23,95]. Because paclitaxel directly affects microtubules, we quantified their density and spacing with and without paclitaxel treatment in myelinated and unmyelinated axons. Paclitaxel treated axons showed frequent clusters of microtubules not present in control axons (*fig 3.6 a-d*) with highly consistent spacing between microtubules (34.88 ± 3.83 nm center to center distance, n=10 pairs), suggestive of a crosslink with a characteristic length. In addition to inducing large microtubule clusters, overall microtubule density and spacing also changed after paclitaxel treatment. In both myelinated and unmyelinated axons, paclitaxel treatment caused a marked increase in the microtubule density of the entire axon ($p<.05$) and decreased the nearest neighbor distance between microtubules ($p<.01$, *fig 3.6e*). The cytoplasmic regions in the paclitaxel-treated nerves appeared darker, with increased cytoskeletal density than the contralateral control. In addition, some paclitaxel treated axons (~9%) appeared to have compacted regions cytoplasm excessively dense with structural proteins (*fig 3.6d*); such malformations were not observed in the control sural nerve. Interestingly, though some cell bodies of non-neuronal cells were interspersed within the extraneuronal space, no microtubules were observed in endoneurial or perineurial compartments, suggesting that these regions are not appreciably changed with paclitaxel treatment. Collectively, these results indicate that paclitaxel treatment increased microtubule, and possibly other cytoskeletal protein, content and connectivity in the axonal shaft, providing a potential structural basis for the observed mechanical changes.

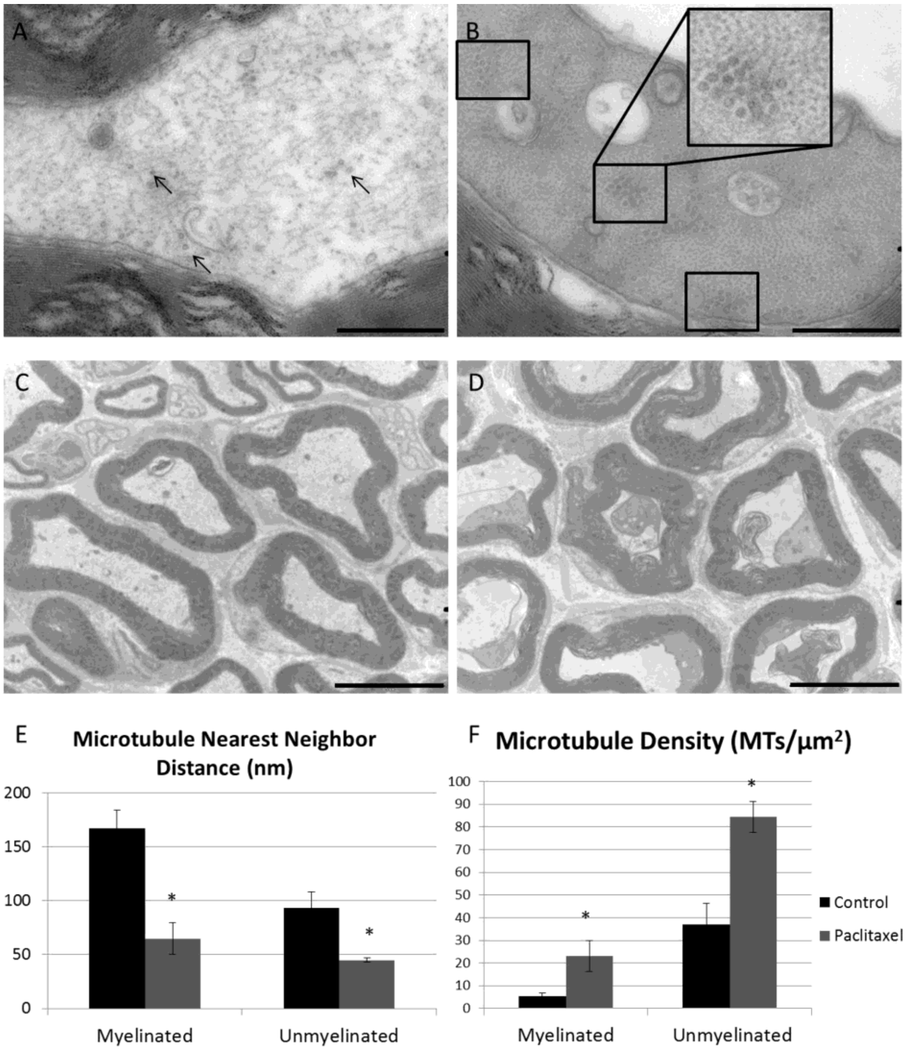

Figure 3.6 – Paclitaxel causes bundling of microtubules in sural nerves
Sural nerves were exposed in anesthetized mice. One sural nerve was surrounded in a hydrophobic boundary and soaked in 20 µM paclitaxel for 2 hours. Mice were sacrificing and paclitaxel treated and control nerves were then fixed for processing. A) TEM image of a myelinated axon within control sural nerves showing expected morphology with microtubules (arrows) scattered throughout the axon B) An axon within a paclitaxel -treated sural nerve shows a contraction of the cytoplasm and buildup of electron dense proteins indicated by the overall darker appearance. Microtubules form clusters of parallel arrays (boxes) and increase dramatically in number. A digitally zoomed inset is provided for increased clarity. C) Control sural nerve axons show intact myelin and axonal structure. D) After paclitaxel treatment, many axons show signs of myelin abnormalities and cytoskeletal collapse. E) Microtubules appear significantly closer together after paclitaxel treatment (*, P<.05). F) Overall microtubule density per axon increases significantly after paclitaxel treatment (*, P<.05). Error bars indicate standard error of the mean. Scale bars indicate 500 nm (A and B) and 5 µm (C and D).

3.5 Discussion

Mechanical properties of paclitaxel-treated sensory nerves

To our knowledge, mechanical testing of sensory nerves such as the sural nerve has not yet been performed, despite sensory branches often spanning joints and being used as autologous grafts. Interestingly, elastic moduli in rodent sural nerves appear to be an over an order of magnitude greater than those of sciatic nerves[132] and slightly lower than those of the porcine laryngeal nerve[133] and rabbit tibial nerve[21]. This could reflect several reasons, including fewer fascicles[134], smaller neurons, and a thicker epineurium relative to the total cross-sectional nerve area, leading to differences in the relative contributions of intra-epineurial fractions to whole nerve properties. In addition, while several studies have suggested that paclitaxel increases microtubule bundling in rat sciatic nerves, few studies have analyzed sensory nerve structure after paclitaxel treatment[70,73], despite the fact that paclitaxel primarily produces sensory neuropathies.

In vitro studies show that paclitaxel nearly doubles the compressive modulus of DRG cell bodies[102], at a much lower dose than that used in this study. Paclitaxel additionally modifies the tensile response of cultured DRG axons[131], and may increase tensile axonal stiffness, though this observation was not discussed by the authors and only reflected a single sample in each group (figures 4 and 11 in[131]). Here we show that cellular properties can influence the tensile properties of a nerve (*fig 3.2*). This finding is consistent with a tensile load-bearing role for intact neurons in nerves of C. elegans[103], which is impaired by destabilizing the spectrin cytoskeleton; however, it contrasts with previous assumptions that the cellular portion of the nerve does not contribute significantly to the stiffness of nerves[4,19,126,135].

When a nerve is stretched, connective tissue and axons, which initially undulate, unravel and begin to accommodate loads[19]. Conventionally, this loading is believed to be primarily borne by the connective tissue, especially the perineurium[4,126], with axonal fibers contributing minimally. This argument is primarily supported by two observations: (i) Wallerian degenerated nerve stumps have similar mechanical properties to intact nerves[135]; and (ii) rabbit tibial nerves stretched past the point of plastic deformation show ruptured perineurium without observation of nerve fiber or epineurial damage[19]. However, conclusions based on these observations could be an oversimplification. In the first case, Wallerian degeneration takes weeks, and could alter the mechanical properties of nerves during that time via extracellular and intracellular remodeling. In the second case, nerve fibers do not remain in a single image plane through their entire course and thus are often observed as discontinuous in 2D images, making confirmation of fiber rupture difficult to observe. Alternatively, axons could be plastically deformed due to cytoskeletal protein breakage, as opposed to cell membrane rupture.

A limitation of our study is that our methods ignore the viscous response of the tissue, which could provide important information regarding changes in nerve properties. Furthermore, because we are unable to visualize the interior of the nerve during stretch, we cannot reliability interpret the integrity of inner sheath tissue and cells from measurements such as ultimate stress (*supplementary fig 3.2*). In addition, the method of paclitaxel delivery to the nerve via local soaking is not a clinical delivery mechanism. However, this approach precludes confounding effects on nerve stiffness or intraneural pressure after systemic delivery, including inflammatory or fibrotic influences. Finally, while the concentration of taxol used here (20 µM) was larger than peak concentrations measured in human subjects[136], several animal models for paclitaxel-induced neuropathy use peak plasma paclitaxel concentrations nearly an order of magnitude higher than those used here[137,138]. Thus, though a direct comparison is difficult, due to the metabolism of systemically injected paclitaxel, the fact that electron microscopy showed significant structural changes within 2 hours, and literature reports also show bundled microtubules in sciatic nerves treated with paclitaxel[139] suggests that our dosage is appropriate for modeling paclitaxel induced neuropathy.

Structural basis for nerve biomechanics

Structurally, mechanical changes correlate with increased microtubule bundling and density. These structural changes are in agreement with previous observations that paclitaxel increases cytoskeletal connectivity in homogenized brain tissue[31] and brine shrimp[84]. Microtubule bundles seen in paclitaxel-treated axons via electron microscopy showed remarkably uniform spacing with center-to-center distances of 34.88 ± 3.83 nm (*fig 3.6b*). Given microtubule diameters of ~25 nm, our data suggest a potential cross-linking (bundling) protein of ~10 nm in length. This dimension is close to but slightly smaller than spacings expected for microtubule crosslinking proteins such as tau (20-27 nm[140]) or dynein (consisting of a 13-15 nm diameter ring and a 10-15 nm length stalk[141]), suggesting other microtubule associated proteins may be involved. Neurofilaments also appear to be more densely packed around microtubule bundles (*fig 3.6b,d*), though their potential role in nerve mechanics remains to be determined. Finally, the perineurium contains densely packed layers of cells[142] – we cannot exclude the possibility that nerve stiffening was due to mechanical changes in the perineurial cells, though electron microscopy (*fig 3.6*) does not indicate many microtubules in these cells[142].

Because the cytoskeleton anchors the cell to the surrounding extracellular matrix, a more networked cytoskeleton could also alter the way axons strain with respect to their surroundings. Stiffer axons or altered adhesion between the cell and its extracellular environment could alter the unraveling of undulating axons, or change the relative extension of cells and their surrounding matrix under asymmetric loads (e.g., shear). These less intuitive possibilities could additionally amplify the mechanical effects of paclitaxel.

Model parameters and predictions

Our model of nerve mechanics relies on several parameters relating to the stiffness of connective tissue and cells within the nerve which have not yet been reported. Interestingly, though the perineurium is suggested to be the primary load bearing tissue in nerves[19], peeling of the epineurium dramatically decreased nerve stiffness and tensile modulus (*fig 3.4*), indicating that the epineurium contributes significantly to the overall stiffness of the sural nerve, and is likely to be engaged during tensile loading.

In addition, values of the tensile modulus of the cellular fraction of untreated nerves were also necessary to determine the stiffening effects of paclitaxel. Several *in vitro* and *in silico* studies have been performed to measure or estimate the stiffness of axons. The Young's modulus of PC12 neurites grown *in vitro* has been experimentally measured to be 12 ± 2 kPa[130]. However, PC12 neurites are ~10 times more compliant than DRG axons[131], and so this value was not used. Cultured DRG neurites show a wide range of diameters from .05 to 1.20 µm[143] with a median diameter of 0.24 µm; using data from figure 4 in[131] and the median reported cultured DRG diameter of 0.24 µm, one can roughly estimate the modulus of a cultured DRG axon to be ~90 kPa. Finally, axonal moduli have been determined via modeling to be ~1 MPa[96]. The authors reconcile this difference with the above papers by noting that *in vitro* studies use short axons where the tensile modulus is calculated based on force measurements taken from the entirety of the axon; the weakest point along the axon therefore dominates stiffness measurements. The axon does not necessarily show a uniform distribution of microtubules along its length[96,144] and therefore such *in vitro* studies may underestimate stiffness. Our model shows that paclitaxel treated cells must stiffen considerably (≥ 12x) to cause the observed results, suggesting that paclitaxel induced changes to tensile mechanical properties of cells are dramatic.

3.6 Conclusions

Nerves necessarily experience substantial strains during joint movement, including regional deformations of 20-30%[4,6,123]. Our results suggest that paclitaxel stiffens sensory nerves, consistent with morphological observations of increased microtubule packing and density. If these changes alter the magnitude or distribution of strains along a nerve or impair axonal unraveling, thus forcing axons to incur larger loads than normal, nerve fibers could be damaged by simple daily movement. Though this idea is currently highly speculative, altered nerve mechanics may thus influence neuropathic progression. Such damage may impact cell function directly, due to microtubule breakage, such as that observed in neurons loaded at high strain rates [33], or indirectly, by amplifying axonal transport defects[145] . Given the possibility of a mechanical contribution to neuropathy, the physical management of patients treated with paclitaxel, including the development of effective post-chemotherapy immobilization or physical therapy protocols, warrants further investigation.

3.7 Acknowledgements

I acknowledge the Journal of Biomechanics for accepting the manuscript presented in this chapter for publication, titled “Paclitaxel alters sensory nerve biomechanical properties.” I also acknowledge the co-author, Sameer Shah, for his contributions. We gratefully acknowledge imaging by Dr. Malcolm Wood at the Scripps Research Institute electron microscopy core facility, and support from the National Science Foundation (CBET1042522), U.S. Army Medical Research and Materiel Command (W81XWH1010773), and the UCSD Academic Senate.

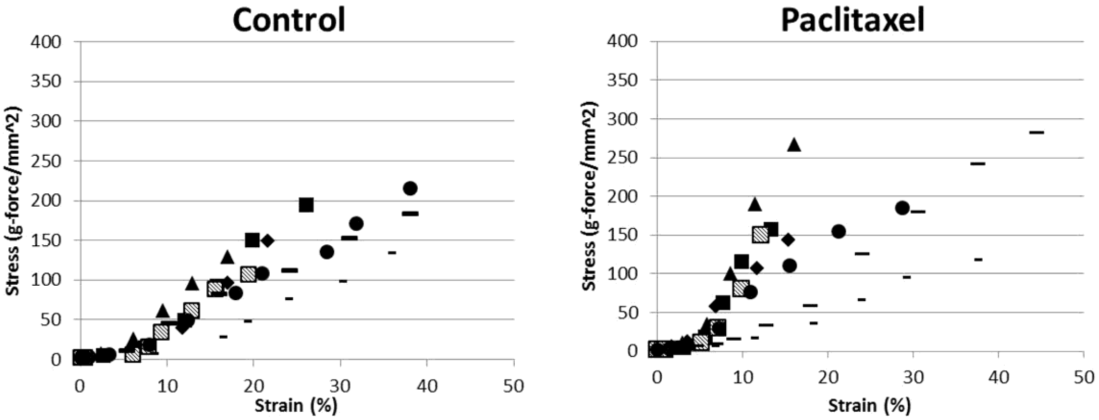

Supplementary Figure 3.7 – Stress-Strain curves of sural nerves
Stress-strain curves of sural nerves with and without paclitaxel treatment with strain normalized to $L_{\sigma=2}$. Note that in general, stress-strain curves appear steeper after paclitaxel treatment.

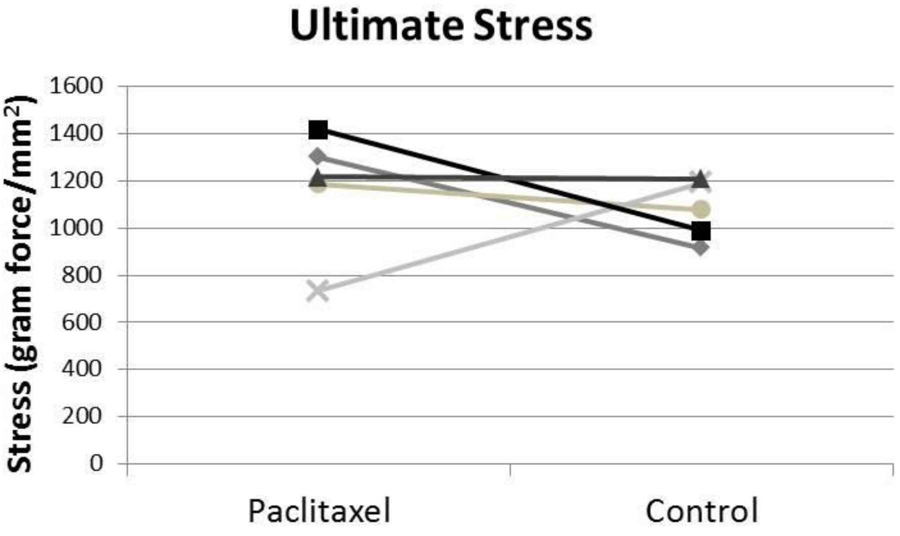

Supplementary Figure 3.8 – Ultimate stresses of sural nerves
Ultimate Stresses measured from 5 pairs of sural nerves stretched to failure. No significant difference between groups was detected; however, barring one nerve pair, paclitaxel treated nerves typically experienced higher ultimate stresses.

CHAPTER 4: TAU INFLUENCES PACLITAXEL-INDUCED MICROTUBULE BUNDLING IN NEURONS

4.1 Summary

Paclitaxel, also known by its brand name taxol, is a chemotherapeutic that despite its clinical success causes patients to develop peripheral sensory neuropathy in high frequencies. Mechanistically, paclitaxel binds to and stabilizes microtubules, making them resistant to depolymerization. While the etiology of neurotoxicity of paclitaxel remains unclear, studies hypothesize that abnormal microtubule bundling and organization that have been observed to follow paclitaxel treatment ultimately result in functional impairment. Prior experimentation has suggested that intracellular factors interact with paclitaxel or paclitaxel stabilized microtubules to result in microtubule bundle formation. However, the primary factor(s) responsible for this phenomenon remain unclear. In this study we investigated whether tau, a common MAP in axons known to confer microtubule stability and regulate microtubule crosslinking, is a primary factor responsible for paclitaxel induced microtubule bundling *in vivo.* We compared microtubule bundling in sensory nerves and homogenized nervous tissue extract from tau knockout and wild type mice treated with paclitaxel using electron microscopy and biochemical assays. Results revealed that tau knockout mice exhibited less bundling of microtubules following paclitaxel treatment than wild type mice, suggesting tau may play a role in the development of these structural abnormalities. Finally, we performed sensory assays following systemic delivery of paclitaxel, which indicated that tau knockout mice were still

susceptible to neuropathy, suggesting that the reductions in microtubule bundling observed were not sufficient to prevent neurotoxicity.

4.2 Introduction

Paclitaxel is a powerful chemotherapeutic that is used to treat a variety of metastatic cancers including breast, ovarian, and non-small cell lung cancer[49]. Mechanistically, paclitaxel binds to and stabilizes microtubules, promoting their assembly[119]. In addition to altering typical microtubule polymerization kinetics, paclitaxel decrease the number of protofilaments composing microtubules[55] as well as the stiffness of individual microtubules[146]. Collectively, these actions disrupt the intricate microtubule dynamics required for cell division.

Because it is delivered systemically, paclitaxel is also toxic to post-mitotic cells, especially neurons. Consequently, a frequent and dose limiting side effect is the development of peripheral sensory neuropathy, which includes symptoms of hyperalgesia, alloydnia, neuropathic pain, and paresthesia[48]. Structurally, neurons and other cell types appear to develop abnormal microtubule bundles upon direct exposure to paclitaxel[68,139,147]. Functionally, neurons show impaired axonal transport of a wide variety of cargoes[60,77,78,99]. Axonal transport deficits have therefore been hypothesized to play a role in the development of paclitaxel induced neuropathy. Due to the critical role that microtubules play in intra-axonal transport, the cause of these deficits has been presumed to be directly connected to the observed alterations to microtubule organization[49], though other mechanisms of transport disruption such as alterations to microtubule post-translational modifications and deleterious interactions with microtubule associated proteins (MAPs) have also been proposed[52].

Despite the fact that initial observations of axonal microtubule bundling following paclitaxel treatment occurred several decades ago[31,147], the mechanisms by which paclitaxel induces microtubule bundling in axons still remain unclear. *In vitro* studies have revealed that microtubules composed of purified tubulin do not bundle in the presence of paclitaxel[31,85]. However, in homogenized tissues, paclitaxel induces microtubule bundling and crosslinking as evidenced by electron microscopy and centrifugation assays[31,84]. The natural conclusion is, therefore, that some factor(s) within cells interact with paclitaxel or microtubules stabilized by paclitaxel to form such bundles.

MAPs are likely candidates for influencing paclitaxel induced bundling *in vivo*. Specific to axons, tau is a major MAP that confers microtubule stability[81,148]. Tau can bind to microtubules, and is also capable of dimerizing with other nearby tau proteins[140]. Experimentation has revealed that tau is capable of cross-linking microtubules both in the presence of paclitaxel and in its absence in high concentrations[85]. A number of studies have detailed potential interactions between paclitaxel and tau. For example, paclitaxel and tau both occupy similar binding sites on the inner lumen, though tau also can bind to an additional site on the exterior of microtubules[81,89,149]. In addition, evidence suggests that tau is displaced from microtubules upon exposure to paclitaxel[81,90,150], and high concentrations of tau appear to cause paclitaxel to cooperatively bind to microtubules[89]. Despite these observations, paclitaxel treatment also induces tau dephosphorylation[91], which enhances its binding affinity for microtubules, and tau can still binds to microtubules after paclitaxel treatment. Finally, microtubule destabilization seen in tauopathies can be ameliorated with paclitaxel treatment[151].

Though many experiments have detailed interactions between tau and paclitaxel and there is a large body of evidence detailing tau's roles in diseases of the central nervous system[152-154], little is known about potential roles of tau in peripheral neuropathy. Given that tau is a major microtubule associated protein in axons whose dysfunction is linked to numerous neurodegenerative diseases, that tau appears to interact with paclitaxel, and that tau can crosslink nearby microtubules in the presence of paclitaxel, we sought to determine if tau was required for microtubule bundling in neurons by utilizing electron microscopy and a biochemical fractionation assays.

4.3 Methods

Transmission electron microscopy

Tau Knockout (strain: $\mathrm{Mapt}^{\mathrm{tm1(EGFP)Klt}}$/J, Jackson Labs) and wild type C57/Bl6 mice were anesthetized and sural nerves were exposed bilaterally. Nerves were surrounded by a hydrophobic barrier and immersed in Ringer's solution containing 20µM paclitaxel for 2hr. Nerves were then fixed and imaged via electron microscopy. A custom MATLAB script was used to determine the nearest neighbor distance between microtubules and the microtubule density in images of 13 myelinated fibers from paclitaxel-treated and control nerves.

Tissue Centrifugation

8 week old Tau knockout and wild type mice were sacrificed and their brains were removed. Brains were homogenized in MEM buffer (100 mM MES, 1 mM EGTA, 1 mM $MgSO_4$, pH 6.75) supplemented with a protease inhibitor cocktail and subjected to a series of centrifugations as previously described. Briefly, each brain homogenate was first centrifuged at 200,000x g at 4^oC. The supernatant from each brain was collected (henceforth referred to as brain extract), supplemented with .05 mM GTP, divided into two groups with one group receiving with 35 uM paclitaxel, and incubated at 30^oC for 30 minutes. Each sample was collected, placed atop a 1 mL 35% sucrose cushion, and centrifuged at 150,000x g for 15, 45, or 120 minutes. Following centrifugation, the supernatant, sucrose cushion, and protein pellets were collected for further analysis. Total volumes of each sample were recorded at each step. A schematic detailing this process is shown in *fig 4.1*.

50 ug purified tubulin was suspended in 200 uL MEM buffer, supplemented with .05 mM GTP, divided into two grouips with one group receiving with 35 µM paclitaxel, and incubated at 30^oC for 30 minutes. Each sample was collected, placed atop a 1 mL 35% sucrose cushion, and centrifuged at 150,000x g for 15, 90, or 240 minutes. Following centrifugation, the supernatant, sucrose cushion, and protein pellets were collected for further analysis.

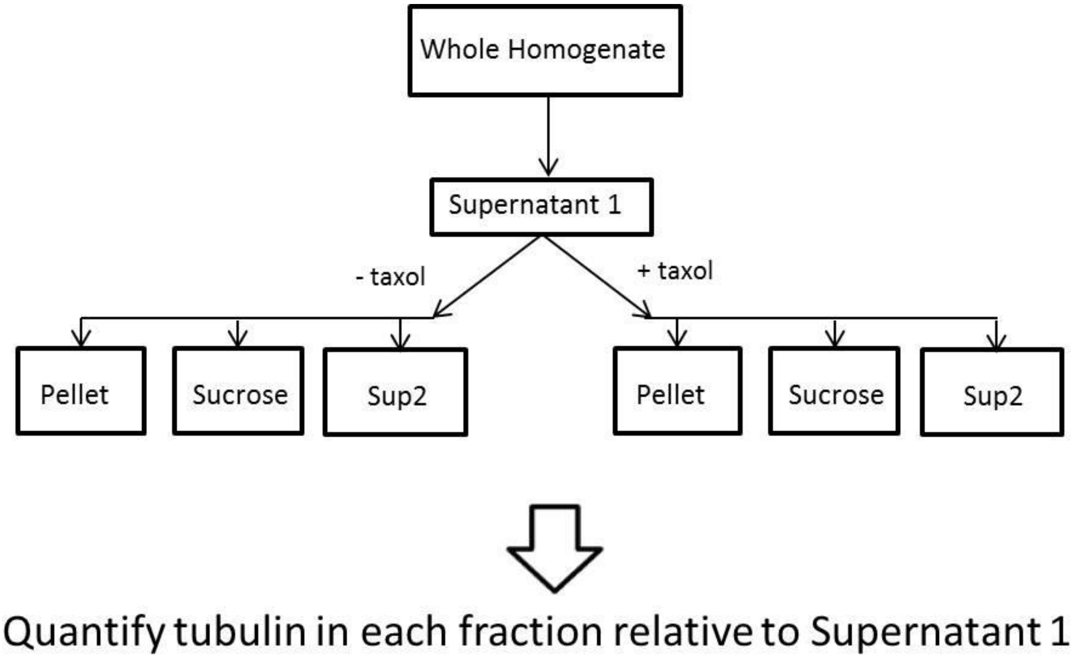

Figure 4.1 – Centrifugation assay work flow
Brains were homogenized and centrifuged at 200,000x g, and the supernatant was collected (Supernatant 1). This extract was then divided into two groups, with one treated with paclitaxel and the other serving as a control group, and centrifuged through a 35% sucrose cushion. Each fraction (supernatant 2, sucrose, and pellet fractions) were collected and tubulin was then quantified relative to the original tubulin present in supernatant 1.

Western blotting

After centrifugation and collection, each brain was subdivided different groups as defined in *fig 4.1*. Total protein in each group was quantified using the Pierce BCA assay. Western blots were then performed to quantify the relative tubulin quantity in each group. Briefly, samples were mixed with criterion xt sample buffer and reduced agent, heated at 95^{o}C for 5 minutes, loaded into 3-8% tris acetate gels, and electrophoresis was performed in tricine running buffer at 110 volts for 90 minutes. Wet transfer to a nitrocellulose membrane was then performed in Towbin buffer with 20% methanol at 200 mA for 2 hours. Membranes were then blocked in 5% milk in TBS-T for 1 hour, incubated in anti-tubulin antibodies overnight at 4^{o}C (1:1000 in TBS-T and 5% BSA), rinsed 3x, and incubated for 1 hour at room temperature in anti-mouse secondary antibodies. Membranes were there imaged using the Bio-Rad chemilumiscent kit according to manufacturer specifications.

Quantification

Western blot images were quantified using Image Lab with the goal of tracking the relative amount of tubulin in each group such that all of the tubulin in the supernatant 1 fraction could be tracked through the supernatant 2, sucrose, and pellet fractions. Integrated pixel intensities from each sample were normalized to the signal from the whole homogenate and supernatant 1 fractions of each brain according to the equations: $I_{N_i} = I_i / I_{whole/sup1}$, where I_{N_i}represents the normalized intensity of sample *i,* I_i represents the intensity of *i,* and $I_{whole/sup1}$ represents the intensity of the whole homgenate or supernatant 1 fractions of the brain being analyzed . The volume fraction of each sample loaded into each gel was calculated as $V_{f_i} = V_i / V_{i_{total}}$, were V_{f_i} represents the volume fraction of *i*, V_i represents the volume of the sample loaded into the gel, and $V_{i_{total}}$represents the total volume of each sample collected. The total tubulin in each sample, in arbitrary units, was then calculated from: $T_{tub} = I_{N_i} / V_{f_i}$, where T_{tub} is the total tubulin in the sample. In order to assure that quantification of western blots was accurate, different volumes of each sample were loaded gels such that subsequent band intensities fell within the linear region of quantification where integrates pixel intensities linearly scaled with concentration.

Paclitaxel treatment

Tau knockout and wild type mice were injected intraperitoneally with paclitaxel (4 mg/kg) for 4 consecutive days. Paclitaxel was dissolved in a 50:50 mixture of Cremophor EL to a concentration of 2 mg/mL, and then diluted in a 0.9% NaCl solution to a final concentration of 0.5 mg/mL before injection. Total injection volume was 8 mL/kg. A separate group of tau knockout and wildtype mice were injected with the Cremophor EL, ethanol, and NaCl solution as a vehicle control. Mice were assessed using the Von Frey hair test and tail withdrawal test as described above prior to treatment, after 2 days of treatment, and after 4 days of treatment.

Sensory Assays

Mechanical allodynia was assessed using the Von Frey hair test. The 50% response threshold was determined using a modified version of the Dixon Up-Down method. Briefly, Von Frey hairs of progressively increasing stiffness were applied to the hind paw of the mice, beginning with a .4 gram force filament, until a pain response (flinching of paw or licking of paw) was observed. After a positive pain response, the previous, incrementally less stiff filament was then applied. If there was no response, the next incrementally stiffer filament was applied. The process is repeated until 5 test points, including the first response, were recorded, and the 50% withdrawal threshold was then calculated.

Thermal hyperalgesia was assessed using a tail withdrawal test. Mice were secured in a custom restraining device and approximately half of the mouse tail was immersed in a water bath at 49 or 50 ^{o}C. The time to pain response (flicking of tail, attempts at tail withdrawal, or successful tail withdrawal) was measured.

Statistics

Nearest neighbor distances from electron microscopy were analyzed using a Two-Way ANOVA with factors of genotype and drug treatment (± paclitaxel), with post-hoc comparisons using Tukey's HSD. Differences between groups from the centrifugation assay and Von Frey analysis were determined using a Student's t-test. In all cases, significance was noted as $p<.05$.

4.4 Results

Electron Microscopy

To test the influence of tau on microtubule bundling in nerves due to paclitaxel treatment, we first performed electron microscopy on nerves externally bathed in paclitaxel *in vivo* in wild type and tau knockout mice. Because paclitaxel primarily induces sensory neuropathy, we chose to examine sural nerves, a purely sensory branch of the sciatic nerve. Under control conditions without paclitaxel treatment, nerves from both the wild type and tau knockout appeared as expected, with populations of myelinated and unmyelinated axons and visible cross sections of microtubules scattered throughout each axon (*fig*

4.2a-f).

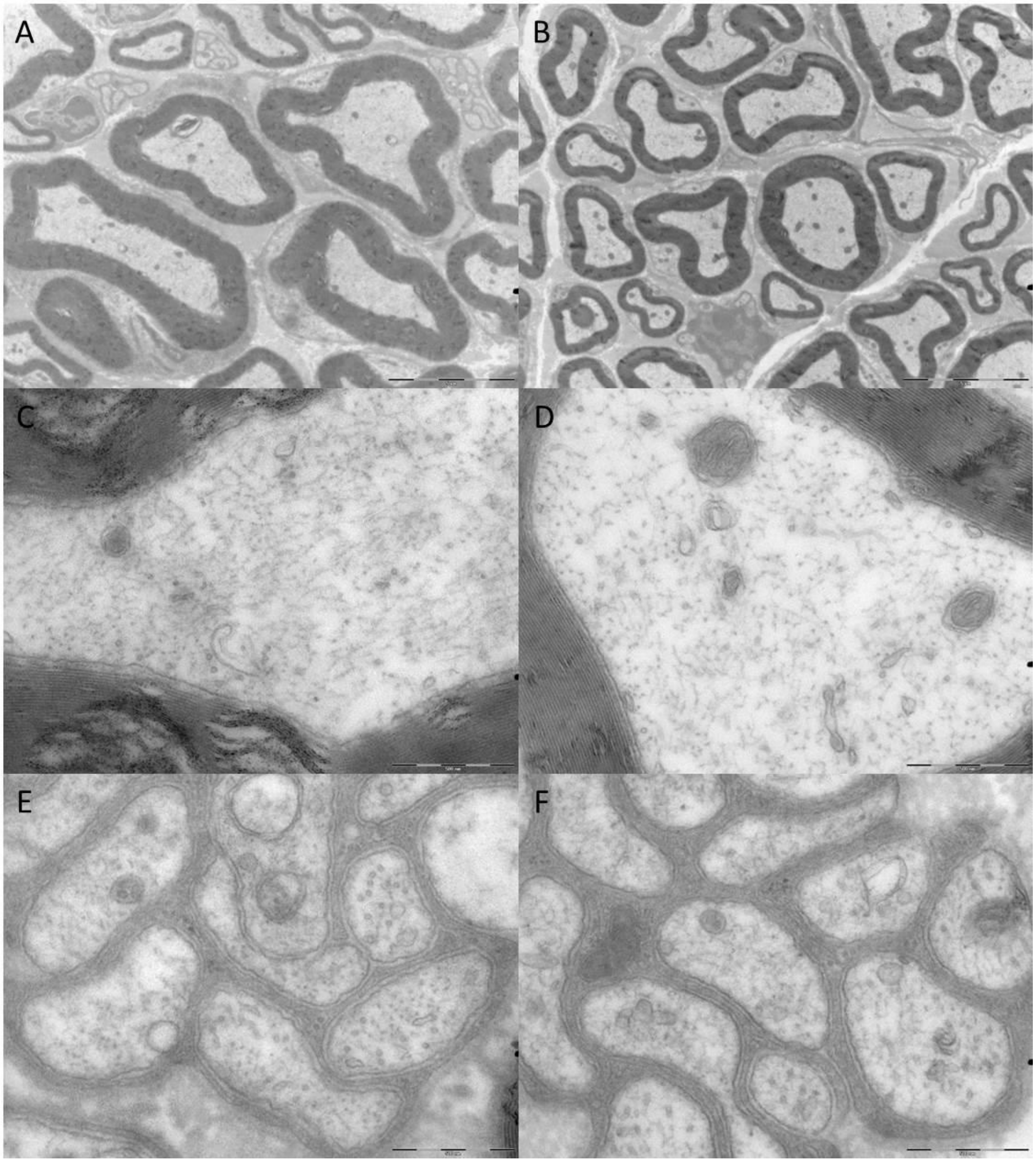

Figure 4.2 – Electron micrographs of sural nerves from wild type and tau knockout mice A) Cross section from wild type mouse. Scale bar = 5 µm B) Cross section from tau knockout mouse. Scale bar = 5 µm C) Myelinated axon from wild type mouse. Scale bar = 500 nm D) Myelinated axon from tau knockout mouse. Scale bar = 500 nm E) Unmyelinated axon bundle from wild type mouse. Scale bar = 500 nm F) Unmyelinated axon bundle from tau knockout mouse. Scale bar = 500 nm No gross differences are noted between wild type and tau knockout mice

However, quantitative examination revealed that microtubules in myelinated axons of tau knockout mice had a significantly larger nearest neighbor distance than those in wild type mice ($p<.001$), suggesting that tau influences the normal clustering of microtubules *in vivo (fig 4.4a*). In unmyelinated axons, microtubules were packed closer together than in myelinated axons (*fig 4.2e,f*), and there were no significant differences in nearest neighbor distance between microtubules wild type and tau knockout mice (*fig 4.4a*).

We next performed analysis on nerves bathed externally in paclitaxel from tau knockout and wild type mice. Two-way ANOVA indicated main effects of genotype and paclitaxel treatment on microtubule nearest neighbor distance in both myelinated ($p<10^{-11}$) and unmyelinated ($p<.001$) axons, and there was a strong trend of an interaction between both factors in myelinated axons ($p = .07$), suggesting microtubule bundling following paclitaxel treatment may occur differentially depending on genotype. Qualitative analysis of electron micrographs revealed that following paclitaxel treatment in wild type mice, tightly clustered microtubule arrays developed throughout the entirety of axons (*fig 4.3a,c,e*). Quantitation of microtubule nearest neighbor distance (*fig 4.4a*) showed a significant decrease in nearest neighbor distances in both myelinated ($p < 10^{-9}$) and unmyelinated axons ($p < .0001$) following paclitaxel treatment. Microtubules located within clusters had a highly consistent spacing of 36.7 $\pm$ 5.9 nm (center to center), which may be indicative of crosslink mediated bundling.

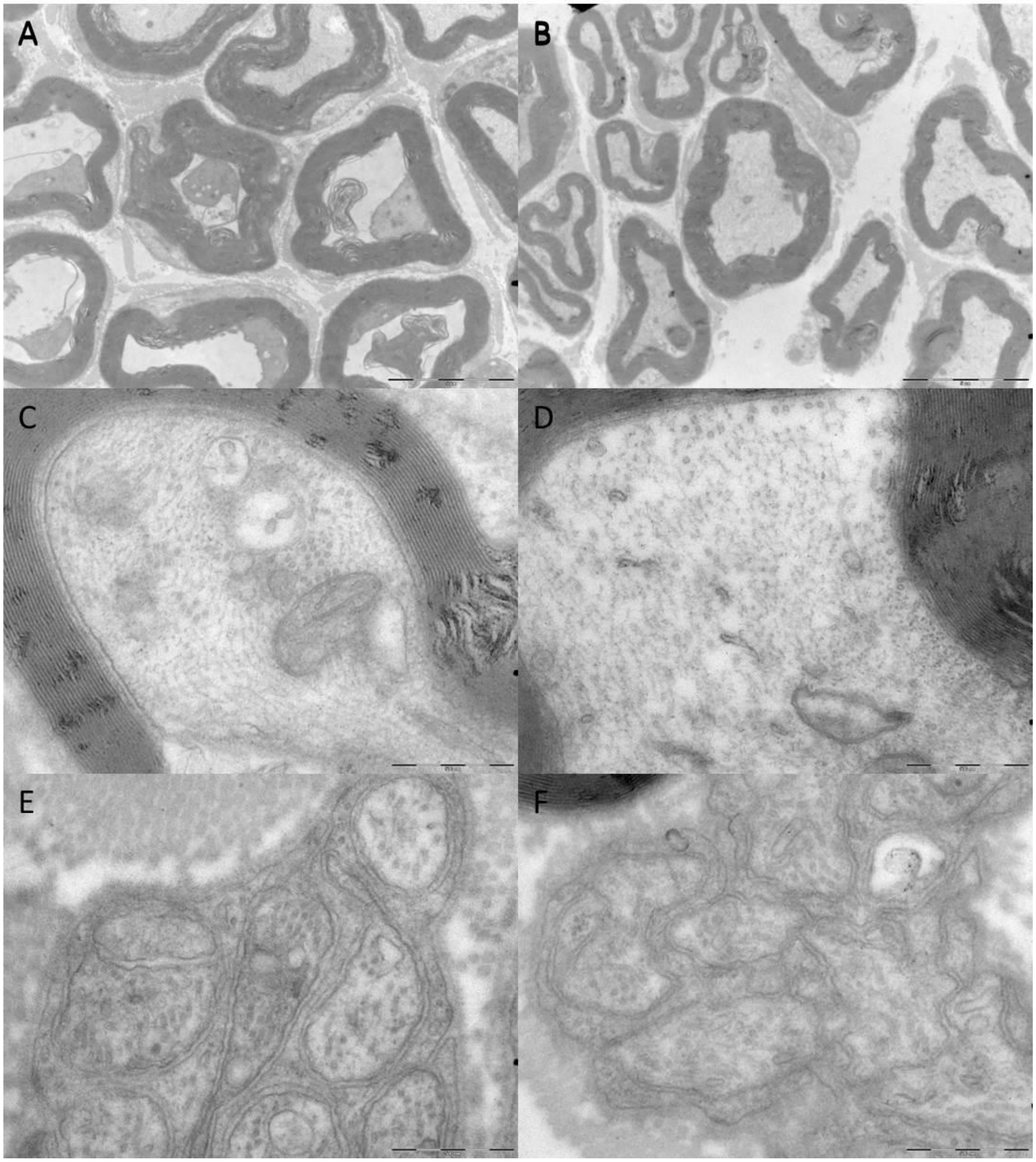

Figure 4.3 – Electron micrographs of sural nerves from wild type and tau knockout mice treated with paclitaxel. A) Cross section from wild type mouse. Paclitaxel treatment leads to severe axonal damage and myelin damage Scale bar = 5 µm B) Cross section from tau knockout mouse. Damage appears less severe than in wild type mice. Scale bar = 5 µm C) Myelinated axon from wild type mouse. Large clusters of microtubules appear throughout the axon. Scale bar = 500 nm D) Myelinated axon from tau knockout mouse. Some clusters of microtubules appear near the periphery of the axon. Scale bar = 500 nm E) Unmyelinated axon bundle from wild type mouse. Axons appear full of microtubule clusters. Scale bar = 500 nm F) Unmyelinated axon bundle from tau knockout mouse. Axons appear full of microtubule clusters. Scale bar = 500 nm

Following paclitaxel treatment, tau knockout mice showed a small decrease in nearest neighbor distance (*fig 4.4a*) in myelinated axons ($p<.05$), though the magnitude of this effect was much smaller than in wild type mice. In addition, microtubules were spaced significantly closer together in paclitaxel treated wild type mice than paclitaxel treated tau knockout mice ($p<10^{-7}$). Unmyelinated axons in tau knockout mice showed a large decrease in nearest neighbor distance ($p<.001$), but these microtubules were also less clustered than those observed in unmyelinated axons from wild type mice ($p<.05$). Regions of clustered microtubules in tau knockout mice localized to the periphery of myelinated axons (*fig 3d*), and clustered microtubules had a larger average spacing than wild type mice (46.1 ± 4.2 nm; $p<.001$; *fig 4.4b*). This suggests that tau, as well as other non-identified structures, may play a role in microtubule bundling following paclitaxel treatment. In addition, electron dense regions of apparent cytoplasmic contraction appeared many axons following paclitaxel treatment (*fig 4.3a,b*). The number of axons observed with this type of deformity was significantly higher in wild type nerves ($p<.0001$), again suggesting that tau may contribute to structural defects following paclitaxel treatment.

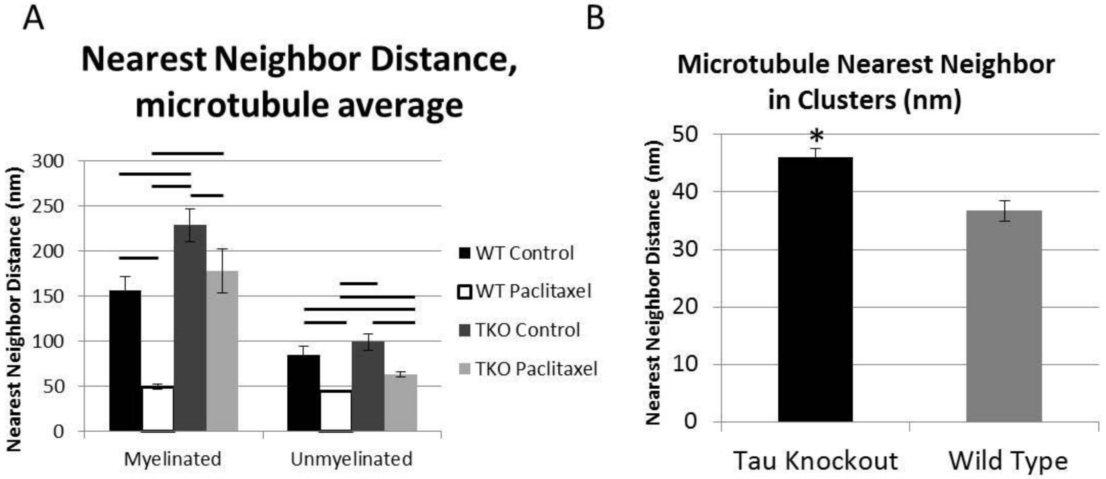

Fig 4.4 – Microtubule nearest neighbor distances
(A) and within microtubule clusters (B). A) Tau knockout mice exhibit larger microtubule nearest neighbor distances than wild type mice prior to paclitaxel treatment in unmyelinated axons and similar microtubule nearest neighbor distances in unmyelinated axons. After paclitaxel treatment, wild type mice exhibit a large decrease in average nearest neighbor distance in myelinated and unmyelinated axons. Tau knockout mice exhibit a small decrease in nearest neighbor distance in myelinated axons, though this is to a much smaller degree than in wild type mice. In unmyelinated axons, tau knockout mice show a similar decrease in nearest neighbor distance as wild type mice; however, microtubules still remain further spaced apart than in wild type mice. Significance ($p<.05$) is noted with bars between different groups. B) Tau knockout mice have further spaced apart microtubules located within paclitaxel induced clusters than wild type mice. * indicates $p < .05$. All error bars indicate standard error of the mean.

In Vitro Bundling Assay

To further quantitatively assess the bundling of microtubules following paclitaxel treatment in a robust manner not dependent on sampling of individual axons or differences in preexisting microtubule configurations, we employed a centrifugation assay (*fig 4.*1) in which larger clusters of microtubules are expected to pellet faster than non-bundled microtubules. We initially used homogenized brain extract, as opposed to peripheral nerve extract, as our model system, due to the insufficient amount of protein acquired from mouse nerves for experimentation and troubleshooting.   Tubulin from brain extracts incubated ± paclitaxel was tracked after centrifugation through a sucrose cushion for varying durations via quantitative western blotting of the supernatant, sucrose, and pellet fractions.

We first performed a control experiment tracking microtubule pelleting in samples of purified tubulin treated ± paclitaxel. Here, both non-paclitaxel treated and paclitaxel treated samples exhibited linear pelleting behavior and approximately the same rate of microtubule pelleting, albeit with an initial increase in the amount of tubulin pelleted at 15 minutes following paclitaxel treatment (*fig 6a*). We next performed similar experiments using homogenized brain extracts. Initially, 7.5 µg protein from each sample, as determined by the Pierce BCA assay, was loaded into each lane of the gel. However, the pellet regions after paclitaxel treatment were highly and selectively enriched in tubulin which led to overloading of the gel and image intensities outside of the linear range of quantification (*fig 4.5a*). Subsequent trials were performed to determine volumes of each sample to load such that all intensities appeared within the linear range, resulting in blots where each lane appeared to have visually similar intensities (*fig 4.5b*) and accurate relative quantification of total tubulin could be easily performed. Following this procedure, 80-90% of the total tubulin of each sample was able to be accounted for in all samples. General trends indicated that over time, tubulin progressively exited the supernatant fractions and either pelleted or remained suspended in the sucrose fractions (*fig 4.5c,d*).

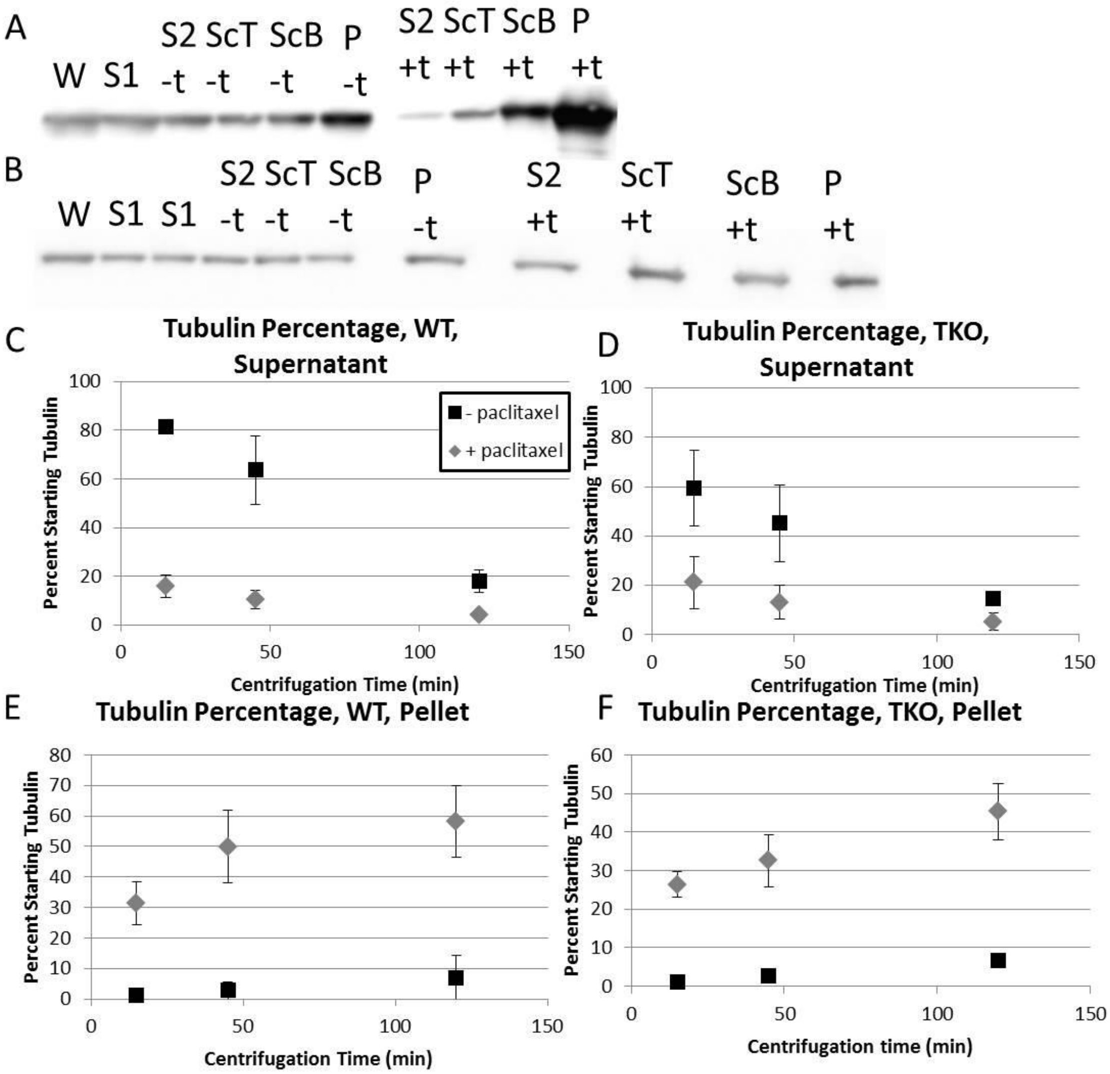

Figure 4.5 – Microtubule pelleting over time
A) Western blot of tubulin from samples centrifuged for 15 minutes, loaded according to total protein content. Tubulin in the +taxol, pellet fraction overloads the gel and is outside the linear range of quantification. W = Whole homogenate, S1 = supernatant 1, S2 = supernatant 2, ScT = sucrose (top half), ScB = sucrose (bottom half), P = pellet; - t = non taxol treated, + t = taxol treated. B) Western blot of tubulin from samples centrifuged for 15 minutes, loaded to equalize intensity across groups. C, D) Tubulin percentage over time within the supernatant 2 fraction from wild type (C) and tau knockout brains (D). Taxol causes a large decrease in the proportion of soluble tubulin, and tubulin leaves the soluble fraction over time. E,F) Tubulin percentage over time within the pellet fraction from wild type (E) and tau knockout brains (F). Taxol treatment causes a large increase in the proportion of tubulin in the pellet fraction, and nonlinear pelleting behavior over time. All error bars indicate standard deviation.

For both wild type and tau knockout brain extract, tubulin that pelleted without paclitaxel treatment occurred at similar, linear rates (*fig 4.5e,f*), and approached similar maximum values for the percent of total tubulin pelleted. Following paclitaxel treatment, both wild type and tau knockout brain extract exhibited a large increase in the initial tubulin pelleted at 15 minutes and a decrease in the amount of tubulin remaining in the supernatant (*fig 4.5,e,f*). In addition, tubulin pelleted in a nonlinear fashion approaching large maximum values of percent total tubulin pelleted relative to both purified tubulin samples and non-paclitaxel treated brain extract samples. Because the presence of paclitaxel did not alter the rate of pelleting in purified tubulin samples, these results indicate that the nonlinear microtubule pelleting behavior following paclitaxel treatment is due to paclitaxel and/or microtubule interaction with other factors in the brain extracts. In addition, comparing the rates of tubulin pelleting following paclitaxel treatment for wild type and tau knockout brain extract indicated that tubulin pelleted at a significantly faster rate in the wild type extract (*fig 4.6b)*. Collectively, because paclitaxel treated microtubules in wild type brain extract pelleted at a significantly higher rate than those in the tau knockout brain extract, and pelleting rate has been previously linked to microtubule crosslinking, it is likely that tau plays a role in microtubule bundling following paclitaxel treatment. In addition, because the tau knockout brain extract still showed elevated rates of pelleting following paclitaxel treatment, microtubule bundling must also occur through non-tau mediated interactions.

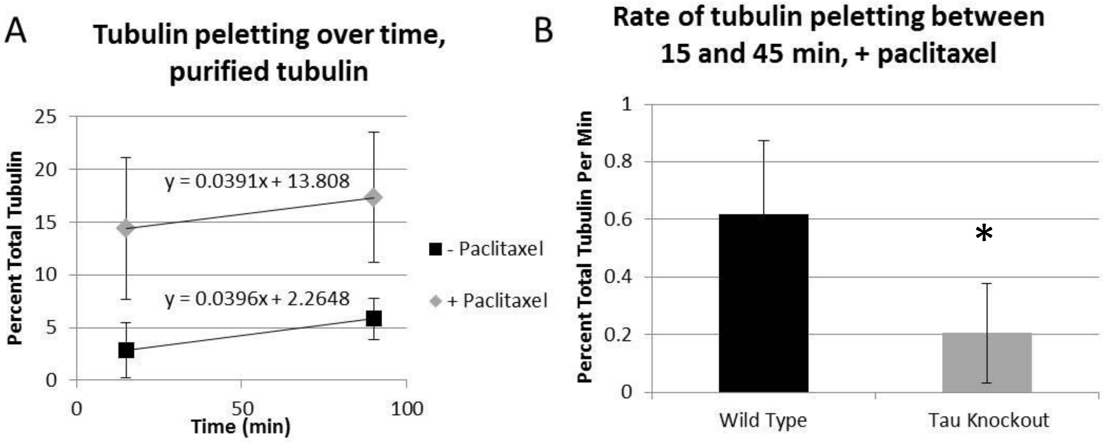

Figure 4.6 – Microtubule pelleting rates.
A) Paclitaxel treatment causes an increase in the tubulin initially pelleted in the first 15 minutes; however, purified tubulin pellets at the same rate over time regardless of paclitaxel treatment (regression lines). B) Wild type brain extract tubulin pellets significantly faster than tau knockout brain extract tubulin when treated with paclitaxel. All error bars indicate standard deviation. * indicates $p < .05$.

Functional Testing

Mice typically exhibit signs of mechanical allodynia and thermal hyperalgesia following paclitaxel treatment, as indicated by von frey hair and tail withdrawal testing, respectively. Because our results implicated a role for tau in exacerbating microtubule bundling, we next sought to determine whether mice lacking of tau would be resistant to typical neuropathic progression. We therefore performed sensory testing on wild type and tau knockout mice treated with paclitaxel.

Following paclitaxel treatment, wild type mice showed signs of mechanical sensitivity demonstrated by a significant decrease in the 50% response threshold that progressed with increasing dosages (*fig 4.7*). Tau knockout mice showed slightly reduced baseline response threshold values prior to paclitaxel treatment, indicating that mice lacking tau may potentially be more sensitive to mechanical stimuli. The reason for this is not yet known. Following paclitaxel treatment, tau knockout mice also showed a significant increase in mechanical sensitivity (*fig 4.7*). Thus, even though morphological and biochemical analysis indicated that tau increases the extent of structural changes following paclitaxel treatment, removal of tau is not sufficient to prevent functional neuropathy.

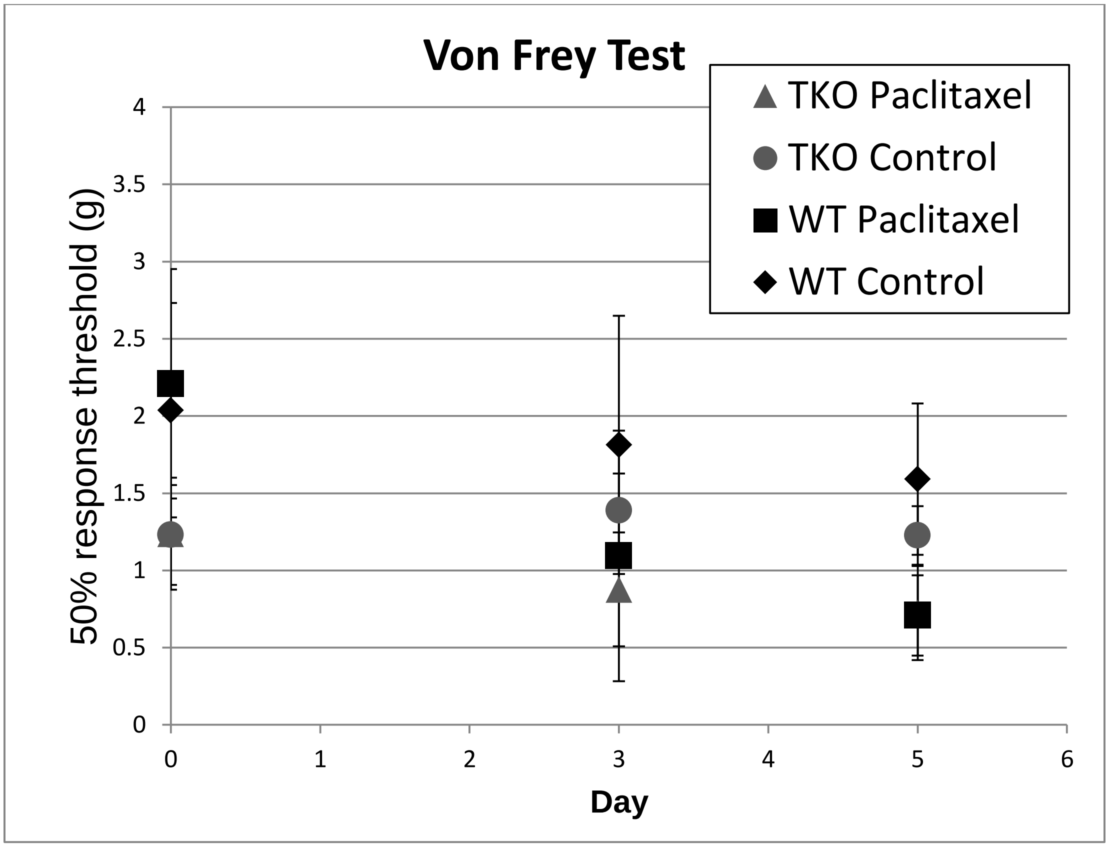

Figure 4.7 – Sensory testing.
Mechanical sensitivity in wild type and tau knockout mice were assessed prior to paclitaxel treatment (day 0), after 2 days of treatment (day 3), and after 4 days of treatment (day 5) using the Von Frey hair test. Tau knockout mice showed reduce response thresholds at day 0 prior to treatment. Wild type and tau knockout mice both exhibit increased mechanical sensitivity following paclitaxel treatment. These results indicate that removal of tau is not sufficient to prevent the development of neuropathy. All error bars indicate standard deviation.

4.5 Discussion

Overall, results suggest a role of tau in the formation of paclitaxel induced microtubule bundles. Electron microscopy of nerves bathed in paclitaxel showed significantly less microtubule bundle formation following paclitaxel treatment in nerves from tau knockout mice compared to wild type mice. Similarly, homogenized brain extract from wild type mice pelleted faster than extract from tau knockout mice following paclitaxel treatment, again implicating tau in the formation of microtubule bundles. However, in both experiments, removal of tau was not sufficient to completely prevent bundle formation. This suggests that other proteins are also involved in microtubule bundling following paclitaxel treatment. Finally, sensory testing of mice injected with paclitaxel revealed that tau knockout mice were still susceptible to neuropathy, indicating that removal of tau is not sufficient to prevent functional neuropathy.

Effects of paclitaxel on sensory nerve structure

Several previous studies have observed qualitative increases in microtubule clustering along with other structural abnormalities via electron microscopy peripheral nerves following paclitaxel treatment[67,68,139]. Axonal transport disruption due to disruptions to the microtubule network in axons is hypothesized to play a role in neuropathic progression following paclitaxel treatment[52,77,99], and thus the exact cause of the formation of aberrant microtubule clusters may be important to designing therapies to ameliorate or prevent paclitaxel induced neuropathy. In agreement with previous studies, paclitaxel treatment led to a large increase in microtubule bundling in wild type mice as quantitatively demonstrated by analysis of electron micrographs[68]. Importantly, while previous studies typically analyzed sciatic nerves containing both motor and sensory branches, our study directly analyzed a pure sensory nerve due to the selective sensory neuropathy induced by paclitaxel treatment, and showed structural abnormalities in a large percentage of observed axons. We have additionally demonstrated that microtubules pack in a highly organized and consistent fashion, which is likely indicative of controlled cross-linking or trafficking of these microtubules.

Prior experimentation has revealed that tau alone can cross-link microtubules[85], that paclitaxel and tau may interact and compete at the same binding site[81], and that paclitaxel stabilized microtubules can be cross-linked by tau[85]. In mice lacking tau, initial microtubule bundling and microtubule bundling following paclitaxel treatment was decreased compared to wild type mice in myelinated axons, indicating that tau plays a detectable role in microtubule cross-linking *in vivo*. However, there were no differences observed in microtubule nearest neighbor distances between unmyelinated axons from wild type and tau knockout mice without paclitaxel treatment, and microtubule cross-linking still increased in tau knockout mice following paclitaxel treatment, suggesting that other microtubule associated proteins unrelated to tau are additionally involved in microtubule clustering and organization. Intriguingly, the spacing between microtubules within clusters that formed following paclitaxel treatment was different between tau knockout and wild type mice. This additionally provides further evidence that multiple types of microtubule associated proteins are likely involved in bundle formation. Finally, it is important to note that the spacing observed between bundled microtubules in wild type mice is not entirely consistent with literature reported values expected for tau crosslink. Tau crosslinks have been reported to be 20-27 nm in length[140], whereas in our study, microtubules in clusters had center to center distances of 36.7 ± 5.9 nm. Given that microtubules are ~25 nm in diameter, the crosslink length in this case would be 11.6 ± 5.9 nm, which is smaller than one would expect for tau crosslinks. This further suggests that other MAPs may also influence paclitaxel induced bundling, and additionally raises the possibility that the reduction in bundling observed in tau knockout mice may have been an indirect effect due compensatory changes or alterations to the initial microtubule cytoskeleton prior to paclitaxel treatment.

Effects of paclitaxel on microtubule bundling in brain extracts

The centrifugation assay used in this study was modified from a previously published protocol which also described evidence of microtubule bundling following paclitaxel treatment in brains of wild type mice[31]. One important distinction between our methods is that we selectively quantified tubulin pelleting, whereas the previous study quantified total protein in the pellet. Our study indicated that while total protein pelleting, as measured by BCA assays, generally followed the same trend as pure microtubule pelleting (*fig 4.8*), paclitaxel treatment greatly selectively enhanced pelleting of microtubules compared to other proteins. This indicates that paclitaxel treatment enhances clustering of microtubules to each other at faster rates than other cytoskeletal materials.

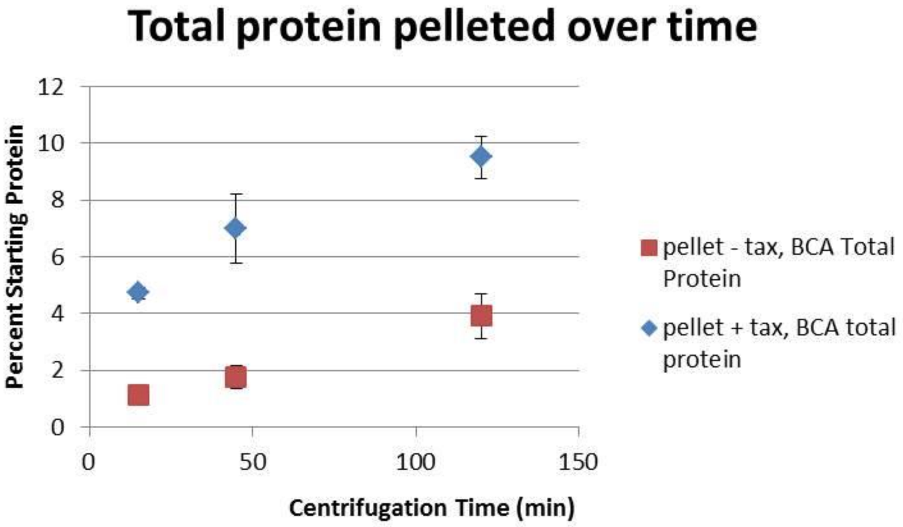

Figure 4.8 – Total protein pelleted over time in wild type mice.
Paclitaxel treatment increases the total protein pelleted over time; however, the percent total protein pelleted is much lower than the percent tubulin pelleted (*fig 4.5*), indicating selective enhancement of microtubule polymerization and bundling. Error bars indicate standard deviation.

The results from the centrifugation assay largely confirmed observations made by electron microscopy. Paclitaxel treatment increased microtubule bundling in both wild type and tau knockout mice, however, this increase was reduced in tau knockout mice. Thus, again, evidence implicates a role for tau, along with other, undetermined proteins, in the development of microtubule bundling following paclitaxel treatment. However, conclusively extrapolating results from the analysis of brains to the peripheral nervous system is not possible, as brains contain dendritic elements, different tau isoforms, and many other cell types than those found in peripheral nerves.

Functional Results and Conclusions

Interestingly, despite the reduction in microtubule bundling in tau knockout mice, functionally, tau knockout mice did not appear to show resistance to paclitaxel treatment. There are several possible reasons for this result. One possibility is that even without tau, microtubule abnormalities following paclitaxel treatment are still sufficiently severe to cause neuropathic symptoms. Alternatively, while smaller myelinated and unmyelinated axons are responsible for mechanical and thermal pain transmission, tau knockout mice seemed most resistant to bundling in larger myelinated fibers. Thus, it is possible that fibers responsible for pain transmission were less affected by the removal of tau. Finally, it is possible that structural clustering of microtubules may not be the primary cause of neuropathy. For example, studies indicate several other potential sites of neuropathy initiation, such as upregulation of TRPV channels linked to pain transmission[75], mitochondrial dysfunction[52,73], and signs of inflammation[74]. However, while many observations of dysfunction have been reported, no initial site of neuropathy has yet been determined. If future work can determine the cause of structural deficits following paclitaxel treatment and reduce their occurrence, then it may be possible to determine whether the cause of paclitaxel induced neuropathy is structural in origin. Such analysis can then further guide the targeted development of treatments for paclitaxel induced neuropathy.

4.5 Acknowledgements

I would like to acknowledge two other contributors to this project, Sameer Shah and Elisabeth Orozco, who will be included as co-authors in the event that the work in this chapter is submitted for publication in the future.

CHAPTER 5: ACTIN–MYOSIN NETWORK INFLUENCES MORPHOLOGICALR RESPONSE OF NEURONAL CELLS TO ALTERED OSMOLARITY

5.1 Summary

Acute osmotic fluctuations in the brain occur during a number of clinical conditions and can result in a variety of adverse neurological symptoms. Osmotic perturbation can cause changes in the volumes of intra- and extracellular fluid and, due to the rigidity of the skull, can alter intracranial pressure thus making it difficult to analyze purely osmotic effects in vivo. The present study aims to determine the effects of changes in osmolarity on SH-SY5Y human neuroblastoma cells in vitro, and the role of the actin–myosin network in regulating this response. Cells were exposed to hyper- or hypoosmotic media and morphological and cytoskeletal responses were recorded. Hyperosmotic shock resulted in a drop in cell body volume and planar area, a persisting shape deformation, and increases in cellular translocation. Hypoosmotic shock did not significantly alter planar area, but caused a transient increase in cell body volume and an increase in cellular translocation via the development of small protrusions rich in actin. Disruption of the actin–myosin network with latrunculin and blebbistatin resulted in changes to volume and shape regulation, and a decrease in cellular translocation. In both osmotic perturbations, no apparent disruptions to cytoskeletal integrity were observed by light microscopy. Overall, because osmotically induced changes persisted even after volume regulation occurred, it is possible that osmotic stress may play a larger role in neurological dysfunction than currently believed.

5.2 Introduction

Changes in intracranial pressure are dictated by alterations in extracellular fluid volumes, and are largely determined by the balance between hydrostatic and osmotic pressures. Clinically, traumatic brain injury and glaucoma have been correlated with high intracranial and intraocular pressure, respectively[155]. Brain osmolarity may also fluctuate during the progression of a number of conditions, such as traumatic brain injury, infection, ischemia, diabetic hyperglycemia, and dehydration. Osmotic fluctuations are associated with a wide variety of neurological symptoms including seizures, coma, and death[156]. Conversely, controlled osmotic therapy has potential benefits in the short-term management of brain edema, which leads to elevated intracranial pressure[157]. Despite the importance of understanding osmotic effects on neuronal function, purely osmotic effects on neurons are difficult to decouple from hydrostatic pressure related effects in vivo because osmotic perturbations affect tissue swelling and extracellular fluid levels, and thus also intracranial pressure.

The lipid bilayer of the cell membrane is typically more permeable to water than the various ions present in the intra and extracellular fluid by several orders of magnitude[158]. Consequently, osmotic alterations cause an initial fluid flux into or out of the cell. As maintenance of cell volume and osmolyte concentration are critical for proper cellular function and survival, cells are equipped to restore homeostatic volume levels after osmotic perturbation by undergoing a regulatory volume increase or decrease[158]. Volume influx or efflux can activate stretch related signaling pathways, mechano-sensitive ion channels, alter the concentrations of intracellular ions and molecules, and regulate intracellular membrane recruitment to the plasma membrane[159-161]. By thus modulating osmolyte concentration, the cell is able to adjust its volume, thereby adapting to the osmotic fluctuations encountered due to physiological conditions.

The unique polarity and geometry of neurons, which are composed of a soma and elongated neurites, imposes an additional constraint upon volume regulation. Fernandez and Pullarkat showed that the volume of PC12 neurites returns to baseline values in just several minutes in response to hypoosmotic shock[162]. On the other hand, in cases of fast onset acute osmotic shock, natural regulatory mechanisms can fail, leading to severe pathology[156]. A likely candidate for guiding neuronal response to osmotic loading is its cytoskeleton, which is responsible for bearing mechanical loads and maintaining cell morphology. Several studies directly implicate a cytoskeletal role in the cell volume regulatory response. For example, the capabilities of various cell lines to regulate volume increases and decreases are perturbed via actin disruption[163,164]. In addition, erythrocytes behave as a perfect osmometer only after disruption of the spectrin–actin cytoskeleton[165], implying that the cytoskeleton normally resists osmotic changes. Finally, both microtubule and myosin disruption alter the rate and magnitude of hypoosmotically induced swelling, though not recovery, in PC12 neurites[162].

Despite the known roles of the cytoskeleton in the cellular response to osmotic loading, the full scope of the effects of osmotic perturbation on neuronal cells, including a role for the neuronal cytoskeleton, has not yet been determined.

Toward the elucidation of such pathways the present study analyzed the role of the actin–myosin cytoskeleton in the short-term morphological response and cellular movement changes in SH-SY5Y human neuroblastoma cells in response to hyper- and hypoosmotic shock.

5.3 Results

Qualitative Response to Osmotic Loading

Following retinoic acid treatment in order to induce differentiation, consistent with their neuronal identity, SY5Y cells extended projections of lengths up to 10 times the diameter of their cell bodies. Cells existed in an interconnected network, with each cell analyzed connected to between 1 and 4 cells. Cells not connected to any other cells did not extend long projections, and were not analyzed.

We first assessed cell viability in media of a wide range of osmolarities in order to choose osmotic perturbations for subsequent analyses that significantly perturbed the cell population while still avoiding acute toxicity. Cells exposed to media with osmolarities of 190 mOsm (C = 0.6 relative to control media) or 420 mOsm (C = 1.3 relative to control media) both experienced significant toxicity (<50% viability) at 24 h, indicating that osmotic shock of this magnitude was a potentially lethal perturbation (Table 5.1).

Table 5.1 – Cell viability following osmotic perturbation
SH-SY5Y cells were exposed to media of a wide range of osmolarities. After 24 h, a live/dead assay was performed to quantify the percentage of living and dead cells. Osmolarity of standard culture media for SH-SY5Y cells was measured to be 320 mOsm. Significant change compared to control (Tukey's HSD, α=.05).

Osmolarity (mOsm)	**Viability Percentage**
140	6.0 ± 3.6 *
190	24.7 ± 3.5 *
250	75.3 ± 9.3 *
320	87.3 ± 3.6
420	45.3 ± 8.2 *
530	19.3 ± 4.2 *
630	22.3 ± 4.9 *
730	14.0 ± 3.5 *

However, at earlier time points, cells exposed to C = 0.6 and C = 1.3 media still seemed viable and remained adherent, allowing us to analyze cellular responses post-treatment. To further investigate the short-term response to osmotic loading SH-SY5Y cells were imaged for 30 min after exposure to hyper- or hypoosmotic media. Gross morphological changes were first noted qualitatively. Typically, control cells (320 mOsm) maintained constant shape (*fig 5.1*a), while hyperosmotic media (420 mOsm, C = 1.3) caused the cells to assume a more elliptical shape (*fig 5.1*b). Hypoosmotic media (190 mOsm, C = 0.6) did not result in consistently large morphological changes at early time points; however, at later time points, cells trended toward a more rounded morphology (*fig 5.1c*), though occasionally experienced large shape deformations in which the natural regular elliptical or round shape of the cell was altered (*fig 5.6c*). Interestingly, nuclei (apparent as faint shadows in the cell body) also seemed to respond to changes in osmolarity, though apparently independent of the cell bodies. Though these qualitative responses applied to most cells within a group, differences in cellular response between groups were not always visually obvious. In order to gain a better sense of the exact morphological changes occurring to the cells, we quantitatively assessed cellular geometry.

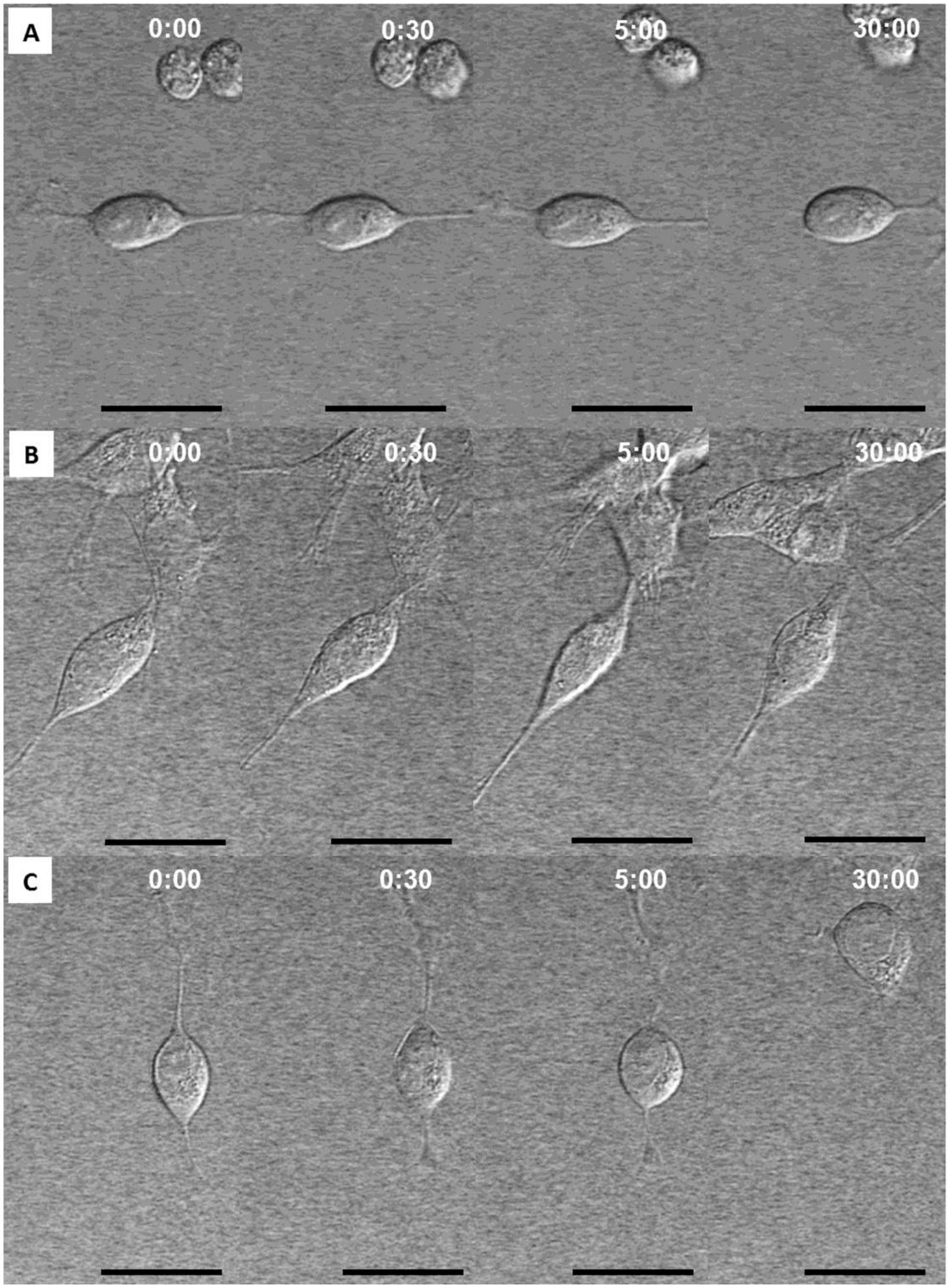

Figure 5.1 – Time lapse images of differentiated SH-SY5Y cells exposed to osmotic stresses (a) Control cells exposed to standard culture media. Morphology stayed relatively constant. (b) Cells exposed to C=1.3 media. Shape became more elliptical and cellular motion was observed. (c) Cells exposed to C=0.6 media. Cell shape stayed relatively constant at early time points but the cell began to round and crawl to a new location. Scale bars=20 mm.

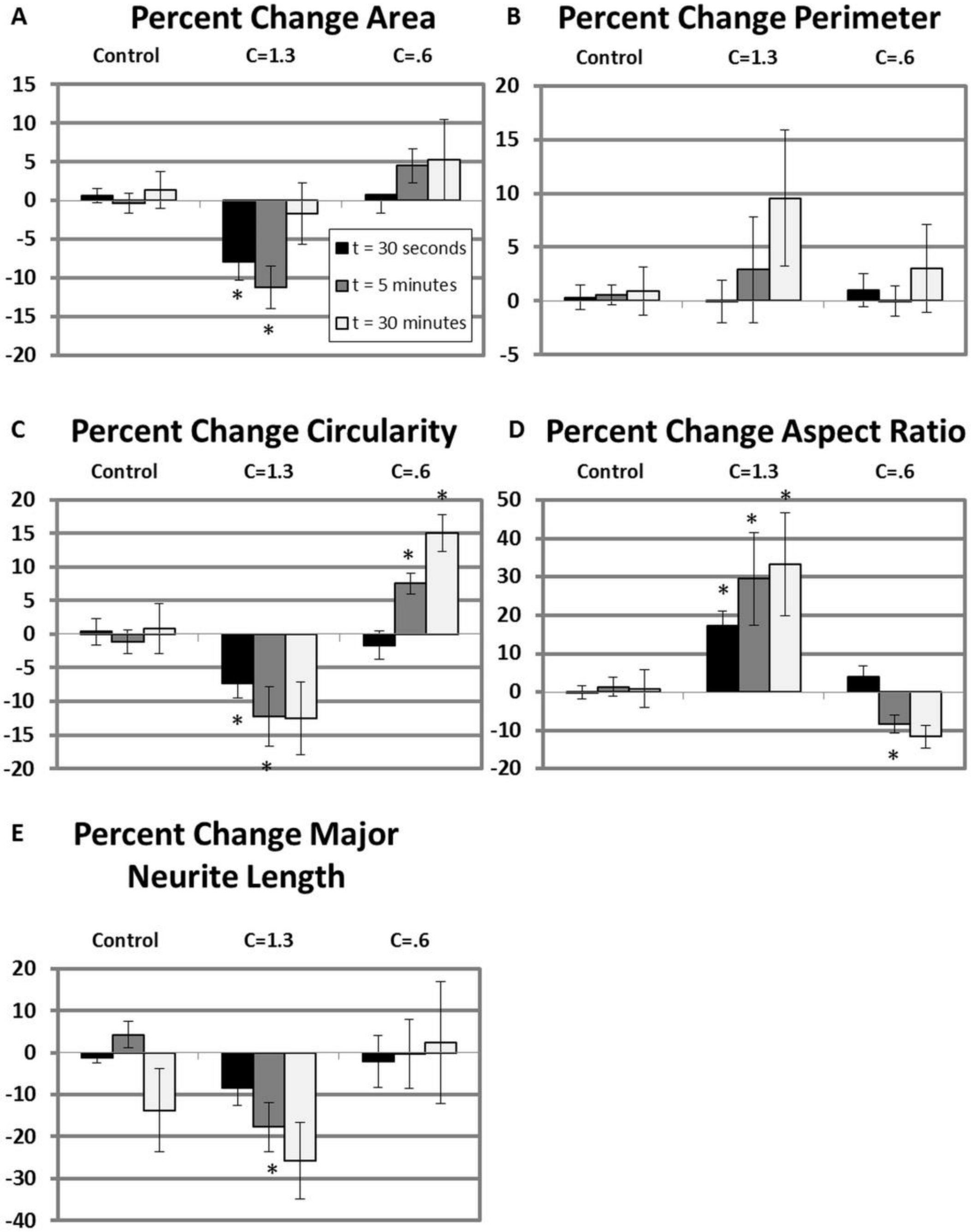

Figure 5.2 – Changes in cell geometry parameters
Parameters of cells were measured at 30 s, 5 min, and 30 min, and compared to starting values. * represents a significant change (Tukey's HSD, α = 0.05) compared to control at that time point. Error bars represent standard error of the mean. N=12–16 for each group. (a) Percentage of change area, (b) percentage change in perimeter, (c) percentage change in circularity, (d) percentage change in aspect ratio, and (e) percentage change in axon length.

Changes in Neuronal Geometry Following Osmotic Loading

We first measured the percentage change in cell body area from baseline (*fig 5.2a*). Two-way ANOVA revealed a significant effect of osmolarity on cell body area ($P < 0.05$), but no effect of time and no significant interaction between time and osmolority. Post-hoc comparisons showed that initially, as expected, the planar area (from 2-D images) of cell bodies exposed to hyperosmotic media ($C = 1.3$) significantly decreased by an average of 7.9 ± 9.4% at 30 s ($P < 0.05$). This area decrease peaked at 11.2 ± 11.1% at 5 min, and then gradually diminished over time. After 30 min in hyperosmotic media, cell body area was no longer significantly different from control values. Interestingly, cell body area was less sensitive to hypoosmotic stress; no significant differences were observed at any time point, although there was a trend toward increased area over time.

In order to determine how planar area changes correlated with the overall volume change in the cell body, volumes of cells exposed to hyper- and hypoosmotic media were approximated by staining the cell membrane with a fluorescent wheat germ agglutinin dye[166,167] (*fig 5.3*); cell areas at varying slice depths were used to reconstruct cell volumes. Two-way ANOVA indicated a significant effect of osmotic treatment on volume ($P < 0.05$) and a significant interaction term ($P < 0.05$) between osmotic and time effects. Post-hoc analysis showed that initially, hyperosmotic treatment caused a significant decrease in cell body volume that peaked at 5 min with an average volume reduction of 29.9 ± 6.4% ($P < 0.05$). This volume decrease still persisted at 30 min with minimal changes. In the case of cells exposed to hypoosmotic media, minimal volume changes were detected in the first 30 s; however, by 5 min, cell volume significantly increased by an average of 31.9 ± 0.7% ($P < 0.05$). Interestingly, by 30 min, volume measurements approached initial values, indicating that volume regulation within the cell had occurred. Finally, in order to assess the relationship between volume and area changes, linear regression analysis between average change in volume and area at each time point was performed (*fig 5.3b*). Results showed that while volume changes were higher in magnitude than area changes, area and volume changes were tightly coupled, with an $R^2 = 0.7239$. Thus, area response was a reasonable proxy for volume response.

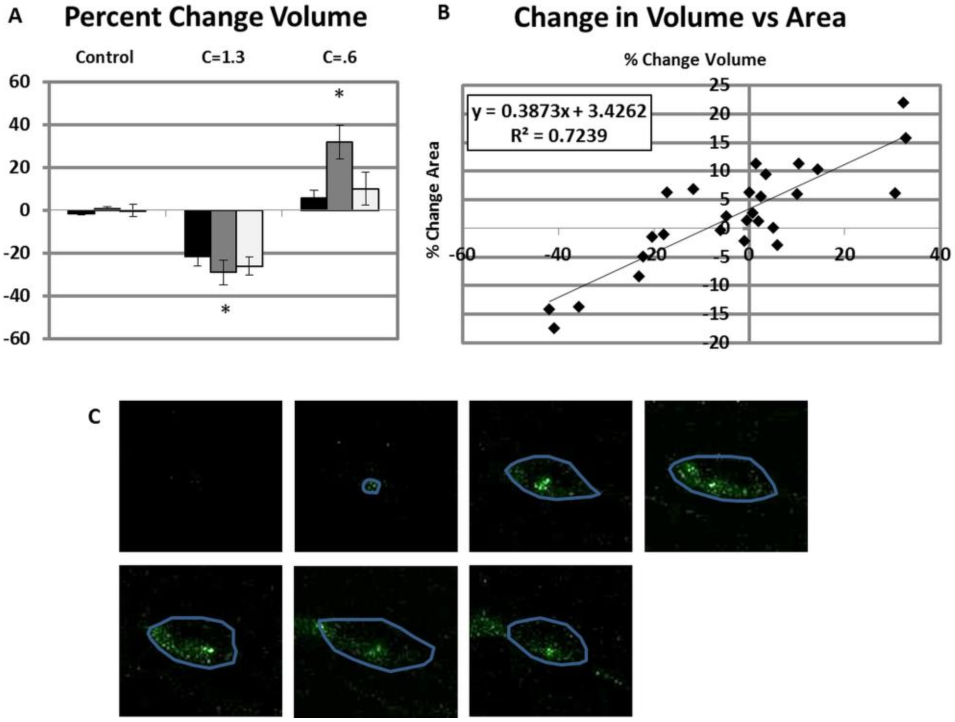

Figure 5.3 – Percentage change in volume vs. percentage change in area
(a) percentage change in cell body volume. * represents a significant change (Tukey's HSD, $\alpha = 0.05$) compared to control at that time point. N = 3 per group. Error bars represent standard error of the mean. (b) Scatterplot of volume and area changes taken for each treatment group with linear regression line of best fit. Note that volume and area changes are positively correlated, with volume changes being higher in magnitude. (c) Fluorescent wheat germ agglutinin showing outline of a cell at various depth slices in order to estimate volume.

In contrast to area, cell body perimeter did not significantly change for all groups; the trend toward increasing perimeter for the hyperosmotic group was largely driven by a few cells with large perimeter increases (*fig 5.2b*). Two-way ANOVA revealed no significant effects of osmolarity or time of exposure. Closer analysis of the data for individual cells showed that area and perimeter changes did not always occur at the same rates or same directions, suggesting that changes in cell shape must have occurred. We therefore quantified cell body shape changes in response to osmotic loading using two independent parameters, circularity and aspect ratio (*fig 5.2c and 5.2d*). Two-way ANOVA revealed an effect of osmotic treatment ($P < 0.05$) on circularity and aspect ratio, as well as a significant interaction effect between time and osmotic treatment on circularity ($P < 0.05$). The majority of cell bodies examined naturally assumed a circular or elliptical appearance under normal conditions. Control values stayed constant, showing stable circularity in a resting neuron. Hyperosmotic shock resulted in a significant decrease in circularity compared to control values apparent at 30 s post-treatment ($P < 0.05$). Circularity progressively decreased over time, culminating with an average decrease of 12.5 ± 21.6% at 30 min. Consistent with this observation, aspect ratio changes indicated a significantly more elliptical shape over time, with a peak average increase of 33.3 ± 53.5% at 30 min. Conversely, hypoosmotic shock caused a slower but persistent increase in circularity and decrease in the aspect ratio of the cells. At 30 s post-treatment there were minimal changes in either shape descriptor. By 5 min, cells showed a significant increase in circularity and decrease in aspect ratio ($P < 0.05$), and the magnitudes of these changes increased and persisted at 30 min with an average circularity increase of 15.0 ± 11.0% and average aspect ratio decrease of 11.7 ± 12.0%.

Osmotic shock was also hypothesized to affect neurites, which are continuous with the neuronal cell body, and whose length is dependent on cell tension and substrate adhesion[168]. To test whether neurites extended or retracted in response to osmotic stress, the length of the longest neurite projection was measured over time in response to osmotic perturbation (*fig 5.2e*). Two-way ANOVA revealed significant effects of osmotic treatment and time on neurite length ($P < 0.05$). In response to hyperosmotic shock, neurites tended to retract over time. This decrease in length was significant at 5 min ($P < 0.05$), and peaked at 30 min with an average decrease of 25.8 ± 36.6. However, control cells also showed a slight, but variable decrease in neurite length at 30 min, indicating that the 30-min imaging process may have slightly perturbed the cells. In response to hypoosmotic shock, neurite length did not significantly change compared to control values at any time point; however, this measurement was highly variable between cells. Occasional instances of neurite “retraction” resulted from cell body movement along the path of the neurite, suggesting a dependence of this parameter on cell motility.

In order to better determine how the chosen parameters related to each other and potentially unmask trends buried within the high variability of the averaged data, we performed multiple linear regression analysis. In particular, we were interested in whether shape change could be predicted by a given change in area, perimeter, and neurite length. Change in aspect ratio was regressed against three potential geometric influences: change in area, change in perimeter, and change in neurite length (Table 5.2). R^2 values ranged from 0.58 to 0.78 for each condition and P values were well within the significant range for each fit ($P < 0.001$). Results revealed that change in perimeter is the strongest predictor of change in aspect ratio, as it showed a strong positive correlation in every group analyzed. Area showed a negative correlation in all groups, and neurite length seemed unrelated to changes in the cell body size and shape.

Table 5.2 – Multiple linear regression analysis coefficients showing parameters influencing aspect ratio

Group	**Area**	**Perimeter**	**Axon Length**	**Intercept**	**R^2**	**P-value**
Control	-0.28165	1.999014	-0.02562	-0.39305	0.736576	8.36E-13
C=1.4	-1.92698	2.970918	-0.06664	0.013597	0.775511	2.54E-14
C=.6	-0.91161	1.975195	0.045445	0.659902	0.586257	1.22E-04

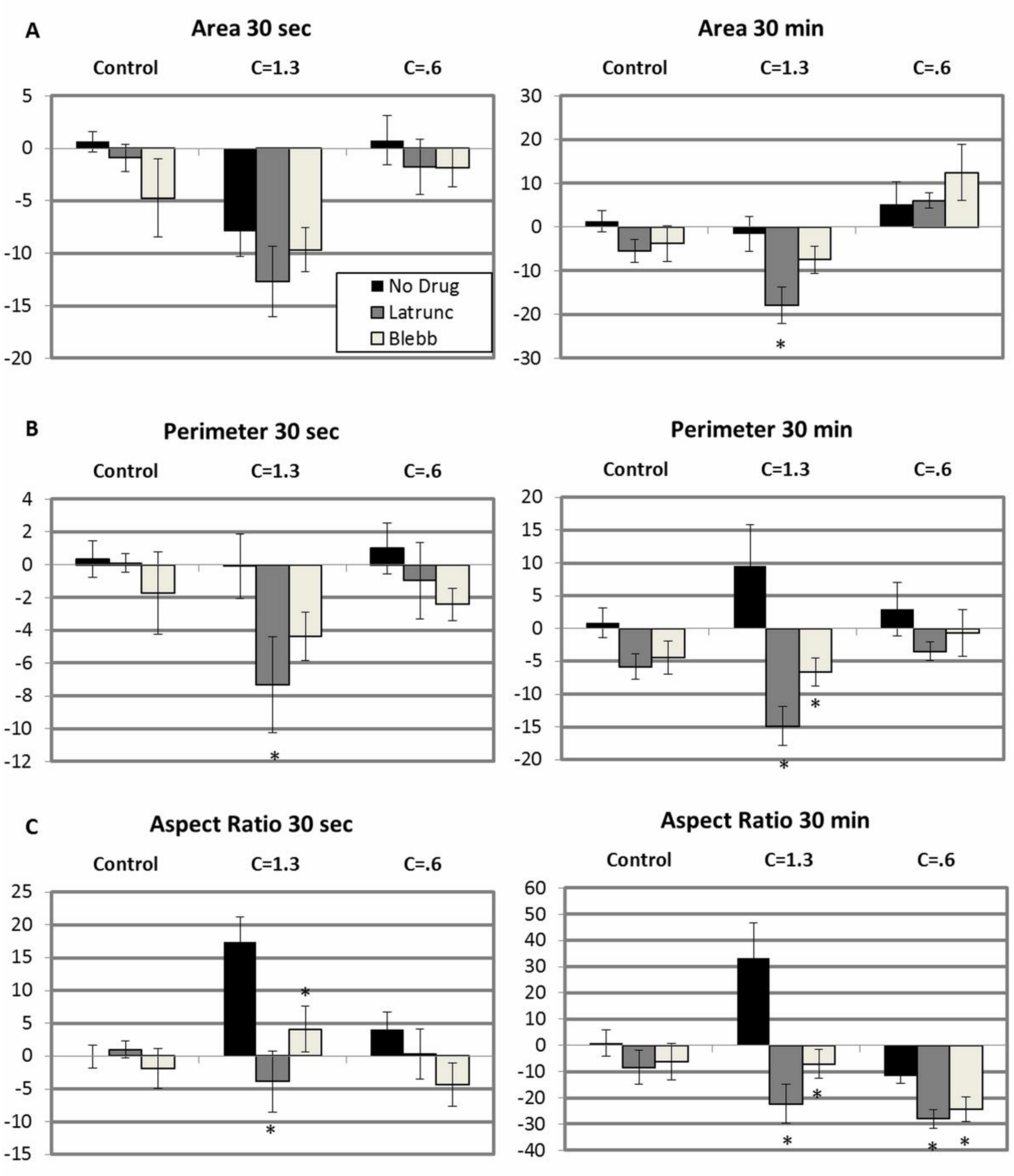

Figure 5.4 – Morphological changes following actin or myosin disruption.
Cells were treated with latrunculin b (10 mm) or blebbistatin (20 mm), treated with hyper- or hypoosmoticmedia, and imaged as above. (a) Percentage of change area at 30 s and 30 min. (b) Percentage of change perimeter at 30 s and 30 min. (c) Percentage of change aspect ratio at 30 s and 30 min. Error bars represent standard error of the mean. N=9 per drug-treated group. Nondrug-treated groups are the same as in fig 5.2 and presented here for ease of comparison. * indicated P<0.05 (Student’s t-test) compared to the nondrug-treated group of the same test conditions.

Influences of actin and myosin on osmotically induced geometric changes

In order to determine potential mechanisms involved in guiding the observed morphological changes, we perturbed the actin cytoskeleton and associated myosin motors due to their known roles in cell contractility, migration[169], and volume regulation[164]. Cells were treated with latrunculin B (inhibitor of f-actin assembly) or blebbistatin (inhibitor of myosin II activity), and cells were imaged as above. We performed additional control experiments to verify that working concentrations of DMSO, used to solubilize inhibitors, did not alter cellular morphology. In agreement with several studies that have used drugs in a similar context[162,170], our data revealed that DMSO treatment did not result in any perturbations beyond the normal fluctuations observed in untreated controls by any morphological measure used in this study. Thus, to avoid the complexity of comparisons with two separate control groups, we compared latrunculin- and blebbistatin-treated cells to the untreated control groups discussed previously.

In the absence of osmotic perturbation, drug treatment did not significantly alter cell size or shape compared to control values. However, differences in cell size and shape regulation became apparent upon treatment with hyper- and hypo-osmotic media (*fig 5.4*). In response to hyperosmotic media, all groups (latrunculin, blebbistatin, and no drug) initially experienced area decreases, but these area decreases brought about drastically different shape changes. Both latrunculin- and blebbistatin-treated cells experienced a significantly decreased percentage of change in aspect ratio compared to control cells at the 30-s time point ($P < 0.05$; *fig 5.4*c). This change persisted at the 30-min time point, where latrunculin- and blebbistatin-treated cells trended toward a decrease in aspect ratio, in contrast to the more elliptical morphology of control cells. Thus, while untreated cells shrank in a polarized fashion, both actin and myosin disruption resulted in symmetrical area reduction to a more circular shape, suggesting a role of the actin–myosin network in shape regulation and adhesion following hyperosmotic shock. While nondrug-treated cells largely recovered their areas in response to hyperosmotic media by 30 min, latrunculin, but not blebbistatin-treated cells showed a significantly reduced area and perimeter that persisted through all time points ($P < 0.05$; *figs 5.4a and 5.4b*). This suggests a role of an intact actin cytoskeleton, partially independent of myosin motors, in the regulatory volume increase.

Drug treatment also altered the cellular response to hypo-osmotic shock. All groups showed a trend toward a reduction in aspect ratio following treatment. However, at 30 min, latrunculin, and particularly blebbistatin-treated cells remained significantly rounder compared to nondrug-treated cells ($P < 0.05$; *fig 5.4*c). In addition, blebbistatin-treated cells trended toward an increased area at 30 min compared to baseline values when exposed to hypoosmotic media while nondrug-treated cells did not ($P = 0.10$; *fig 5.4a*). Axons did not retract following latrunculin or blebbistatin treatment. Collectively these results implicate a role of myosin contractility in regulatory volume decrease and cell shape regulation in response to hypoosmotic shock.

Changes in Cytoskeletal Localization in Response to Osmotic Loading

To test whether osmotically induced changes altered cytoskeletal localization we examined changes in actin and microtubules following 30 min of osmotic treatment (*fig 5.5*). In control cells, as expected, actin was present throughout the entirety of the cell body and neurites with the exception of the nuclear region, and was especially concentrated near the cell membrane (*fig 5.*5*a*). Tubulin also showed clear staining throughout the cell, also with a lack of signal at the nucleus. As expected, most neuronal processes contained both actin and tubulin, with regions near the tips of processes enriched in actin. Following hyperosmotic treatment for 30 min, there were no major disruptions or changes in the fundamental pattern of intraneuronal actin or tubulin networks, nor were there changes in filopodial density (*fig 5.5b*). However, in response to 30 min of hypoosmotic treatment, cells showed a large increase in branched neuronal processes heavily enriched in actin, but not tubulin (*fig 5.5c*). Such structures were occasionally observed in bright field and DIC images, and typically extended in the direction of subsequent cellular movement, described below.

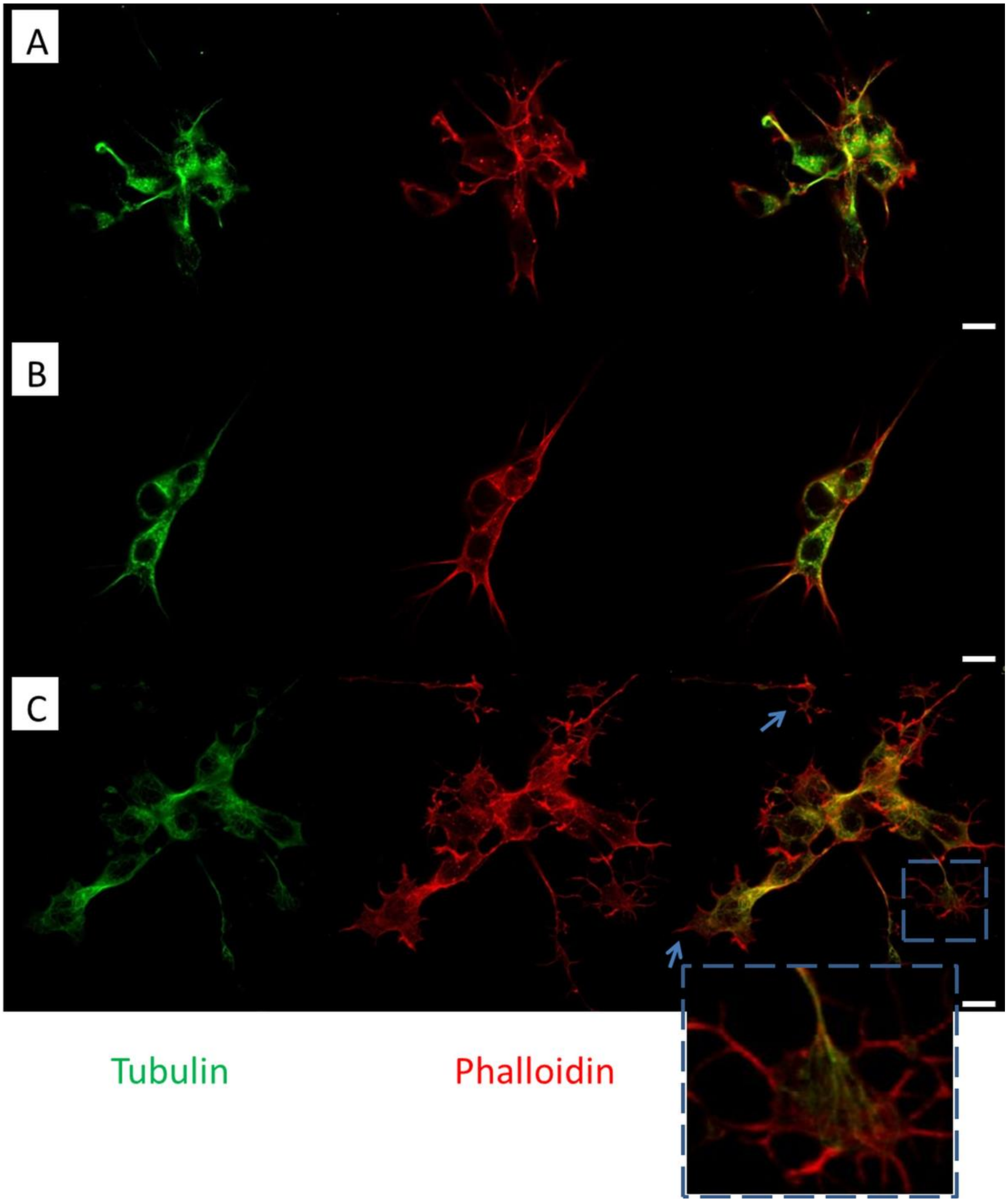

Figure 5.5 – Osmotic effects on the cytoskeleton.
SH-SY5Y cell immunostains of tubulin, phalloidin, and overlaid channels under osmotic stress. (a) Control cells. (b) Cells exposed to C=1.3 media for 30 min. (c) Cells exposed to C=0.6 media for 30 min. Note the increased presence of actin-rich projections (arrows). Scale bar=10 mm.

Changes in Neuronal Translocation Following Osmotic Loading

Cellular translocation relative to the substrate was frequently noted to change in response to osmotic loading, and was categorized as crawling or tugging. A tug was classified as a movement of the cell body along an adjacent axon or along its own axon (*fig 5.6*b). A cell was considered to crawl if it developed short projections near the cell body and experienced a quick but large cell body deformation followed by a large movement (*fig 5.6*c). While both hyper- and hypoosmotic shock qualitatively resulted in increased translocation, the characteristics of that movement differed significantly (P < 0.0001, Pearson's chi-square, *fig 5.6*a). Hyperosmotic shock appeared to induce cell tugging, typically toward other cells or along an adjacent retracting axon, while hypoosmotic loading induced crawling. A trivial explanation for these phenotypes was differences in connectivity to other cells. However, cells analyzed in all groups were connected to at least one other cell and no more than four other cells, and there was no difference in connectivity across groups. While other cells did influence movement by providing a stable site of attachment, there was no apparent relationship between the number of connected cells and the type of movement.

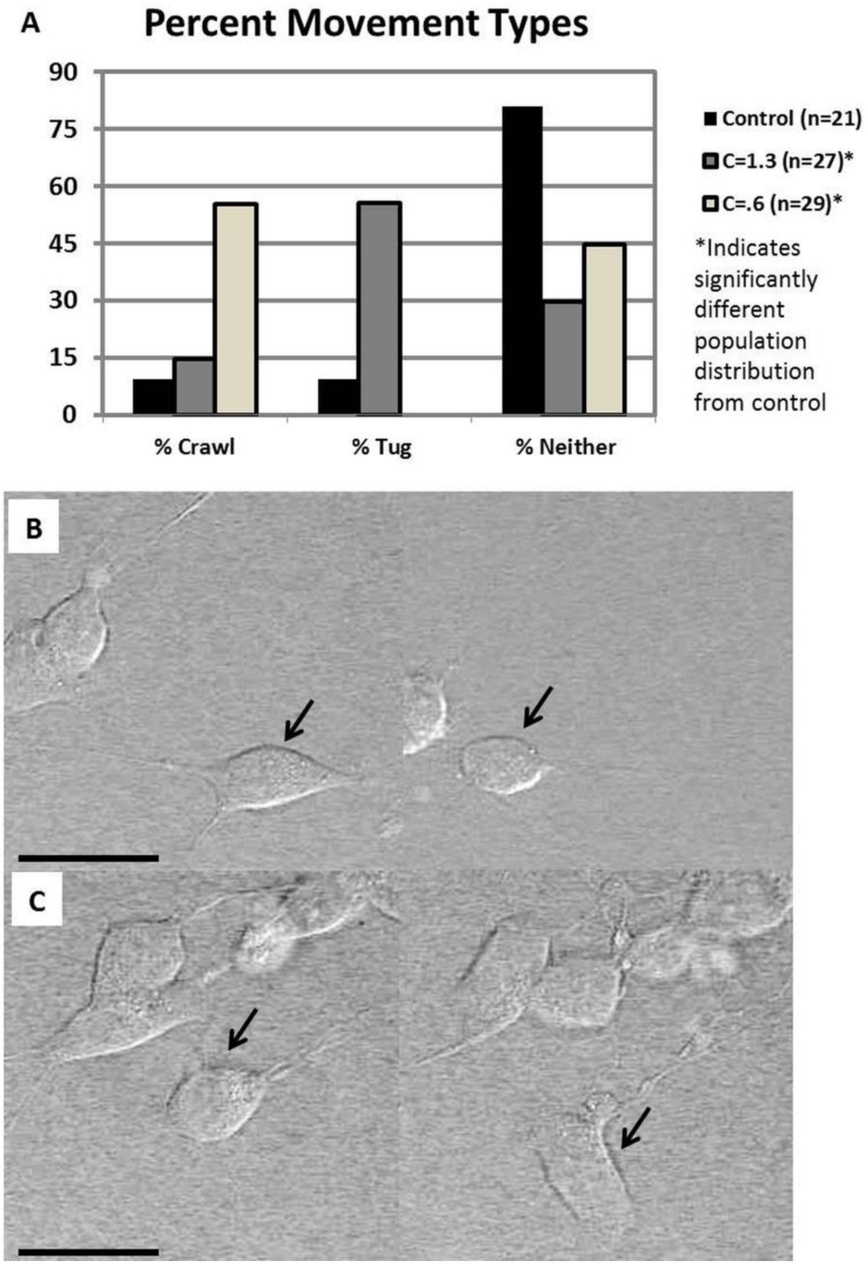

Fig 5.6 – Types of movement for each treatment group
(a) Population observations of cellular movement types. A crawl represents the formation of cell processes and gross deformation of the cell body while the cell moves to a new location. A tug represents cells being pulled toward other cells by nearby axons. N5number of observations made—a few cells displayed both tugging and crawling and thus counted as two observations. Both C =1.3 and C=0.6 groups showed significantly different movement distributions compared to the control group using Pearson’s chi-squared test (P<0.0001), indicated by *’s in the legend. Drug-treated cells remained stationary and were not included in this comparison. (b) Cell exposed to hyperosmotic media showing tugging along a retracting neurite. Arrow indicates cell of interest. (c) Cell exposed to hypoosmotic media showing large deformation during a crawl. Arrow indicates cell of interest. Scale bar=20 mm.

In order to quantify and compare net cellular translation (displacement from original location) in control and latrunculin- or blebbistatin-treated cells over the course of 30-min postosmotic insult (*fig 5.7*), we developed a new metric, termed the normalized movement footprint (detailed in methods for image processing). Two-way ANOVA showed a significant effect of osmotic and drug treatment on the normalized movement footprint ($P < 0.05$), and a strong trend of an interaction ($P = 0.058$) between osmotic and drug treatment effects, indicating that osmotic treatment can influence cellular translocation through actin–myosin dependent mechanisms. Post hoc analysis revealed statistically significant increases in movement following both hyper- and hypoosmotic treatment in nondrug-treated cells. Furthermore, nondrug-treated cells were more mobile than drug-treated cells across all groups; after both latrunculin and blebbistatin treatment, no significant movement was observed and 100% of cells were categorized as stationary.

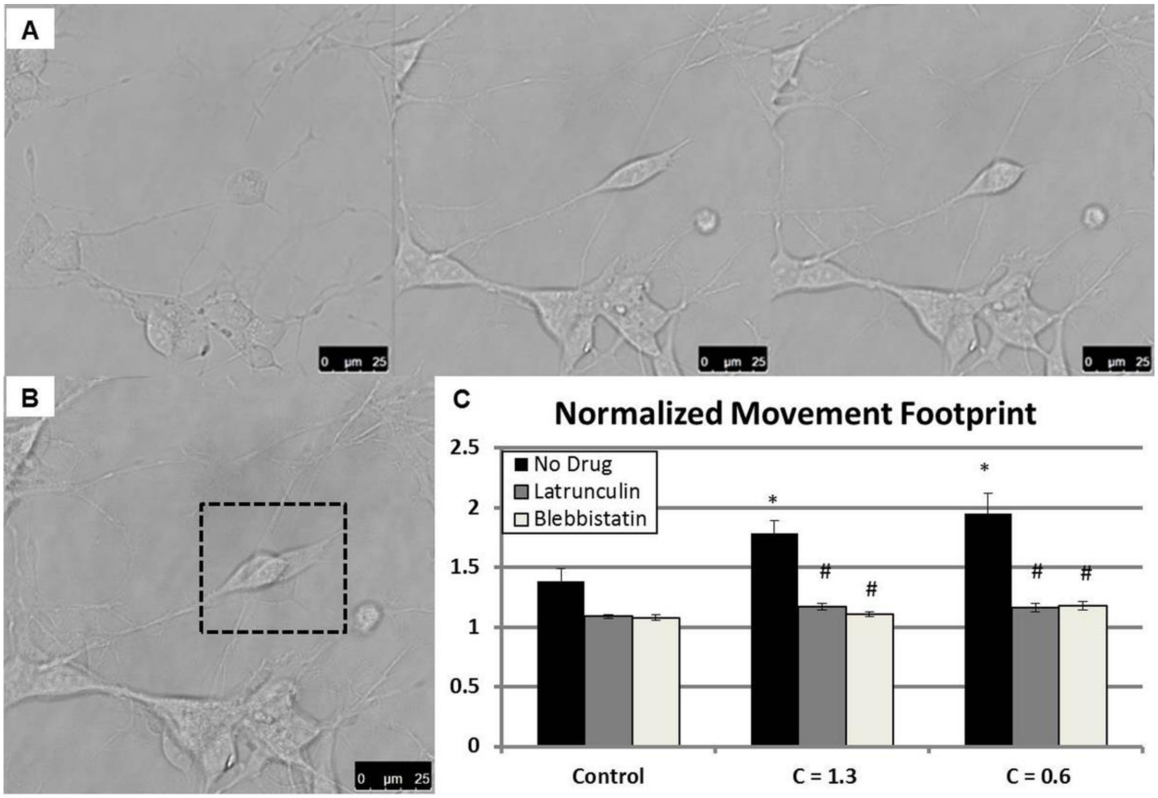

Fig 5.7 – Movement footprint analysis
(a) Images taken of cells exposed to hyperosmotic media at various times showing changes in cell shape and position. (b) Contrast enhanced movement footprint of same cells showing the path of a neuron over the course of 30 min with the dotted box indicating the cell analyzed. The normalized movement footprint is computed by dividing the area of the movement footprint and by the initial area. (c) Normalized movement footprint values for each group. * represents a significant change (Tukey's HSD, α=0.05) compared to control osmolarity. # represents a significant change compared to nondrug-treated group of the same osmotic condition. N=16 for each nondrug group and 9 for each drug-treated group. Error bars represent standard error of the mean.

5.4 Discussion

In this study, we examined actin and myosin dependent effect of hyper- and hypoosmotic shock on the morphology, movement, and cytoskeletal protein patterns of differentiated neuronal cells. Hyperosmotic treatment resulted in a rapid and persisting shape elongation (*figs 5.2c and 5.2d*) which did not occur after actin or myosin disruption (*fig 5.4*), as well as a persisting volume change (*fig 5.3a*). Hypoosmotic treatment resulted in a slower but persisting shape change, which was even more pronounced in drug-treated cells, and a more transient volume change. Both treatment types resulted in increased, but characteristically different, cell movement (*fig* 5*.6 and 5.7*) which was dependent upon an intact actin–myosin network. Immunocytochemistry revealed the presence actin-rich projections developing near the cell body and neurites of hypoosmotic-treated cells

Alterations in Geometry and Movement in Response to Osmotic Shock

In response to osmotic shock, cells are initially expected to increase or decrease volume in the direction dictated by the osmotic gradient, spawning changes in the expression and activity of membrane channels[160,161,171] as well as cytoskeletal remodeling, toward restoration of homeostasis[162,172,173]. Volume regulatory mechanisms are well studied in non-neuronal cells, but there is less information on structural and geometric changes to osmotic stress, particularly in neurons.

Initially, as expected, hyper- and hypoosmotic shock caused a decrease and increase in cell body volume, respectively. Interestingly, while cells exposed to hyperosmotic media experienced this decrease quickly within the first 30 s, cells exposed to hypoosmotic media experienced a slower volume increase that was detectable at 5 min, but not at 30 s. By 30 min, cells in hypoosmotic media were able to achieve a near baseline cell body volume, whereas volume remained reduced for cells in hyperosmotic media, indicating a failure in volume regulatory machinery. Consistent with previous literature, area measurements showed that actin disruption further reduced the capability of the cells to undergo regulatory volume increases and decreases[163,164] (*fig 5.4*). Interestingly, blebbistatin treatment had less of an effect on the volume (area) regulatory response than latrunculin, implicating a motor independent response to hyperosmotic perturbation.

Disruption of the actin–myosin network resulted in a profound effect on cellular shape changes. While cells were expected to decrease in volume in response to hyperosmotic treatment, nondrug-treated cells became more elliptical, likely due to substrate adhesions imposing geometric constraints during volume reduction. When treated with latrunculin or blebbistatin, cells trended toward a more circular morphology over time under hyperosmotic conditions, indicating that shape changes are naturally regulated by or result from actin–myosin interactions. Similarly, hypoosmotic-treated cells were significantly more round at 30 min after treatment with either drug—a likely consequence of reduced cellular contractility.

Osmotically induced differences among measured parameters were observed in spite of large cell to cell variability, emphasizing the magnitude of the effect of osmotic perturbation on cell morphology. Variability was likely due to differences in both cell to cell and cell to substrate adhesion. Hyperosmotic media in particular induced a wide range of changes in cell body area and shape, depending on the pattern of retracting neurites and moving cells contacting them, which, though also creating variability, are consistent with theoretical and experimental observations that cell-substrate interactions and membrane tension strongly influence the response of molluscan neurons to osmotic stress[174,175].

Regression analysis enabled us to identify trends within highly variable data sets, and suggested that though change in area can be a good predictor of aspect ratio, change in perimeter tends to be the larger predictor of this parameter. Thus, cellular shape is likely to reflect geometric constraints as well as the volume regulatory response of cells.

Taken collectively, neuronal cells seemed better equipped to adapt to hypoosmotic shock than hyperosmotic shock in terms of volume and area regulation, but in both cases, regardless of the effectiveness of such regulation, the cells were unable to easily correct their altered shapes. On the other hand, increased variability in most measured parameters at 30 min compared to 5 min suggests that the degree of correction was highly variable, likely due to the complexity associated with a physically interconnected neuronal network. Future studies will reveal whether these shape changes persist or are reversible following a return to isoosmotic conditions, but it is plausible that long-term shape changes in a cell would alter intracellular biological activity due to altered surface area to volume ratios, communication between the cell and its mechano-chemical environment, and even communication within compartments of the cell, including nuclei, whose volumetric response, at least qualitatively, does not appear to be perfectly coupled to the rest of the cell.

Another interesting impact of osmotic stress was an increase in cellular translocation. Hyper- and hypoosmotic stress both resulted in a similar change in the magnitude of cellular movement. However, the types of movement observed were different. Hyperosmotic-treated cells were often directionally tugged. This may be explained, at least in part, by the retraction of neurites. The shortening of a neurite often resulted in a force sufficient to tug and displace an attached cell. Similarly, projections were also observed to pull their own cell body toward them, presumably if tension produced was strong enough to disrupt adhesion of the cell body. Alternately, if the cell body elongated, this occasionally deflected neighboring cells, and vice versa. As expected, disruption of actin or myosin resulted in a marked reduction in cellular translocation—inhibition of contractility halts axonal retraction[168] and likely prevented cellular tugging observed here.

Unlike cells subjected to hyperosmotic shock, hypoosmotically treated cells sometimes developed small processes, grossly deformed at later time points, and “crawled” to new nearby locations. This phenomenon is less easily explainable. It is possible that uncoordinated disruption in cell– substrate adhesion due to swelling and short-term cortical actin disruption that is known to occur during hypoosmotic treatment[160,176] could destabilize the cell and result in the cell moving to a new location. Such a phenomenon is analogous to membrane blebbing, which can occur when the cortical cytoskeleton is disrupted in response to an increase in intracellular pressure[177] and has been suggested as a mechanism for cell migration[178] and cell spreading[179]. Regardless, crawling behavior was halted by actin or myosin disruption, indicating it is an active contractile process.

In addition, immunocytochemistry revealed an increase in the density of actin-rich branches near the cell bodies and tips of neurites following hypoosmotic treatment (*fig 5.5c*). These projections appear related to filipodia or lamellaepodia, which are actin-rich and devoid of tubulin, and traditionally implicated in neuron movement[169]. Given the high frequency of cellular “crawling” exhibited by cells after hypoosmotic treatment, these projections likely played roles in cell migration or subsequent stabilization. Immunolabeling did not reveal any obvious differences in cytoskeletal integrity in response to osmotic perturbation at a 30-min time point, suggesting that the cytoskeleton effectively accommodates (or, potentially, guides) changes in cell shape. Previous studies have shown that hyperosmotic perturbation can cause an increase in F-actin polymerization[160,180], while hypoosmotic perturbation can cause a transient depolymerization of actin[176] likely related to intracellular Ca^{2+} levels that change during swelling[160,181]. Our study did not show such changes, perhaps due to insufficient temporal and/or spatial resolution.

Finally, a natural question is to ask whether primary neurons, such as hippocampal or dorsal root ganglion neurons would respond similarly to neuroblastoma cells. While specific adhesive patterns are likely different from those of SY5Y cells, based on of the existence of these cells in extracellular matrix and/or neuronal networks, conceptually, we expect similar results. Future studies will directly test these possibilities.

5.5 Conclusion

Our data reveal that osmotic perturbations to a cell can cause significant changes to neuronal morphology. In addition, both hyper- and hypoosmotic shock caused an increase in cellular movement; however, differences in the nature of observed motion suggest that hyper- and hypoosmotic shock may perturb cellular function through different pathways. Though distinct compensatory cellular responses were observed within 30 min, effects were variable and not fully reversible within this time frame, particularly in regards to cell shape changes. Compensatory responses were alterable by actin–myosin disruption, and thus tied to their activity. These findings have significant implications for both our fundamental understanding of neuronal compensatory response to osmotic shock as well as the susceptibility of neurons to dysfunction in the context of neurological injury and disease.

5.6 Materials and Methods

Cell Culture

SH-SY5Y (referred to henceforth as SY5Y) human neuroblastoma cells varying from passages 18 to 25 were grown in media containing 45% Eagles Minimum Essentials Media (ATCC), 45% F-12 media (Gibco), and 10% fetal bovine serum (Gibco). Glass-bottom cell culture dishes (MatTek Corp.) were coated in laminin (Sigma-Aldrich) for 2 h at a concentration of 10 μg/mL in PBS. SY5Y cells were added to the dishes for 2 h to allow for attachment, at which point 10 μM retinoic acid was added for 5 days in order to induce differentiation into a neuronal phenotype[182].

Experimental Groups

Retinoic acid differentiated SY5Y cells were given a fresh media change 30 min prior to experimentation with the exception of a control group where no media change was performed. Fresh media osmolarity was measured to be 320 mOsm. Media was concentrated by the addition of sorbitol or diluted by the addition of distilled water. After 30 min of fresh media exposure, a micropipette was used to add the same volume of new media to each dish, concentrating or diluting the media to a final concentration of either 1.3 times (C = 1.3, 420 mOsm) or 0.6 times (C = 0.6, 190 mOsm) the normal media osmolarity. Osmolarity was measured using a vapor pressure osmometer (Vapro, Wescor, Logan, UT). Mixing was rapid. Cells were exposed to the hyper- or hypoosmotic media for 30 min. To test for perturbations due to media change, an additional group in which a fresh media change was performed 30 min prior to imaging was compared to control cells with no media change; however, no significant differences were detected in any measure (data not shown). For viability testing, cells were incubated in media whose osmolarity was varied from 140 to 730 mOsm. For cells that were treated with drugs, 10 μM latrunculin B or 20 μM blebbistatin in 0.05% (by volume) DMSO were added to the cells 10 min prior to imaging. These dosages have been shown to be large enough to effectively perturb cells in prior experiments[168,183].

Immunocytochemistry and Cell Viability

Cells were fixed in a 2% paraformaldehyde/0.25% glutaraldehyde mixture for 10 min, permeabilized in 0.1% Triton-X100 for 2 min, blocked in 3% BSA/10% fetal goat serum in PBS for 30 min, and incubated at room temperature with primary antibodies for 1 h. An anti-tubulin monoclonal antibody was used (Sigma-Aldrich T9026, 1:1000 dilution) to detect tubulin. Cells were then incubated in

AlexaFluor-488 goat-anti-mouse secondary antibody (Invitrogen, 1:200 dilution) for 2 h at room temperature. Alternatively, AlexaFluor-594 conjugated phalloidin (Invitrogen) was added to the cells postfixation and permeabilization according to manufacturer specifications to stain for filamentous actin. To test cell viability, a Live/Dead assay (Life Technologies, L-3224) was performed on cells treated for 24 h per protocols included with product literature.

Live Imaging and Microscopy

Culture dishes were placed on a Leica SP5 confocal microscope within an environmental chamber (Tokai Hit), which maintained a temperature of 37 –C, with constant airflow of 5% CO_2. Cells were imaged for 30 min using a 633 glycerol immersion lens with images captured every 10 s. Bright field and differential interference contrast (DIC) images were captured. In order to calculate volume, fluorescent wheat germ agglutinin (Invitrogen, W6748) was added to the media of the cells to stain the cell membrane, and image slices were acquired at varying depths with step sizes of 1.5 μm. Volume was then approximated by summing the products of the area of the cell in each slice by the step size until the cell membrane was no longer visible, analogous to other 3-dimensional reconstruction techniques[184].

Image Processing

Videos were collected and analyzed using ImageJ and MATLAB. Frames used for subsequent morphology calculations were at the initial, 30-s, 5-min, and 30-min time points. Candidate cells were identified based on presence of a major projection whose length exceeded the diameter of the cell body. Cell bodies and projection lengths were traced manually, ignoring minor projections of lengths less than half of the cell body diameter or filopodia-like processes. ImageJ was used to quantify changes in axon length, circularity, aspect ratio, and area in the imaging plane. The shape descriptors circularity and aspect ratio were defined as:

$$Circularity = \frac{4 * \pi * area}{perimeter^2}$$

$$Aspect\ Ratio = \frac{major\ axis\ length}{minor\ axis\ length}$$

A custom MATLAB script was used to calculate a novel movement parameter termed the normalized movement footprint. The initial area of the cell body was calculated by manually tracing the cell. Evenly spaced frames from each movie were made 75–85% transparent and overlaid on top of each other. The resulting image showed a projection of the full path taken by the cell during the imaging period (*Figs* 5-7a and 5-7b). The area of the composite image, which was called the movement footprint, was then calculated by manual tracing. By dividing the movement footprint by the initial area, we obtained the normalized movement footprint. Slight vibration of the plate or camera may have slightly increased the movement footprint; however, this effect was the same for all groups and thus did not affect the results.

Statistics

Normality of the data within each group was verified using the Jarque-Bera test, showing approximately 75% of the groups to have skewness and kurtosis matching a normal distribution. In the remaining cases, putative outliers seemed to cause significantly skewed samples, though this did not alter the interpretation of the data. We elected not to remove outliers, as there was no experimental basis to do so, resulting in a more inclusive data set. Significant effects were determined using one or two-way ANOVA with significant differences designated for $P < 0.05$. Post hoc comparisons were performed using Tukey's honest significant difference test or Student's t tests with a Bonferroni correction factor and $\alpha = 0.05$ to determine significant differences between individual groups at the same time point and account for multiple comparisons. Each group contained 12–16 cells analyzed for nondrug-treated cells and 9 cells for drug-treated cells. Sample sizes were chosen based on a power analysis using $\alpha = 0.05$ and $\beta = 0.2$. For an effect size given by Cohen's $d = 1.5$, based on means and standard deviations from preliminary data, a significant difference between two means can be detected using eight samples per group. A post-hoc calculation using $\alpha = 0.05$ shows that for the effect sizes determined and sample sizes used in this experiment, a statistical power of 0.80 ($\beta = 0.2$.) or higher was achieved for all significant comparisons, with many comparisons achieving a power >0.90.

Multiple linear regression analysis on the morphological data was performed using MATLAB. Data from each time point (30 s, 5 min, and 30 min) was pooled and grouped according to the osmotic loading condition prior to regression. Aspect ratio was regressed against the predictors change in area, change in perimeter, and change in axon length.

5.7 Acknowledgments

I acknowledge the publisher, Cytoskeleton, for publishing the manuscript presented in this chapter, titled “Actin-myosin network influences morphological response of neuronal cells to altered osmolarity.” I also acknowledge all of the co-authors (James Love, Steven Horton, Mariya Sitnova, Sinan Shahamatdar, Ajay Kannan, and Sameer Shah) for their contributions. We gratefully acknowledge funding support from the National Science Foundation (CBET-0932590 and CMMI-1130997) and Alzheimer’s Association (NIRG09133270) and appreciate valuable discussions with the Neuromuscular Bioengineering Laboratory.

CHAPTER 6: CONCLUSIONS AND FUTURE DIRECTIONS

6.1 Summary of Findings

Paclitaxel is a common chemotherapy drug that binds to the inner lumen of microtubules[53], increasing their stability and promoting polymerization. While effective as an anti-cancer agent, due to its systemic delivery and activity in non-cancerous cells, paclitaxel causes peripheral neuropathy in a large percentage of patients for reasons that are not yet clearly understood. These symptoms can be severe and often limit maximum drug dosages used. Within axons, microtubules largely serve two purposes – they support axonal structure and bear loads, and they act as tracks upon which molecular motors can deliver important cargoes to and from the distal reaches of the axon. This dissertation therefore explores the consequences of paclitaxel exposure in neurons to parameters relating to these functions of microtubules.

In chapter 2, it was shown that by altering the microtubule network, paclitaxel perturbs axonal transport of mitochondria, synaptophysin, and actin by decreasing the frequency and velocity of their movements. In addition, while stretch alone had little impact on axonal transport, in neurons that were treated with paclitaxel, stretch exacerbated transport defects. Thus, paclitaxel fundamentally perturbs the ability of a neuron to withstand mechanical stretch, and stretch may play a role in exacerbating transport defects seen in paclitaxel treated neurons.

In chapter 3, it was demonstrated via electron microscopy that paclitaxel treatment increases microtubule clustering in axons within the sural nerve, a pure sensory nerve innervating regions of the foot in humans and hind paw in rats and mice. Mechanical testing was performed on control and paclitaxel soaked sural nerves, and revealed that paclitaxel stiffens the nerves both in the transition and linear regions of the stress-strain curve. Taken collectively, these results indicate that increases in microtubule density and packing likely contribute to alterations to tissue level properties in nerves.

In chapter 4, the mechanisms by which paclitaxel induces microtubule bundling are explored. Prior literature indicates that paclitaxel or microtubules stabilized by paclitaxel interact with other cellular factors which induce microtubule crosslinking. Here, tau was explored as a potential paclitaxel-stabilized-microtubule crosslinking candidate due to its known interactions with both paclitaxel and microtubule crosslinking under non-pathological conditions. Tau knockout mice showed partial resistance to microtubule clustering, as demonstrated by electron microscopy of nerves and biochemical assays of brain extract. However, lessening of microtubule bundling did not appear to result in resistance to neuropathy development following system delivery of paclitaxel, indicating that lessening of microtubule bundling due to removal of tau alone is not sufficient to prevent neuropathy, or that other, non-structural factors may be contributing to neuropathic side effects.

6.2 Significance

Chapters 2 and 3 primarily indicate that paclitaxel fundamental alters both the mechanical properties of nerves and the ability of neurons to adapt to mechanical loads. Given that peripheral nerves exist in a dynamic environment where tensile loading is necessarily imposed on nerves during joint motion[4], these observations have potential implications for the management of patients receiving paclitaxel based therapy. For example, because transport deficits were exacerbated during periods of loading, it is possible that immobilization or light exercise following chemotherapy could potentially improve neuropathic side effects in patients. Light exercise in particular has shown to be somewhat beneficial following chemotherapy treatment[185-188]. In addition, changes to the mechanical properties of nerves could alter strain profiles in axons, which could further cause nerve damage. There is precedent for evaluating and managing mechanical contributions to neuropathy in the context of nerve entrapment[11,189,190], which shares several common neuropathic outcomes to paclitaxel neuropathy. Overall, by identifying these novel contributions to nerve changes following paclitaxel treatment, future studies can be carefully designed to analyze their roles in neuropathic development, and can guide future patient management protocols.

Chapter 4 primarily indicates that tau plays a significant role in the development of microtubule bundles following paclitaxel treatment, though other factors also appear to contribute to bundle development as well. Microtubule bundling has been hypothesized to play a role in the development of paclitaxel induced neuropathy. Identifying molecular targets responsible for this phenomenon therefore has the potential help develop targeted treatments to prevent or alleviate nerve damage following paclitaxel treatment. Finally, because removal of tau alone was not sufficient to prevent development of neuropathy, other factors can be more carefully analyzed in future studies.

6.2 Future Directions

There are several potential areas to expand on the body of work presented here in future studies. Given the apparent mechanical sensitivity of neurons to transport disruption following paclitaxel treatment *in vitro*, future studies should analyze the importance of this factor *in vivo*. This can be accomplished, for example, by assessing neuropathic outcomes of animals forced to undergo exercise or animals under forced immobilization. In addition, bulk transport rates in nerves can be measured using techniques from previous studies such as injection of radiolabeled amino acids into nerves[36] to see if transport is directly altered by these types of interventions, and if it correlates with neuropathic outcomes.

Other future work should verify that mechanical stiffening of nerves following paclitaxel treatment occurs *in vivo* due to systemic delivery of paclitaxel. In addition, it is important to determine the impacts of mechanical stiffening of nerves. This can be accomplished, for example, by measuring nerve strains during movement following paclitaxel treatment, or more importantly, observing dynamics of axonal unpacking during nerve strain. One way to visualize axonal unpacking of nerves is to utilize fluorescent markers in axons to visualize their tracks on the nerve interior via microscopy. To more accurately analyze individual axons, mixed color axonal markers can be employed, such as those observed in brainbow mice where axons express a differential and wide variety of fluorescent proteins, enabling easier study of individual axon tracks.

Finally, given that tau knockout mice showed reduced severity of structural defects following paclitaxel treatment, it would be interesting to see if some of the prior observed changes in nerve mechanics and axonal transport following paclitaxel treatment occurred in neurons and nerves from these mice. These results could further elucidate the role of tau in the development of paclitaxel induced neuropathy. Furthermore, this analysis could provide further insight into general mechanisms of peripheral neuropathy. For example if removal of tau sufficiently ameliorates transport defects following paclitaxel treatment, but tau knockout mice still develop neuropathy, it could be concluded that axonal transport is not the primary site of the development of neuropathy. Currently, studies of paclitaxel induced neuropathy have not yet been able to define a primary site of disease pathogenesis. Therefore, analyses such as those proposed above will be critical in identifying the major mechanisms of neuropathy, which can then further guide the development of treatments.

REFERENCES

1. Debanne D, Campanac E, Bialowas A, Carlier E, Alcaraz G. Axon physiology. Physiol Rev 2011;91:555-602.

2. Crochot, W. A diagram of the human nervous system. 2014. (Accessed 7/10/20155, at https://commons.wikimedia.org/wiki/File:Nervous_system_diagram-en.svg.)

3. McDonald DS, Bell MS. Peripheral nerve gap repair facilitated by a dynamic tension device. Can J Plast Surg 2010;18:e17-9.

4. Topp KS, Boyd BS. Structure and biomechanics of peripheral nerves: nerve responses to physical stresses and implications for physical therapist practice. Phys Ther 2006;86:92-109.

5. Millesi H, Zoch G, Reihsner R. Mechanical properties of peripheral nerves. Clin Orthop Relat Res 1995:76-83.

6. Aoki M, Takasaki H, Muraki T, Uchiyama E, Murakami G, Yamashita T. Strain on the ulnar nerve at the elbow and wrist during throwing motion. J Bone Joint Surg Am 2005;87:2508-14.

7. Tanoue M, Yamaga M, Ide J, Takagi K. Acute stretching of peripheral nerves inhibits retrograde axonal transport. J Hand Surg Br 1996;21:358-63.

8. Ogata K, Naito M. Blood flow of peripheral nerve effects of dissection, stretching and compression. J Hand Surg Br 1986;11:10-4.

9. Wall EJ, Massie JB, Kwan MK, Rydevik BL, Myers RR, Garfin SR. Experimental stretch neuropathy. Changes in nerve conduction under tension. J Bone Joint Surg Br 1992;74:126-9.

10. Szabo RM, Chidgey LK. Stress carpal tunnel pressures in patients with carpal tunnel syndrome and normal patients. J Hand Surg Am 1989;14:624-7.

11. Mackinnon SE. Pathophysiology of nerve compression. Hand Clin 2002;18:231-41.

12. Mahan MA, Vaz KM, Weingarten D, Brown JM, Shah SB. Altered Ulnar Nerve Kinematic Behavior in a Cadaver Model of Entrapment. Neurosurgery 2015.

13. Sanz J, Lizaur A, Sanchez Del Campo F. Postoperative changes of carpal canal pressure in carpal tunnel syndrome: a prospective study with follow-up of 1 year. J Hand Surg Br 2005;30:611-4.

14. Haninec P. Undulating course of nerve fibres and bands of Fontana in peripheral nerves of the rat. Anat Embryol (Berl) 1986;174:407-11.

15. Merolli A, Mingarelli L, Rocchi L. A more detailed mechanism to explain the "bands of Fontana" in peripheral nerves. Muscle Nerve 2012;46:540-7.

16. Clarke E, Bearn JG. The spiral nerve bands of Fontana. Brain 1972;95:1-20.

17. Love JM, Chuang TH, Lieber RL, Shah SB. Nerve strain correlates with structural changes quantified by Fourier analysis. Muscle Nerve 2013;48:433-5.

18. Anatomy & Physiology. 2013. (Accessed 7/10/2015, at http://cnx.org/content/col11496/1.6/.)

19. Rydevik BL, Kwan MK, Myers RR, Brown RA, Triggs KJ, Woo SL, Garfin SR. An in vitro mechanical and histological study of acute stretching on rabbit tibial nerve. J Orthop Res 1990;8:694-701.

20. Wall EJ, Kwan MK, Rydevik BL, Woo SL, Garfin SR. Stress relaxation of a peripheral nerve. J Hand Surg Am 1991;16:859-63.

21. Kwan MK, Wall EJ, Massie J, Garfin SR. Strain, stress and stretch of peripheral nerve. Rabbit experiments in vitro and in vivo. Acta Orthop Scand 1992;63:267-72.

22. Haas, J. Neurons uni bi multi pseudouni. 2012. (Accessed 7/10/2015, at https://commons.wikimedia.org/wiki/File:Neurons_uni_bi_multi_pseudouni.svg.)

23. Ouyang H, Nauman E, Shi R. Contribution of cytoskeletal elements to the axonal mechanical properties. J Biol Eng 2013;7:21.

24. Lee MK, Cleveland DW. Neuronal intermediate filaments. Annu Rev Neurosci 1996;19:187-217.

25. Hrdina PD. Basic neurochemistry: Molecular, cellular and medical aspects - Siegel,GJ. J Psychiatry Neurosci 1996;21:352-3.

26. Bowne-Anderson H, Zanic M, Kauer M, Howard J. Microtubule dynamic instability: a new model with coupled GTP hydrolysis and multistep catastrophe. Bioessays 2013;35:452-61.

27. Conde C, Caceres A. Microtubule assembly, organization and dynamics in axons and dendrites. Nat Rev Neurosci 2009;10:319-32.

28. Weisenberg RC, Deery WJ, Dickinson PJ. Tubulin-nucleotide interactions during the polymerization and depolymerization of microtubules. Biochemistry 1976;15:4248-54.

29. Gordon-Weeks PR. Microtubules and growth cone function. J Neurobiol 2004;58:70-83.

30. Hirokawa N. Cross-linker system between neurofilaments, microtubules, and membranous organelles in frog axons revealed by the quick-freeze, deep-etching method. J Cell Biol 1982;94:129-42.

31. Turner PF, Margolis RL. Taxol-induced bundling of brain-derived microtubules. J Cell Biol 1984;99:940-6.

32. Ahmadzadeh H, Smith DH, Shenoy VB. Viscoelasticity of tau proteins leads to strain rate-dependent breaking of microtubules during axonal stretch injury: predictions from a mathematical model. Biophys J 2014;106:1123-33.

33. Tang-Schomer MD, Johnson VE, Baas PW, Stewart W, Smith DH. Partial interruption of axonal transport due to microtubule breakage accounts for the formation of periodic varicosities after traumatic axonal injury. Exp Neurol 2012;233:364-72.

34. Tang-Schomer MD, Patel AR, Baas PW, Smith DH. Mechanical breaking of microtubules in axons during dynamic stretch injury underlies delayed elasticity, microtubule disassembly, and axon degeneration. FASEB J 2010;24:1401-10.

35. Campenot RB, Eng H. Protein synthesis in axons and its possible functions. J Neurocytol 2000;29:793-8.

36. Willard M, Cowan WM, Vagelos PR. The polypeptide composition of intra-axonally transported proteins: evidence for four transport velocities. Proc Natl Acad Sci U S A 1974;71:2183-7.

37. Miller KE, Samuels DC. The axon as a metabolic compartment: protein degradation, transport, and maximum length of an axon. J Theor Biol 1997;186:373-9.

38. Hoffman PN, Lasek RJ, Griffin JW, Price DL. Slowing of the axonal transport of neurofilament proteins during development. J Neurosci 1983;3:1694-700.

39. Chang S, Rodionov VI, Borisy GG, Popov SV. Transport and turnover of microtubules in frog neurons depend on the pattern of axonal growth. J Neurosci 1998;18:821-9.

40. Grafstein B, Forman DS. Intracellular transport in neurons. Physiol Rev 1980;60:1167-283.

41. Miller KE, Heidemann SR. What is slow axonal transport? Exp Cell Res 2008;314:1981-90.

42. Wang L, Ho CL, Sun D, Liem RK, Brown A. Rapid movement of axonal neurofilaments interrupted by prolonged pauses. Nat Cell Biol 2000;2:137-41.

43. Roy S, Coffee P, Smith G, Liem RK, Brady ST, Black MM. Neurofilaments are transported rapidly but intermittently in axons: implications for slow axonal transport. J Neurosci 2000;20:6849-61.

44. Wang L, Brown A. Rapid movement of microtubules in axons. Curr Biol 2002;12:1496-501.

45. Brown A, Wang L, Jung P. Stochastic simulation of neurofilament transport in axons: the "stop-and-go" hypothesis. Mol Biol Cell 2005;16:4243-55.

46. Salinas S, Bilsland LG, Schiavo G. Molecular landmarks along the axonal route: axonal transport in health and disease. Curr Opin Cell Biol 2008;20:445-53.

47. Juranek JK, Geddis MS, Rosario R, Schmidt AM. Impaired slow axonal transport in diabetic peripheral nerve is independent of RAGE. Eur J Neurosci 2013;38:3159-68.

48. Argyriou AA, Kyritsis AP, Makatsoris T, Kalofonos HP. Chemotherapy-induced peripheral neuropathy in adults: a comprehensive update of the literature. Cancer Manag Res 2014;6:135-47.

49. Scripture CD, Figg WD, Sparreboom A. Peripheral neuropathy induced by paclitaxel: recent insights and future perspectives. Curr Neuropharmacol 2006;4:165-72.

50. Lipton RB, Apfel SC, Dutcher JP, Rosenberg R, Kaplan J, Berger A, Einzig AI, Wiernik P, Schaumburg HH. Taxol produces a predominantly sensory neuropathy. Neurology 1989;39:368-73.

51. Lee JJ, Swain SM. Peripheral neuropathy induced by microtubule-stabilizing agents. J Clin Oncol 2006;24:1633-42.

52. Gornstein E, Schwarz TL. The paradox of paclitaxel neurotoxicity: Mechanisms and unanswered questions. Neuropharmacology 2014;76 Pt A:175-83.

53. Prota AE, Bargsten K, Zurwerra D, Field JJ, Diaz JF, Altmann KH, Steinmetz MO. Molecular Mechanism of Action of Microtubule-Stabilizing Anticancer Agents. Science 2013;339:587-90.

54. Schiff PB, Horwitz SB. Taxol assembles tubulin in the absence of exogenous guanosine 5'-triphosphate or microtubule-associated proteins. Biochemistry 1981;20:3247-52.

55. Diaz JF, Valpuesta JM, Chacon P, Diakun G, Andreu JM. Changes in microtubule protofilament number induced by Taxol binding to an easily accessible site. Internal microtubule dynamics. J Biol Chem 1998;273:33803-10.

56. Hawkins TL, Sept D, Mogessie B, Straube A, Ross JL. Mechanical properties of doubly stabilized microtubule filaments. Biophys J 2013;104:1517-28.

57. Letourneau PC, Ressler AH. Inhibition of neurite initiation and growth by taxol. J Cell Biol 1984;98:1355-62.

58. Scuteri A, Nicolini G, Miloso M, Bossi M, Cavaletti G, Windebank AJ, Tredici G. Paclitaxel toxicity in post-mitotic dorsal root ganglion (DRG) cells. Anticancer Res 2006;26:1065-70.

59. Williamson T, Gordon-Weeks PR, Schachner M, Taylor J. Microtubule reorganization is obligatory for growth cone turning. Proc Natl Acad Sci U S A 1996;93:15221-6.

60. Shemesh OA, Spira ME. Paclitaxel induces axonal microtubules polar reconfiguration and impaired organelle transport: implications for the pathogenesis of paclitaxel-induced polyneuropathy. Acta Neuropathol 2010;119:235-48.

61. De Brabander M, Geuens G, Nuydens R, Willebrords R, De Mey J. Taxol induces the assembly of free microtubules in living cells and blocks the organizing capacity of the centrosomes and kinetochores. Proc Natl Acad Sci U S A 1981;78:5608-612.

62. Masurovsky EB, Peterson ER, Crain SM, Horwitz SB. Microtubule arrays in taxol-treated mouse dorsal root ganglion-spinal cord cultures. Brain Res 1981;217:392-8.

63. Sengottuvel V, Leibinger M, Pfreimer M, Andreadaki A, Fischer D. Taxol facilitates axon regeneration in the mature CNS. J Neurosci 2011;31:2688-99.

64. Brunden KR, Trojanowski JQ, Smith AB, 3rd, Lee VM, Ballatore C. Microtubule-stabilizing agents as potential therapeutics for neurodegenerative disease. Bioorg Med Chem 2014;22:5040-9.

65. Ballatore C, Brunden KR, Huryn DM, Trojanowski JQ, Lee VM, Smith AB, 3rd. Microtubule stabilizing agents as potential treatment for Alzheimer's disease and related neurodegenerative tauopathies. J Med Chem 2012;55:8979-96.

66. Vuorinen V, Roytta M, Raine CS. The long-term effects of a single injection of taxol upon peripheral nerve axons. J Neurocytol 1989;18:775-83.

67. Roytta M, Raine CS. Taxol-induced neuropathy: further ultrastructural studies of nerve fibre changes in situ. J Neurocytol 1985;14:157-75.

68. Roytta M, Horwitz SB, Raine CS. Taxol-induced neuropathy: short-term effects of local injection. J Neurocytol 1984;13:685-701.

69. Siau C, Xiao W, Bennett GJ. Paclitaxel- and vincristine-evoked painful peripheral neuropathies: loss of epidermal innervation and activation of Langerhans cells. Exp Neurol 2006;201:507-14.

70. Sahenk Z, Barohn R, New P, Mendell JR. Taxol neuropathy. Electrodiagnostic and sural nerve biopsy findings. Arch Neurol 1994;51:726-9.

71. Authier N, Gillet JP, Fialip J, Eschalier A, Coudore F. Description of a short-term Taxol-induced nociceptive neuropathy in rats. Brain Res 2000;887:239-49.

72. Mironov SL, Ivannikov MV, Johansson M. [Ca2+]i signaling between mitochondria and endoplasmic reticulum in neurons is regulated by microtubules. From mitochondrial permeability transition pore to Ca2+-induced Ca2+ release. J Biol Chem 2005;280:715-21.

73. Flatters SJ, Bennett GJ. Studies of peripheral sensory nerves in paclitaxel-induced painful peripheral neuropathy: evidence for mitochondrial dysfunction. Pain 2006;122:245-57.

74. Peters CM, Jimenez-Andrade JM, Kuskowski MA, Ghilardi JR, Mantyh PW. An evolving cellular pathology occurs in dorsal root ganglia, peripheral nerve and spinal cord following intravenous administration of paclitaxel in the rat. Brain Res 2007;1168:46-59.

75. Hara T, Chiba T, Abe K, Makabe A, Ikeno S, Kawakami K, Utsunomiya I, Hama T, Taguchi K. Effect of paclitaxel on transient receptor potential vanilloid 1 in rat dorsal root ganglion. Pain 2013;154:882-9.

76. Nakata T, Yorifuji H. Morphological evidence of the inhibitory effect of taxol on the fast axonal transport. Neurosci Res 1999;35:113-22.

77. Lapointe NE, Morfini G, Brady ST, Feinstein SC, Wilson L, Jordan MA. Effects of eribulin, vincristine, paclitaxel and ixabepilone on fast axonal transport and kinesin-1 driven microtubule gliding: Implications for chemotherapy-induced peripheral neuropathy. Neurotoxicology 2013;37:231-9.

78. Theiss C, Meller K. Taxol impairs anterograde axonal transport of microinjected horseradish peroxidase in dorsal root ganglia neurons in vitro. Cell Tissue Res 2000;299:213-24.

79. Das V, Sim DA, Miller JH. Effect of taxoid and nontaxoid site microtubule-stabilizing agents on axonal transport of mitochondria in untransfected and ECFP-htau40-transfected rat cortical neurons in culture. J Neurosci Res 2014.

80. Dixit R, Ross JL, Goldman YE, Holzbaur EL. Differential regulation of dynein and kinesin motor proteins by tau. Science 2008;319:1086-9.

81. Kar S, Fan J, Smith MJ, Goedert M, Amos LA. Repeat motifs of tau bind to the insides of microtubules in the absence of taxol. EMBO J 2003;22:70-7.

82. Mansfield SG, Gordon-Weeks PR. Dynamic post-translational modification of tubulin in rat cerebral cortical neurons extending neurites in culture: effects of taxol. J Neurocytol 1991;20:654-66.

83. Dunn S, Morrison EE, Liverpool TB, Molina-Paris C, Cross RA, Alonso MC, Peckham M. Differential trafficking of Kif5c on tyrosinated and detyrosinated microtubules in live cells. J Cell Sci 2008;121:1085-95.

84. Campbell EJ, MacKinlay SA, MacRae TH. Cross-linking of microtubules by microtubule-associated proteins (MAPs) from the brine shrimp, Artemia. J Cell Sci 1989;93 (Pt 1):29-39.

85. Hirokawa N, Shiomura Y, Okabe S. Tau proteins: the molecular structure and mode of binding on microtubules. J Cell Biol 1988;107:1449-59.

86. Takemura R, Okabe S, Umeyama T, Kanai Y, Cowan NJ, Hirokawa N. Increased microtubule stability and alpha tubulin acetylation in cells transfected with microtubule-associated proteins MAP1B, MAP2 or tau. J Cell Sci 1992;103 (Pt 4):953-64.

87. Kanai Y, Chen J, Hirokawa N. Microtubule bundling by tau proteins in vivo: analysis of functional domains. EMBO J 1992;11:3953-61.

88. Kanai Y, Takemura R, Oshima T, Mori H, Ihara Y, Yanagisawa M, Masaki T, Hirokawa N. Expression of multiple tau isoforms and microtubule bundle formation in fibroblasts transfected with a single tau cDNA. J Cell Biol 1989;109:1173-84.

89. Ross JL, Santangelo CD, Makrides V, Fygenson DK. Tau induces cooperative Taxol binding to microtubules. Proc Natl Acad Sci U S A 2004;101:12910-5.

90. Samsonov A, Yu JZ, Rasenick M, Popov SV. Tau interaction with microtubules in vivo. J Cell Sci 2004;117:6129-41.

91. Xie H, Litersky JM, Hartigan JA, Jope RS, Johnson GV. The interrelationship between selective tau phosphorylation and microtubule association. Brain Res 1998;798:173-83.

92. Heidemann SR, Buxbaum RE. Mechanical tension as a regulator of axonal development. Neurotoxicology 1994;15:95-107.

93. Pfister BJ, Iwata A, Meaney DF, Smith DH. Extreme stretch growth of integrated axons. J Neurosci 2004;24:7978-83.

94. Singh A, Kallakuri S, Chen C, Cavanaugh JM. Structural and functional changes in nerve roots due to tension at various strains and strain rates: an in-vivo study. J Neurotrauma 2009;26:627-40.

95. Peter SJ, Mofrad MR. Computational modeling of axonal microtubule bundles under tension. Biophys J 2012;102:749-57.

96. Garcia JA, Pena JM, McHugh S, Jerusalem A. A Model of the Spatially Dependent Mechanical Properties of the Axon During Its Growth. Cmes-Computer Modeling in Engineering & Sciences 2012;87:411-32.

97. Loverde JR, Ozoka VC, Aquino R, Lin L, Pfister BJ. Live imaging of axon stretch growth in embryonic and adult neurons. J Neurotrauma 2011;28:2389-403.

98. Ahmed WW, Saif TA. Active transport of vesicles in neurons is modulated by mechanical tension. Sci Rep 2014;4:4481.

99. Komiya Y, Tashiro T. Effects of taxol on slow and fast axonal transport. Cell Motil Cytoskeleton 1988;11:151-6.

100. Chetta J, Kye C, Shah SB. Cytoskeletal dynamics in response to tensile loading of mammalian axons. Cytoskeleton (Hoboken) 2010;67:650-65.

101. Anava S, Greenbaum A, Ben Jacob E, Hanein Y, Ayali A. The regulative role of neurite mechanical tension in network development. Biophys J 2009;96:1661-70.

102. Au NP, Fang Y, Xi N, Lai KW, Ma CH. Probing for chemotherapy-induced peripheral neuropathy in live dorsal root ganglion neurons with atomic force microscopy. Nanomedicine 2014.

103. Hammarlund M, Jorgensen EM, Bastiani MJ. Axons break in animals lacking beta-spectrin. J Cell Biol 2007;176:269-75.

104. Li R. Culture methods for selective growth of normal rat and human Schwann cells. Methods Cell Biol 1998;57:167-86.

105. E. Gutierrez BB, E.V. Tkachenko, S.B. Shah, A. Groisman. Micro-fabricated devices with stretchable silicone substrates and micro-patterned silicone gels for experiments on adherent cells with high-resolution imaging. Mol Biol Cell2014:415.

106. Boyce FM, Bucher NL. Baculovirus-mediated gene transfer into mammalian cells. Proc Natl Acad Sci U S A 1996;93:2348-52.

107. Koch D, Rosoff WJ, Jiang J, Geller HM, Urbach JS. Strength in the periphery: growth cone biomechanics and substrate rigidity response in peripheral and central nervous system neurons. Biophys J 2012;102:452-60.

108. Love JM, Pathak GK, Chetta J, Shah SB. Variability in Membrane Continuity Between Schwann Cells and Neurons. Cellular and Molecular Bioengineering 2012;5:450-62.

109. Miller KE, Sheetz MP. Direct evidence for coherent low velocity axonal transport of mitochondria. J Cell Biol 2006;173:373-81.

110. Chetta J, Love JM, Bober BG, Shah SB. Bidirectional actin transport is influenced by microtubule and actin stability. Cell Mol Life Sci 2015.

111. Saxton WM, Hollenbeck PJ. The axonal transport of mitochondria. J Cell Sci 2012;125:2095-104.

112. Roy S, Winton MJ, Black MM, Trojanowski JQ, Lee VM. Rapid and intermittent cotransport of slow component-b proteins. J Neurosci 2007;27:3131-8.

113. Welzel O, Knorr J, Stroebel AM, Kornhuber J, Groemer TW. A fast and robust method for automated analysis of axonal transport. Eur Biophys J 2011;40:1061-9.

114. Ruthel G, Banker G. Actin-dependent anterograde movement of growth-cone-like structures along growing hippocampal axons: a novel form of axonal transport? Cell Motil Cytoskeleton 1998;40:160-73.

115. Flynn KC, Pak CW, Shaw AE, Bradke F, Bamburg JR. Growth cone-like waves transport actin and promote axonogenesis and neurite branching. Dev Neurobiol 2009;69:761-79.

116. Chada SR, Hollenbeck PJ. Nerve growth factor signaling regulates motility and docking of axonal mitochondria. Curr Biol 2004;14:1272-6.

117. Zheng J, Lamoureux P, Santiago V, Dennerll T, Buxbaum RE, Heidemann SR. Tensile regulation of axonal elongation and initiation. J Neurosci 1991;11:1117-25.

118. Phillips JB, Smit X, De Zoysa N, Afoke A, Brown RA. Peripheral nerves in the rat exhibit localized heterogeneity of tensile properties during limb movement. J Physiol 2004;557:879-87.

119. Amos LA, Lowe J. How Taxol stabilises microtubule structure. Chem Biol 1999;6:R65-9.

120. Boyette-Davis J, Xin W, Zhang H, Dougherty PM. Intraepidermal nerve fiber loss corresponds to the development of taxol-induced hyperalgesia and can be prevented by treatment with minocycline. Pain 2011;152:308-13.

121. Argyriou AA, Koltzenburg M, Polychronopoulos P, Papapetropoulos S, Kalofonos HP. Peripheral nerve damage associated with administration of taxanes in patients with cancer. Crit Rev Oncol Hematol 2008;66:218-28.

122. Masurovsky EB, Peterson ER, Crain SM, Horwitz SB. Morphological alterations in dorsal root ganglion neurons and supporting cells of organotypic mouse spinal cord-ganglion cultures exposed to taxol. Neuroscience 1983;10:491-509.

123. Ochi K, Horiuchi Y, Nakamura T, Sato K, Arino H, Koyanagi T. Ulnar nerve strain at the elbow in patients with cubital tunnel syndrome: effect of simple decompression. J Hand Surg Eur Vol 2013;38:474-80.

124. Luna C, Detrick L, Shah SB, Cohen AH, Aranda-Espinoza H. Mechanical properties of the lamprey spinal cord: uniaxial loading and physiological strain. J Biomech 2013;46:2194-200.

125. Shah SB, Lieber RL. Simultaneous imaging and functional assessment of cytoskeletal protein connections in passively loaded single muscle cells. J Histochem Cytochem 2003;51:19-29.

126. Walbeehm ET, Afoke A, de Wit T, Holman F, Hovius SE, Brown RA. Mechanical functioning of peripheral nerves: linkage with the "mushrooming" effect. Cell Tissue Res 2004;316:115-21.

127. Yamanari M, Ishii K, Fukuda S, Lim Y, Duan L, Makita S, Miura M, Oshika T, Yasuno Y. Optical rheology of porcine sclera by birefringence imaging. PLoS One 2012;7:e44026.

128. Xiong J, Wang SM, Zhou W, Wu JG. Measurement and analysis of ultimate mechanical properties, stress-strain curve fit, and elastic modulus formula of human abdominal aortic aneurysm and nonaneurysmal abdominal aorta. J Vasc Surg 2008;48:189-95.

129. Gomori G. A rapid one-step trichrome stain. Am J Clin Pathol 1950;20:661-4.

130. Bernal R, Pullarkat PA, Melo F. Mechanical properties of axons. Phys Rev Lett 2007;99:018301.

131. Dennerll TJ, Lamoureux P, Buxbaum RE, Heidemann SR. The cytomechanics of axonal elongation and retraction. J Cell Biol 1989;109:3073-83.

132. Borschel GH, Kia KF, Kuzon WM, Jr., Dennis RG. Mechanical properties of acellular peripheral nerve. J Surg Res 2003;114:133-9.

133. Alexander MJ, Barkmeier-Kraemer JM, Vande Geest JP. Biomechanical properties of recurrent laryngeal nerve in the piglet. Ann Biomed Eng 2010;38:2553-62.

134. Jeronimo A, Jeronimo CA, Rodrigues Filho OA, Sanada LS, Fazan VP. Microscopic anatomy of the sural nerve in the postnatal developing rat: a longitudinal and lateral symmetry study. J Anat 2005;206:93-9.

135. Sunderland S, Bradley KC. Stress-Strain Phenomena in Denervated Peripheral Nerve Trunks. Brain 1961;84:125-&.

136. Vasantha J, Kannan G, Goud T, Palani T, Vanitha R, Anitha R, Priya J. Pharmacokinetic evaluation of Paclitaxel in South Indian cancer patients: a prospective study. J Young Pharm 2011;3:322-8.

137. Sparreboom A, van Tellingen O, Nooijen WJ, Beijnen JH. Nonlinear pharmacokinetics of paclitaxel in mice results from the pharmaceutical vehicle Cremophor EL. Cancer Res 1996;56:2112-5.

138. Huehnchen P, Boehmerle W, Endres M. Assessment of paclitaxel induced sensory polyneuropathy with "Catwalk" automated gait analysis in mice. PLoS One 2013;8:e76772.

139. Roytta M, Raine CS. Taxol-induced neuropathy: chronic effects of local injection. J Neurocytol 1986;15:483-96.

140. Rosenberg KJ, Ross JL, Feinstein HE, Feinstein SC, Israelachvili J. Complementary dimerization of microtubule-associated tau protein: Implications for microtubule bundling and tau-mediated pathogenesis. Proc Natl Acad Sci U S A 2008;105:7445-50.

141. Reck-Peterson SL, Yildiz A, Carter AP, Gennerich A, Zhang N, Vale RD. Single-molecule analysis of dynein processivity and stepping behavior. Cell 2006;126:335-48.

142. Thomas PK. The connective tissue of peripheral nerve: an electron microscope study. J Anat 1963;97:35-44.

143. Windebank AJ, Wood P, Bunge RP, Dyck PJ. Myelination determines the caliber of dorsal root ganglion neurons in culture. J Neurosci 1985;5:1563-9.

144. Zhou FQ, Zhou J, Dedhar S, Wu YH, Snider WD. NGF-induced axon growth is mediated by localized inactivation of GSK-3beta and functions of the microtubule plus end binding protein APC. Neuron 2004;42:897-912.

145. Bober BG, Gutierrez E, Plaxe S, Groisman A, Shah SB. Combinatorial Influences of Paclitaxel and Strain on Axonal Transport. Exp Neurol 2015.

146. Cheng S, Donhauser Z. GMPCPP and Paclitaxel Effect on Microtubule Stiffness. FASEB J 2013;27.

147. Debrabander M, Geuens G, Nuydens R, Willebrords R, Demey J. Taxol Induces the Assembly of Free Microtubules in Living Cells and Blocks the

Organizing Capacity of the Centrosomes and Kinetochores. P Natl Acad Sci-Biol 1981;78:5608-12.

148. Brandt R, Lee G. Functional organization of microtubule-associated protein tau. Identification of regions which affect microtubule growth, nucleation, and bundle formation in vitro. J Biol Chem 1993;268:3414-9.

149. Ross JL, Fygenson DK. Mobility of taxol in microtubule bundles. Biophys J 2003;84:3959-67.

150. Park H, Kim M, Fygenson DK. Tau-isoform dependent enhancement of taxol mobility through microtubules. Arch Biochem Biophys 2008;478:119-26.

151. Trojanowski JQ, Smith AB, Huryn D, Lee VM. Microtubule-stabilising drugs for therapy of Alzheimer's disease and other neurodegenerative disorders with axonal transport impairments. Expert Opin Pharmacother 2005;6:683-6.

152. Reddy PH. Abnormal tau, mitochondrial dysfunction, impaired axonal transport of mitochondria, and synaptic deprivation in Alzheimer's disease. Brain Res 2011;1415:136-48.

153. Lei P, Ayton S, Finkelstein DI, Adlard PA, Masters CL, Bush AI. Tau protein: relevance to Parkinson's disease. Int J Biochem Cell Biol 2010;42:1775-8.

154. Mi K, Johnson GV. The role of tau phosphorylation in the pathogenesis of Alzheimer's disease. Curr Alzheimer Res 2006;3:449-63.

155. Wostyn P, Audenaert K, De Deyn PP. Alzheimer's disease-related changes in diseases characterized by elevation of intracranial or intraocular pressure. Clin Neurol Neurosurg 2008;110:101-9.

156. Gullans SR, Verbalis JG. Control of brain volume during hyperosmolar and hypoosmolar conditions. Annu Rev Med 1993;44:289-301.

157. Grande PO, Romner B. Osmotherapy in brain edema: a questionable therapy. J Neurosurg Anesthesiol 2012;24:407-12.

158. Hoffmann EK, Lambert IH, Pedersen SF. Physiology of cell volume regulation in vertebrates. Physiol Rev 2009;89:193-277.

159. Reuzeau C, Mills LR, Harris JA, Morris CE. Discrete and reversible vacuole-like dilations induced by osmomechanical perturbation of neurons. J Membr Biol 1995;145:33-47.

160. Lang F, Busch GL, Ritter M, Volkl H, Waldegger S, Gulbins E, Haussinger D. Functional significance of cell volume regulatory mechanisms. Physiol Rev 1998;78:247-306.

161. Lang F, Busch GL, Volkl H. The diversity of volume regulatory mechanisms. Cell Physiol Biochem 1998;8:1-45.

162. Fernandez P, Pullarkat PA. The role of the cytoskeleton in volume regulation and beading transitions in PC12 neurites. Biophys J 2010;99:3571-9.

163. Pedersen SF, Mills JW, Hoffmann EK. Role of the F-actin cytoskeleton in the RVD and RVI processes in Ehrlich ascites tumor cells. Exp Cell Res 1999;252:63-74.

164. Blase C, Becker D, Kappel S, Bereiter-Hahn J. Microfilament dynamics during HaCaT cell volume regulation. Eur J Cell Biol 2009;88:131-9.

165. Heubusch P, Jung CY, Green FA. The osmotic response of human erythrocytes and the membrane cytoskeleton. J Cell Physiol 1985;122:266-72.

166. Wang J, Xie X. Development of a quantitative, cell-based, high-content screening assay for epidermal growth factor receptor modulators. Acta Pharmacol Sin 2007;28:1698-704.

167. Goh JM, Bensley JG, Kenna K, Sozo F, Bocking AD, Brien J, Walker D, Harding R, Black MJ. Alcohol exposure during late gestation adversely affects myocardial development with implications for postnatal cardiac function. Am J Physiol Heart Circ Physiol 2011;300:H645-51.

168. Gallo G. Myosin II activity is required for severing-induced axon retraction in vitro. Exp Neurol 2004;189:112-21.

169. Ridley AJ. Life at the leading edge. Cell 2011;145:1012-22.

170. Maloney JM, Van Vliet KJ. Chemoenvironmental modulators of fluidity in the suspended biological cell. Soft Matter 2014;10:8031-42.

171. Sachs F. Mechanical transduction by membrane ion channels: a mini review. Mol Cell Biochem 1991;104:57-60.

172. Ito T, Suzuki A, Stossel TP. Regulation of water flow by actin-binding protein-induced actin gelatin. Biophys J 1992;61:1301-5.

173. Henson JH. Relationships between the actin cytoskeleton and cell volume regulation. Microsc Res Tech 1999;47:155-62.

174. Dai J, Sheetz MP, Wan X, Morris CE. Membrane tension in swelling and shrinking molluscan neurons. J Neurosci 1998;18:6681-92.

175. Morris CE, Wang JA, Markin VS. The invagination of excess surface area by shrinking neurons. Biophys J 2003;85:223-35.

176. Ziyadeh FN, Mills JW, Kleinzeller A. Hypotonicity and cell volume regulation in shark rectal gland: role of organic osmolytes and F-actin. Am J Physiol 1992;262:F468-79.

177. Maugis B, Brugues J, Nassoy P, Guillen N, Sens P, Amblard F. Dynamic instability of the intracellular pressure drives bleb-based motility. J Cell Sci 2010;123:3884-92.

178. Lorentzen A, Bamber J, Sadok A, Elson-Schwab I, Marshall CJ. An ezrin-rich, rigid uropod-like structure directs movement of amoeboid blebbing cells. J Cell Sci 2011;124:1256-67.

179. Norman L, Sengupta K, Aranda-Espinoza H. Blebbing dynamics during endothelial cell spreading. Eur J Cell Biol 2011;90:37-48.

180. Bustamante M, Roger F, Bochaton-Piallat ML, Gabbiani G, Martin PY, Feraille E. Regulatory volume increase is associated with p38 kinase-dependent actin cytoskeleton remodeling in rat kidney MTAL. Am J Physiol Renal Physiol 2003;285:F336-47.

181. Sanchez-Olea R, Pasantes-Morales H, Schousboe A. Neurons respond to hyposmotic conditions by an increase in intracellular free calcium. Neurochem Res 1993;18:147-52.

182. Encinas M, Iglesias M, Liu Y, Wang H, Muhaisen A, Cena V, Gallego C, Comella JX. Sequential treatment of SH-SY5Y cells with retinoic acid and brain-derived neurotrophic factor gives rise to fully differentiated, neurotrophic factor-dependent, human neuron-like cells. J Neurochem 2000;75:991-1003.

183. Wakatsuki T, Schwab B, Thompson NC, Elson EL. Effects of cytochalasin D and latrunculin B on mechanical properties of cells. J Cell Sci 2001;114:1025-36.

184. Allansson L, Khatibi S, Gustavsson T, Blomstrand F, Olsson T, Hansson E. Single-cell volume estimation by three-dimensional wide-field microscopy applied to astroglial primary cultures. J Neurosci Methods 1999;93:1-11.

185. Speck RM, DeMichele A, Farrar JT, Hennessy S, Mao JJ, Stineman MG, Barg FK. Scope of symptoms and self-management strategies for chemotherapy-

induced peripheral neuropathy in breast cancer patients. Support Care Cancer 2012;20:2433-9.

186. Binkley JM, Harris SR, Levangie PK, Pearl M, Guglielmino J, Kraus V, Rowden D. Patient perspectives on breast cancer treatment side effects and the prospective surveillance model for physical rehabilitation for women with breast cancer. Cancer 2012;118:2207-16.

187. Courneya KS, McKenzie DC, Mackey JR, Gelmon K, Friedenreich CM, Yasui Y, Reid RD, Vallerand JR, Adams SC, Proulx C, Dolan LB, Wooding E, Segal RJ. Subgroup effects in a randomised trial of different types and doses of exercise during breast cancer chemotherapy. Br J Cancer 2014;111:1718-25.

188. Pan Y, Yang K, Shi X, Liang H, Zhang F, Lv Q. Tai chi chuan exercise for patients with breast cancer: a systematic review and meta-analysis. Evid Based Complement Alternat Med 2015;2015:535237.

189. Medina McKeon JM, Yancosek KE. Neural gliding techniques for the treatment of carpal tunnel syndrome: a systematic review. J Sport Rehabil 2008;17:324-41.

190. Page MJ, O'Connor D, Pitt V, Massy-Westropp N. Exercise and mobilisation interventions for carpal tunnel syndrome. Cochrane Database Syst Rev 2012;6:CD009899.